DEVELOPMENT AND CHARACTERIZATION OF ELECTROLESS NI-P COMPOSITE COATINGS WITH TRIBALOY ADDITIONS

by

Ahmed Mabrouk

Submitted in partial fulfilment of the requirements
for the degree of Master of Applied Science

at

Dalhousie University
Halifax, Nova Scotia
August 2023

Table of Contents

List of Tables v

List of Figures vi

Abstract x

Acknowledgements xi

Chapter 1 – Introduction 1

Chapter 2 – Literature Review 4

2.1 Electroless Ni-P Coatings 4

2.1.1 Electroless Plating Bath 6

2.1.2 Factors Affecting Electroless Plating 7

2.1.3 Properties of Electroless Ni-P Coatings 9

2.2 Composite Ni-P Coatings 10

2.2.1 Factors of Composite Coatings 11

2.2.2 Properties of Composite Coatings 13

2.3 Tribaloy Alloys 17

2.3.1 Laves Phase 18

2.3.2 Types of Tribaloys 19

2.3.3 Tribaloy Coatings 21

2.4 Cracking and Toughening Mechanisms 23

2.4.1 Hertzian Contact 23

2.4.2 Crack Types 24

2.4.3 Toughening Mechanisms 25

2.5 Sliding Wear 27

2.5.1 Forms of Wear 27

2.5.2 Wear Testing 28
2.5.3 Delamination 29
Chapter 3 – Methodology 30
3.1 Substrate and Powder Characterization 30
3.1.1 Low Carbon Steel Substrate 30
3.1.2 Tribaloy Powder 31
3.2 Coating Preparation 32
3.3 Coating Characterization 34
3.4 Micro-Hardness Testing 34
3.5 Indentation Testing 37
3.6 Scratch Testing 38
3.7 Low-Stress Abrasion Testing 39
Chapter 4 – Results and Discussions 41
4.1 Coating Characterization 41
4.2 Micro-Hardness 48
4.3 Indentation Behaviour 50
4.3.1 Load–Depth Curves and Acoustic Emissions 50
4.3.2 Cracking Behaviour 53
4.3.3 Toughening Mechanisms 54
4.4 Scratch Behaviour 59
4.4.1 Wear Tracks and Acoustic Emissions 59
4.4.2 Volume Loss and Wear Rates 63
4.4.3 Wear Mechanisms 64
4.4.3 Coefficient of Friction 67
4.5 Low-Stress Abrasion 68

4.5.1 Abrasion Wear Scar 68
4.5.2 Abrasion Rate 70
4.5.3 Wear Scar Analysis 71
4.5.4 Wear Mechanisms 77
Chapter 5 – Conclusions and Recommendations 82
References 84
Appendix A – As-Deposited Coating Characterization 98
Appendix B – Micro-Hardness Load–Depth Curves 100
Appendix C – Indentation Images 101
Appendix D – Scratch Full Length Tracks 103
Appendix E – Abrasion Scars 105

List of Tables

Table 3 – 1: Composition of AISI steel [127]. 30

Table 4 – 1: Surface EDS analysis results of Ni-P-Tribaloy. 44

Table 4 – 2: Composition of Ni-P-Tribaloy. 45

Table 4 – 3: Ni-P micro-hardness measurements. 49

Table 4 – 4: Ni-P-Tribaloy micro-hardness measurements 49

Table 4 – 5: Widths and depths of Ni-P and Ni-P-Tribaloy scratch wear tracks. 62

List of Figures

Figure 1 – 1: Cause of pipeline incidents reported by CEPA [5]. 1

Figure 2 – 1: Schematic diagram of a typical electroless plating cell [22]. 7

Figure 2 – 2: Wear rates of electroless nickel composite coatings [10]. 14

Figure 2 – 3: Microstructure of Tribaloy [76]. 19

Figure 2 – 4: Hertzian indentation process [103]. 23

Figure 2 – 5: Crack types under indentation [106]. 24

Figure 2 – 6: Crack bridging toughening mechanism [113]. 25

Figure 2 – 7: Crack deflection toughening mechanism [114]. 26

Figure 2 – 8: Schematic of particle concentration increase due to indentation [116]. 27

Figure 2 – 9: Possible mechanisms of abrasive wear [118]. 28

Figure 2 – 10: Illustration of coating delamination [6]. 29

Figure 3 – 1: Microstructure of AISI 1018 steel. 31

Figure 3 – 2: Particle size distribution of powder. 32

Figure 3 – 3: SEM image of the powder. 32

Figure 3 – 4: Coating deposition set-up. 33

Figure 3 – 5: NANOVEA PB 1000 mechanical tester. 35

Figure 3 – 6: (a) Vickers indenter. (b) Example of produced indent. 35

Figure 3 – 7: Typical load–depth curve [128]. 36

Figure 3 – 8: PASCO ME-8236 materials testing apparatus. 37

Figure 3 – 9: Universal Micro Tribometer. 38

Figure 3 – 10: Schematic diagram of dry sand/rubber wheel test apparatus [124]. 39

Figure 3 – 11: Ottawa silica sand particle size distribution. 40

Figure 4 – 1: X-ray diffraction patterns for AISI 1018 steel, Tribaloy powder, Ni-P, and Ni-P-Tribaloy. 42

Figure 4 – 2: (a) Polished surface and (b) cross-section of Ni-P-Tribaloy. 43

Figure 4 – 3: Surface topography of Ni-P-Tribaloy. 43

Figure 4 – 4: Surface topography of Ni-P. 44

Figure 4 – 5: Surface EDS mapping of Ni-P-Tribaloy. 45

Figure 4 – 6: Cross-sectional EDS mapping of Ni-P-Tribaloy. 46

Figure 4 – 7: Cross-section of as-deposited Ni-P-Tribaloy coating. 47

Figure 4 – 8: SEM image of as-deposited Ni-P-Tribaloy surface. 47

Figure 4 – 9: SEM image of as-deposited Ni-P-Tribaloy cross-section. 48

Figure 4 – 10: Micro-hardness of Ni-P and Ni-P-Tribaloy. 49

Figure 4 – 11: Load–depth curves of Ni-P and Ni-P-Tribaloy. 50

Figure 4 – 12: Ni-P Indentation load–depth curve with AE. 51

Figure 4 – 13: Ni-P-Tribaloy indentation load–depth curve with AE. 51

Figure 4 – 14: Confocal microscopy images of indents for (a) Ni-P and (b) Ni-P-Tribaloy. 52

Figure 4 – 15: Select confocal images of indent cross-section for Ni-P. 53

Figure 4 – 16: Select confocal images of indent cross-section for Ni-P-Tribaloy. 54

Figure 4 – 17: Crack depth in (a) Ni-P and (b) Ni-P-Tribaloy. 54

Figure 4 – 18: Ni-P close-up surface indent. 55

Figure 4 – 19: Toughening mechanisms in Ni-P-Tribaloy. 56

Figure 4 – 20: SEM image of crack deflection in Ni-P-Tribaloy. 57

Figure 4 – 21: 3D image of indentation for Ni-P. 58

Figure 4 – 22: 3D image of indentation for Ni-P-Tribaloy. 58

Figure 4 – 23: Examples of scratch wear tracks from (a) Ni-P and (b) Ni-P-Tribaloy. 59

Figure 4 – 24: AE signals of single-pass scratch. 60

Figure 4 – 25: Shape and average profile of Ni-P scratches. 61

Figure 4 – 26: Shape and average profile of Ni-P-Tribaloy scratches. 62

Figure 4 – 27: Volume loss per sliding distance from scratch test. 63

Figure 4 – 28: SEM image of material deformation wear mechanism for Ni-P-Tribaloy after 100 passes. 64

Figure 4 – 29: SEM image closeup of material deformation wear mechanism for Ni-P-Tribaloy after 100 passes. 65

Figure 4 – 30: SEM image of fracture at the wear track ridges for Ni-P-Tribaloy after 100 passes. 66

Figure 4 – 31: EDS mapping of scratch wear track for Ni-P-Tribaloy after 100 passes. . 66

Figure 4 – 32: Coefficient of Friction as a function of sliding distance. 67

Figure 4 – 33: Pictures of wear scars on (a) Ni-P and (b) Ni-P-Tribaloy coating samples. 68

Figure 4 – 34: 3D images of the wear scars for (a) Ni-P and (b) Ni-P-Tribaloy. 69

Figure 4 – 35: Average profile across the Ni-P wear scar. 69

Figure 4 – 36: Average profile across the Ni-P-Tribaloy wear scar. 69

Figure 4 – 37: Volume loss per wheel revolution from abrasion test. 70

Figure 4 – 38: Ni-P-Tribaloy surface depicting the flattening (a) inside and (b) at the edge of the abrasion scar. 72

Figure 4 – 39: Illustrative diagram of the contact area between the wheel and specimen. 73

Figure 4 – 40: Average profile along the Ni-P wear scar. 73

Figure 4 – 41: Average profile along the Ni-P-Tribaloy wear scar. 74

Figure 4 – 42: SEM images of plowing in Ni-P-Tribaloy. 75

Figure 4 – 43: SEM image of a cutting in Ni-P-Tribaloy. 75

Figure 4 – 44: SEM image of Ni-P-Tribaloy abrasion wear scar. 76

Figure 4 – 45: SEM image of Ni-P abrasion wear scar. 76

Figure 4 – 46: Cross-section of Ni-P-Tribaloy wear scar. 77

Figure 4 – 47: Schematic diagram of Ni-P-Tribaloy wear mechanism during abrasion. . 78

Figure 4 – 48: SEM images of (a) first step and (b) second step of particle removal. 79

Figure 4 – 49: Detachment of Tribaloy particle from coating matrix. 80

Figure A – 1: Additional SEM image of the as-deposited Ni-P-Tribaloy cross-section. .. 98

Figure A – 2: Additional SEM image of the as-deposited Ni-P-Tribaloy cross-section. .. 98

Figure A – 3: EDS mapping of as-deposited Ni-P-Tribaloy coating cross-section. 99

Figure B – 1: All load–depth curves for Ni-P. 100

Figure B – 2: All load–depth curves for Ni-P-Tribaloy. 100

Figure C – 1: Additional images of indent cross-section around Ni-P. 101

Figure C – 2: Additional images of indent cross-section around Ni-P-Tribaloy. 101

Figure C – 3: Additional close-up images of indent around Ni-P. 101

Figure C – 4: Additional close-up images of indent around Ni-P-Tribaloy. 102

Figure D – 1: Confocal microscopy image of all scratches for Ni-P. 103

Figure D – 2: Confocal microscopy image of all scratches for Ni-P-Tribaloy. 104

Figure E – 1: Confocal microscopy image of abrasion wear scar on Ni-P. 105

Figure E – 2: Confocal microscopy image of abrasion wear scar on Ni-P-Tribaloy. 106

Abstract

Oil and gas pipelines are subject to various forms of damage and degradation during their operation. Electroless Nickel (Ni-P) coatings are widely employed as protective coatings due to their ease of application and unique properties, including high wear and corrosion resistance. However, they are not ideal for protecting pipelines due to their brittleness. Thus, Tribaloy (CoMoCrSi) alloy is used in this study as second phase particles to develop a novel Ni-P composite coating with enhanced hardness and toughness. The objective of this research is to develop and characterize the Ni-P-Tribaloy composite coating, and to evaluate the effect of the addition of Tribaloy particles on the wear performance. Ni-P-Tribaloy coatings were successfully deposited on AISI 1018 steel substrates. Coating characterization was carried out using XRD, SEM, and EDS. The 15.7 vol.% Tribaloy composite coating was subjected to hertzian-type indentation, multiple-pass scratch, and low-stress abrasion tests to examine the coating's wear behaviour under different conditions. The Ni-P-Tribaloy coating exhibited superior indentation behaviour. It was found that the addition of Tribaloy particles improved the hardness and fracture toughness of Ni-P and promoted ductile behaviour. Higher wear rates were observed under sliding wear for Ni-P-Tribaloy mainly due to the large Tribaloy particle size used.

Acknowledgements

First and foremost, I would like to thank my supervisor, Dr. Zoheir Farhat, for giving me this opportunity and for his guidance and support throughout my MASc program. Also, I would like to thank Dr. Md. Aminul Islam and Dr. Ahmed Saif for serving as members on my supervisory committee. Moreover, thanks to the National Research Council of Canada, especially Dr. Islam, for performing the abrasion tests. I would also like to thank Rielle Jensen for all her help with my research work, as well as Patricia Scallion, Mark Amegadzie, and Zhila Russell for their training and assistance. Finally, I would like to express my gratitude to my parents for always supporting me.

Ahmed Mabrouk

August 2023

Chapter 1 – Introduction

The global dependence on pipelines in major applications such as in the oil and gas industry, during the production and distribution of crude oil and natural gas, has prompted the need for research aiming to protect pipelines from failure and prolong their service life [1]. Pipelines and process equipment are subject to various forms of service-induced damage and degradation including uniform and/or localized metallurgical failures [2]. Pipeline transport is a safe and economic way for transporting oil and gas compared to other means of transportation, however, pipeline failure has the potential of causing significant financial and environmental losses [3], [4].

The leading cause of pipeline incidents over the period 2016–2020, according to the latest report from the Canadian Energy Pipeline Association (CEPA) [5], is metal loss, followed by cracking, then materials, manufacturing, and construction defects, as shown in Figure 1–1 based on monitoring of the 95,592 km network of transmission pipelines. CEPA also reported in their 2021 performance report that $1.2 billion were invested in maintenance and monitoring of pipeline systems in 2020, as well as, $88.9 million invested between 2016–2020 in innovative technology for reducing pipeline corrosion and improving pipeline inspection, leak detection and damage prevention.

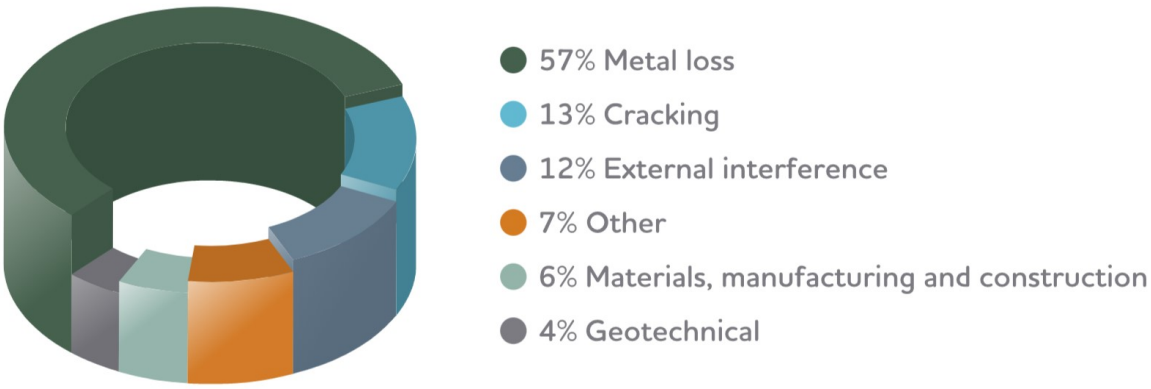

Figure 1 – 1: Cause of pipeline incidents reported by CEPA [5].

To minimize the degradation due to these causes, different preventative and protective measures have been adopted such as changing the material and applying coatings, when altering the operating conditions and environment is not possible nor

practical. Changing the material to one that is more wear and corrosion resistant could be costlier, therefore, the application of coatings is a suitable technique to provide said protection [6].

Coatings can be applied through several methods including electroplating, electroless plating, mechanical plating, and hot dipping. Electroless coating is the most marketable method due to its unique properties and ease of application [7]. Without the use of an external electric current, this process can achieve uniform coatings on complex parts compared to electroplating, making it an excellent candidate for protecting pipelines [6], [7]. Electroless nickel-phosphorus (Ni-P) coatings represent over 95% of industrial electroless coatings and they are widely used in several industries, such as electronics, aerospace, and automotive industries, due to their favorable properties, including high wear and corrosion resistance, hardness, lubricity, and adhesion, allowing for protection of parts under severe operating conditions [7]–[11]. However, Ni-P coatings are brittle and they exhibit low toughness, which limits the coating's suitability for use as pipeline coatings where high scratch and dent resistance are required [6], [11], [12].

Recent research has proven that specific properties can be enhanced through the co-deposition of second phase particles into the metallic Ni-P matrix, and this leading trend in research has resulted in the development of different Ni-P composite coatings [13]. Tribaloy (CoMoCrSi) alloys are cobalt based alloys that possess outstanding wear and corrosion resistance and hardness due to the alloy's unique chemical composition, with each alloying element contributing to the alloy properties [14]. There is currently no literature available on the deposition of Tribaloy particles by electroless plating, however, it is an excellent candidate to be used in the development of a wear-resistant Ni-P-Tribaloy composite coating. Improved wear resistance is achieved by enhancing the overall hardness and toughness properties of the coating.

In order to fill this gap in research, the novel composite coating needs to be fully characterized through various experimental methods to develop an understanding of its behaviour under different wear conditions, after examining the integrity and composition of the coating to confirm its successful deposition. The wear behaviour will be investigated through hertzian indentation, scratch, and low-stress abrasion tests, accompanied by

comparisons with monolithic Ni-P coatings under the same conditions to evaluate the effect of the Tribaloy additions. This will require an understanding of Hertzian contact, sliding wear, toughening mechanisms, wear mechanisms, fracture mechanisms and types of cracks. Thus, the objectives of this research are as follows:

1. Investigate the possibility of depositing electroless Ni-P-Tribaloy composite coatings on low carbon steel substrates.
2. Characterize the Ni-P-Tribaloy coating: composition, surface, thickness, micro-hardness, etc.
3. Study the performance of the Ni-P-Tribaloy coating under indentation, scratch, and abrasion tests.
4. Compare the wear performance of the Ni-P-Tribaloy with that of the monolithic Ni-P coating.
5. Identify the toughening and wear mechanisms present in the Ni-P-Tribaloy coating.

The content of this thesis is divided into five chapters. Chapter 2 contains a literature review on electroless nickel, composite coatings, Tribaloy alloys, toughening mechanisms, wear mechanisms, and fracture mechanics. Chapter 3 outlines the experimental methodology. Chapter 4 contains the presentation of the results and their formal discussion. Chapter 5 provides the conclusions and future recommendations.

Chapter 2 – Literature Review

2.1 Electroless Ni-P Coatings

Electroless plating is an autocatalytic plating method through chemical reduction in an aqueous solution without the use of electrical current, involving a series of simultaneous chemical reactions. Unlike electroplating, the driving force of this process is supplied by a reducing agent. It is used to provide mechanical and tribological properties such as hardness and resistance to wear and corrosion, as well as aesthetic appearance of metallic parts [15], [16]. The most common type of electroless plating is the electroless deposition of nickel, or Electroless Nickel (EN). However, other metals are also being deposited including copper, gold, and cobalt [7], [10].

The deposition of nickel through the reduction of the metal salt by hypophosphite was first discovered by Wurtz in 1844. Later, Roux patented the process for general metal plating using hypophosphite and orthophosphite [10], [16], [17]. However, this process have not been studied further or used commercially until it was rediscovered in 1946 by Brenner and Riddell [18]. They have outlined the process of deposition of nickel and cobalt by chemical reduction using a variety of reducing agents, operating parameters, and bath compositions, in order to find the optimum conditions. In 1947, Brenner and Riddell proposed the term “electroless” for this process and outlined their findings for the optimal bath conditions [19].

The electroless plating method, particularly Electroless Nickel, has since been the focus of research interest, successfully used in various surface engineering applications, and proven to have several advantages. Numerous characterization studies have been done on different electroless coatings and it has been found to have excellent tribological properties such as high hardness, wear resistance, corrosion resistance, and lubricity, allowing for protection of parts in unfavorable environments [9], [15].

Studies have shown that the content of phosphorus, or boron, in the coating deposit can alter its corrosion resistance and hardness. Also, the addition of other alloying elements will have an effect on the behavior and properties of the coatings, which opened a new area of research to find new coatings with desired properties for specific applications, by

varying the coating composition [10], [15]. Electroless plating is also an efficient and cost-effective process as it can be carried out in a controlled environment, requiring no electricity and using less equipment than electroplating, as well as requiring fewer coats to accomplish a strong, high-quality coating [15].

The driving force for the reduction of the coating metal ions and their deposition on the substrate is supplied by a reducing agent, typically sodium hypophosphite for Electroless Nickel. Since this driving force is essentially constant at all points of the surface, and not dependent on current distribution, the deposit thickness is uniform regardless of the complexity of the surface geometry of the substrate, provided that the agitation is sufficient to ensure a uniform concentration of metal ions and reducing agents [15]. This combined with the ability of electroless plating to be used to coat various metals such as carbon steels, stainless steels, and aluminum, allows this method to be very effective in coating a variety of industrial parts with irregular shapes and complex geometry evenly and completely, such as valves, bores, mechanical tools, and threaded parts [15], [20].

In this process, the reaction of the metal ions of the coating metal with the reducing agent results in the deposition of metal atoms of the coating metal and the oxidized product of the reducing agent [16]. In the case of Electroless Nickel, using sodium hypophosphite as the reducing agent, the anodic and cathodic reactions are as follows [9], [16]:

$$H_2PO^{2-} + H_2O \rightarrow H_2PO^{3-} + 2H^+ + 2e^-$$

$$Ni^{2+} + 2e^- \rightarrow Ni$$

Resulting in the following net reaction:

$$Ni^{2+} + H_2PO^{2-} + H_2O \rightarrow Ni + H_2PO^{3-} + 2H^+$$

The process described above utilizes the reducing effect of the hypophosphite in salt solution of nickel at a high temperature. The hypophosphite is oxidized as the anodic component of this chemical reaction, resulting in a negative charge on the surface of the base metal, while the nickel ions from the salt solution are reduced to nickel atoms as they are deposited on the substrate [15].

2.1.1 Electroless Plating Bath

For optimal coating deposition, the plating bath must be controlled at certain operating parameters including temperature and pH. Properly controlling the pH allows for achieving maximum reducing power, therefore, achieving maximum deposition rates, while the temperature of the bath provides the energy for deposition. Tests have been conducted in various bath compositions to find the suitable operating conditions for each application [15], [19].

A typical plating bath generally consists of the following components [10], [21]:

- Metal ions
- Reducing agent
- Complexing agent
- Stabilizer
- Buffer
- pH regulator

The first component is the salt solution of the coating metal. This is the source of metal ions, to be reduced and deposited on the surface of the substrate [21]. Secondly, the reducing agent supplies the electrons for the reduction of metal ions while getting oxidized. In case of hypophosphite, it also supplies the phosphorus content in the deposited alloy [9]. Moreover, a complexing agent improves the quality of the deposit. It prevents excess of free metal ions concentration and prevents nickel phosphate precipitation in Electroless Nickel [10], [15]. The Buffer sustains the pH for a long time. It controls the pH allowing for a thin and uniform plating to be obtained [21]. Also, the presence of pH regulators for the adjustment of the pH in the short term. The pH of the solution decreases consistently during reduction; therefore, continuous additions of an alkali hydroxide is required [9], [21]. The stabilizer prevents the decomposition of the coating solution. It prevents the bath from decomposition by protecting catalytically active deposition. Accelerators increase the deposition rate by activating the hypophosphite anions, thus accelerating the reducing agent [10], [15].

Bath additives such as complexing agents and stabilizers are added to plating baths to improve their operation. Complexing agents are typically organic acids or their salts. Ammonium ion is normally used in alkaline baths to control the pH. The complexing agents' main purposes are to preserve the stability of pH, to prevent the precipitation of the metal salt, and to decrease the amount of free metal ions [10], [15]. Stabilizers are needed in the event of an increase in the quantity of the produced hydrogen gas resulting in the precipitation of fine black particles causing the solution to decompose abruptly. Typical materials used as stabilizers include thiourea, sodium ethylxanthate, lead or tin sulphide [15].

A basic apparatus used in electroless plating by Li et al. [22] is shown in Figure 2–1, including, a thermostat for controlling temperature and a specimen rotator.

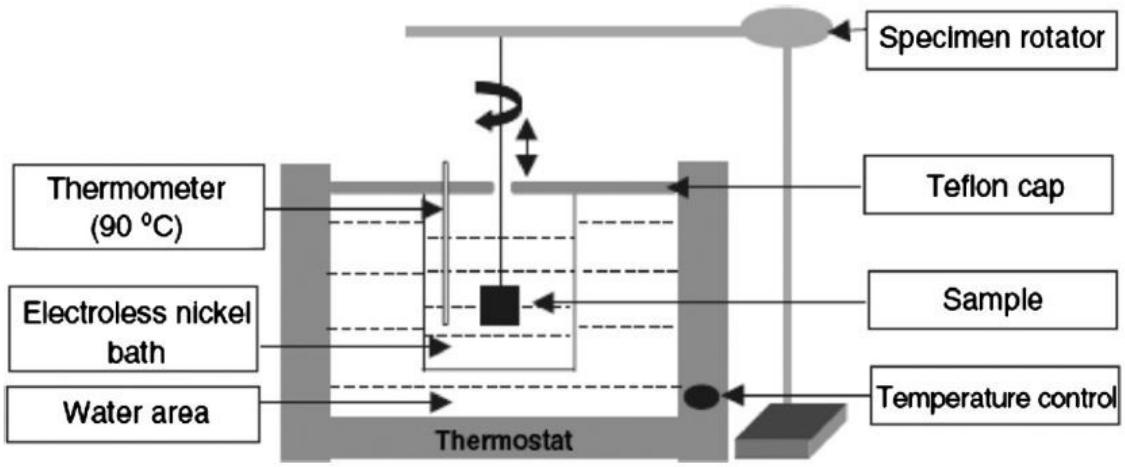

Figure 2 – 1: Schematic diagram of a typical electroless plating cell [22].

2.1.2 Factors Affecting Electroless Plating

There are several factors that affect the deposition rate and the quality of the deposition and its appearance during the process of electroless plating. The factors include the bath concentration, the bath time, the bath volume, the operating temperature and pH, and the additives to the bath [15], [23].

Bath concentration is the quantity of each component of the plating bath, and it is crucial to the quality of the final product, as it directly affects the rate of deposition and the

amount of metal deposited on the substrate. A higher deposition rate is achieved by a higher concentration of the metal ions source or the reducing agent. However, the depletion of the metal ions causes a decrease in the mass of the reduced metal as the equilibrium shifts and less metal ions are available relative to the electrons released by the reducing agent. A study with the emphasis of examining the concentration of the reducing agent has found that an increase in concentration leads to a higher deposition rate and surface roughness. However, with a further increase, it leads to bath decomposition [15], [24].

Bath time refers to the duration of the plating process, and it is dependent on the stability of the bath solution. A longer bath time yields an increase in deposition of the coating metal, provided that the bath is stable [15]. Bath volume is another parameter that influences the quality of the plating and is considered to ensure that the operational level of the plating bath is sustained. For a plating bath solution that is at 100% efficiency and is chemically balanced at the beginning of the process, its efficiency will decline as plating occurs and the bath chemistry is consumed [15].

The operating temperature is one of the two main operating parameters that determines the success of an electroless plating process [15]. Sudagar et al. [10] has reported that temperature greatly influences the rate of deposition, stating that the deposition rate increases exponentially with increased temperature, as other parameters remaining constant. A lower temperature, below 60 °C, provides insufficient energy for the reactions to take place. On the other hand, a higher temperature can lead to an excessively active bath, potentially resulting in a “plate-out” effect or bath decomposition [15], [25]. There is an operating temperature range for electroless nickel plating where the bath operates effectively. However, a bath temperature should not exceed 92 °C where it becomes difficult to maintain the pH of the solution, causing the quality of the coating to deteriorate [9].

The other main operating parameter is the pH of the plating bath. Certain types of electroless plating require an acidic bath to achieve practical and quality deposition, while others require an alkaline bath, therefore, the operating pH is a key parameter in a plating bath. The pH also influences phosphorus content in the deposit. A higher phosphorous content is produced at lower pH values, and conversely, lower phosphorous contents are

produced when operating at higher pH values [15]. Chen et al. [26] has found that a phosphorous content of up to 25% can be obtained in an acidic bath at a pH of 4, while at a pH in the higher alkaline range, less than 1% phosphorous content is observed. Another study had proven the reliance of the good adhesion characteristics to steel of coatings from acidic baths on the bath pH [27].

Proper pre-treatment of the substrate is required in order to achieve strong adhesion between the deposited coating and the substrate. The metal substrates, such as steel, need to be ground with abrasive grit paper then finely polished with diamond suspension solutions to ensure a smooth surface for coating deposition. To prepare for plating, the substrates should be treated with an alkaline cleaning solution, consisting of sodium hydroxide or sodium carbonate, followed by an acid etch using sulfuric acid or hydrochloric acid. Other substrates may necessitate a different pre-treatment process, depending on the material of the substrate [12], [28].

2.1.3 Properties of Electroless Ni-P Coatings

The properties of the Ni-P coatings are greatly influenced by their phosphorus content, which is dependent upon plating parameters and bath composition. Coating deposits containing between 1–5 wt.% P are referred to as low phosphorus Ni-P, while coatings between 6–9 wt.% P are medium phosphorus Ni-P, and 9–11 wt.% P are high phosphorus [6]. The densities of Ni-P coatings range from 7.75 gm/cm^3 for high phosphorous deposits to 8.5 gm/cm^3 for low phosphorus deposits [10].

Electroless Ni-P coatings exhibit high wear resistance due to their typically high hardness. One major drawback of electroless Ni-P coatings is their low toughness and low ductility. This is more pronounced in low phosphorus coatings. Higher phosphorus content is associated with lower hardness and higher ductility [28], [29]. The Vickers hardness (at 100 g load) of Ni-P coatings ranges from 500 to 600 HV_{100} and the ductility ranges from 0.7% elongation to 1.5% elongation. Both properties depend on the phosphorous content and can be improved through post-deposition heat treatment [28], [29].

The phosphorus content also influences the degree of crystallinity of the deposited coatings. High phosphorous coatings are amorphous and low phosphorous coatings are

microcrystalline, while medium phosphorus coatings typically have a structure that is mixture of crystalline and amorphous [6], [30]. The amorphous nature of Ni-P coatings promotes ductility and corrosion resistance [29]. Ni-P coatings in general possess good corrosion resistance due to their amorphous structure as amorphous materials often exhibit better corrosion resistance than equivalent polycrystalline materials due to the lack of grain boundaries. Therefore, high phosphorus Ni-P coatings possess the highest corrosion resistance compared to lower phosphorous content [28], [31].

Electroless Ni-P coatings also possess excellent frictional properties due to the natural lubricity provided by their phosphorous content, which adds to the wear resistance and is very beneficial in applications where high lubricity is required. Ni-P coatings' coefficient of friction against steel is 0.12–0.13 and 0.43-0.44 for lubricated and unlubricated conditions, respectively [10], [28].

2.2 Composite Ni-P Coatings

Electroless composite coating is the incorporation of uniformly distributed second phase particles into the metallic matrix of the electroless coating during the plating process. The composite materials may be hard particles or nonmetallic materials [10]. It has been widely researched and proven to improve the tribological properties of the electroless coatings through dispersion strengthening and modifications of coating characteristics. This has introduced a new generation of electroless coatings and a potential for further improvements in the performance of the coatings in a wide range of applications [32], [33].

Composite coatings are achieved through the impact and settling of the second phase particles on the surface of the substrate, before being surrounded by the metallic matrix as it undergoes deposition. There are no molecular bonds between the metal matrix and the dispersed particles [10]. The uniform distribution of the second phase particles is accomplished by the use of magnetic agitation, stirring, and surface modification of particles using a surfactant to avoid agglomeration [32].

It was reported that the addition of those particles in the electroless bath increases the surface area loading by more than two orders of magnitude, which caused early work

in this area to be unsuccessful as plating baths became unstable and decomposed, until appropriate stabilizers were used to prepare the coatings [34].

Many researchers have studied composite coatings in electroless nickel and the effect of the incorporation of second phase particles on the mechanical and tribological behavior and of the coatings. Hard ceramic particles, such as silicon carbide, chromium carbide, diamonds, and alumina, are used as reinforcements in electroless coatings, as well as solid lubricant polymers like polytetrafluoroethylene (PTFE) and graphite [10], [35]–[39].

2.2.1 Factors Affecting Composite Coatings Quality

The key factors influencing electroless composite coating are as follows [10]:

- Bath stability.
- Agitation.
- Size of particles.
- Concentration of particles.
- Surfactants.

Bath stability is affected by the increase in the surface area loading due to the addition of the particles, causing the plating bath to decompose [10]. Agitation plays an important part in this process to ensure that the particles are uniformly distributed in the matrix. The particles are kept in suspension by being subjected to agitation as they are incorporated in the deposit, and the materials should be arranged in a way where the surface is facing upwards [10], [40]. It is suggested that if the agitation is too high, it can affect the quality of the deposit negatively, even in a bath with optimal loading and appropriate stabilizer concentration [41].

The size of the particles is an essential factor. Reddy et al. [42] suggested that the integrity between the matrix and the second phase particles can be improved with smaller particles as they are more easily held by the matrix. Apachitei et al. [38] reported that better incorporation was achieved by spherical shaped alumina particles than irregularly shaped particles, resulting in more favorable properties, namely much improved hardness. The shape of the particles also influences the coating, with respect to the surface finish, as small

round particles produce smooth surfaces and larger angular particles produce rougher surfacer [10], [38]. Balaraju et al. reported that alumina particles with size 50 nm resulted in superior corrosion resistance than 1.0 μm particles in Ni-P composite coatings, with no significant change in hardness [43]. The particles size is ideally large enough to settle during the deposition process with the nickel and phosphorous, but it should not be too large to significantly increase the roughness of the coating surface [28], [34].

The concentration of the second phase particles affects their incorporation into the matrix. Agglomeration of the particles may occur if a certain critical concentration is reached or exceeded, as the particles become closer to each other, leading to their settlement, and eventually saturation or lower degree of incorporation [44], [45]. Every composite material has its suitable concentration, that is determined experimentally, to achieve favorable results. For example, the optimal concentration of SiC in Ni-P coating was found to be 20–25 vol.% to obtain the maximum hardness. Similarly, the optimal concentration of PTFE is 20–25 vol.% to lubricate the plated part and reduce the friction [10], [46].

Surfactants are additives that are used to ensure that the second phase particles are uniformly distributed in the metallic matrix, and to avoid agglomeration of the particles. They are particularly necessary if the particles used for reinforcement are soft particles like PTFE or graphite [47], [48].

There are several ways of determining the level of incorporation of the second phase particles reported in the literature. One way is using a plasma emitting spectrum analyzer to determine the coating composition directly [49]. Another method is particle counting by observing the surface morphology of the coating [50]. Furthermore, electron microprobe analyzer can also be used [51], as well as observing the coating cross-section using image analysis [52]. The second phase particles' weight percentage in the deposit can be determined by dissolving a known weight of the coating in nitric acid, then filtering through a weighed 0.1 μm membrane filter [53].

2.2.2 Properties of Composite Coatings

2.2.2.1 Hardness

One of the main benefits of composite coatings is the ability to improve the hardness of the deposits. The hardness is influenced by the amount of the second phase particles, as well as the phosphorus content in the matrix and, in some cases, the subsequent heat treatment [10]. The addition of hard particles, such as SiC, increases the hardness of the coating at any phosphorus content, whereas the addition of soft particles, such as PTFE, with the purpose of reducing friction, lowers the hardness [54]–[56].

Huang et al. [56] investigated the electroless nickel composite coatings of both SiC and PTFE on a mild steel substrate and found that the hard ceramic SiC improved hardness from 453 HV_{50} to 530 HV_{50} (a 17% increase), while PTFE reduced it to 340 HV_{50} (a 25% decrease). Heat treatment of the SiC composite coating at 400 °C for one hour was found to increase the hardness considerably from 956 HV_{50} to 1365 HV_{50}, a 43% increase in hardness. Apachitei et al. [38] studied the composite coating Ni-P- Al2O3 with alumina dispersed in the Ni-P matrix, on an aluminum alloy substrate, and found that the hardness improved from 600 HV_{100} to 743 HV_{100}, a 24% increase in hardness, in the as-plated sample. Heat treatment at 400 °C for one hour resulted in a 10% increase in hardness from 1136 HV_{100} to 1248 HV_{100}.

2.2.2.2 Wear Resistance

Another main advantage of electroless composite coatings is improving the wear resistance for applications where the components are subjected to wear and abrasion [10]. The co-deposition of various hard particles was studied, and it was found that wear resistance similar to hard chromium can be achieved in electroless composite coatings. Figure 2–2 compares the Taber wear index, representing the rate of wear, of multiple electroless nickel composite coatings with hard chromium, as well as the monolithic Ni-P coating, to illustrate the effect of the different second phase particles on enhancement of wear resistance [10], [57], [58].

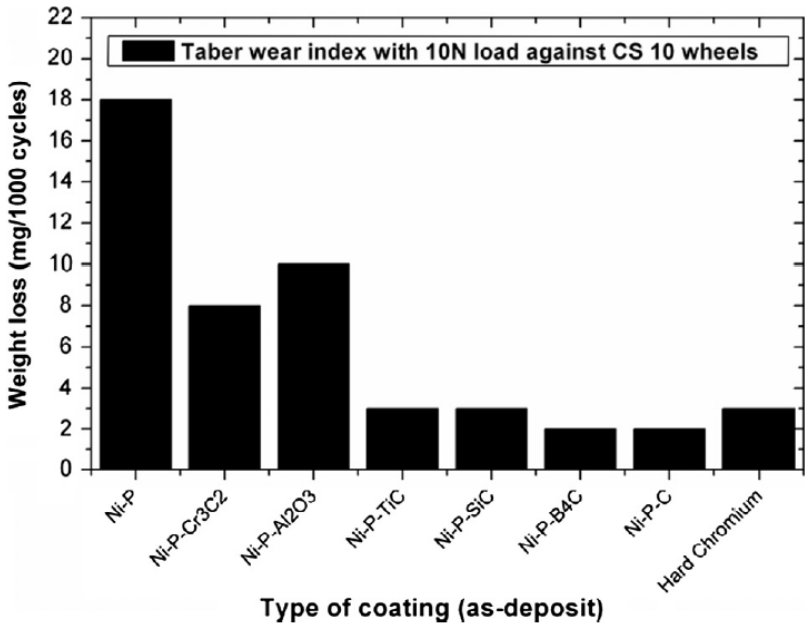

Figure 2 – 2: Wear rates of electroless nickel composite coatings [10].

The wear resistance of composite coatings is influenced by several factors including the type of co-deposited particles, their size, and their concentration, similar to their effect on hardness [10].

SiC is incorporated commonly in electroless coatings and studied extensively as its addition provides superior wear resistance proving to be beneficial in wear applications [10]. It has been reported that higher incorporation levels result in an increase in wear resistance, due to the dispersion strengthening effect of the particles [54], [59], [60]. Huang et al. [56] found that the incorporation of SiC particles in electroless nickel results in an 82% decrease in wear rate, from 2.52 to 0.45 10^{-6} mm^3 N^{-1} m^{-1}. However, they have also found that the incorporation of the softer PTFE instead results in lowering the wear rate further to 0.36 10^{-6} mm^3 N^{-1} m^{-1} (85% decrease), while sacrificing a considerable amount of hardness, as mentioned earlier.

Reddy et al. [42] studied the effect of the particles' size on the wear resistance of the deposits by incorporating different sizes of diamond particles in Ni-P matrix, ranging from 3 μm to 40 μm. They found that finer particles between 3-6 μm exhibit better wear resistance than larger particles of 20-40 μm size, given the coating thickness is equal. This

was attributed to the degree of incorporation of the diamond particles for a certain thickness being higher for the smaller diamond particles.

The wear of electroless Ni-P composite coatings occurs in two steps. The coating undergoes mild abrasive wear damage relating to the surface durability, followed by more severe wear that is characterized by the brittle detachment of debris [10], [61].

2.2.2.3 Friction

One of the purposes of composite coatings is to provide even better lubrication to electroless Ni-P coatings and to reduce the coefficient of friction, which is advantageous in unlubricated conditions or under prolonged friction where Ni-P coatings would fail. Unlike hardness, more favorable friction properties are obtained with the incorporation of soft particles. Graphite and PTFE are commonly used to provide good lubrication in composite coatings as they are able to prevent adhesion between the mating surfaces [10].

The co-deposition of hard particles, such as SiC, results in poorer lubrication properties for the composite coatings than the monolithic ones. Grosjeana et al. [37] studied this effect in Ni-P-SiC composite coatings and attributed the increase in friction to the abrasive properties of the carbide particles. Huang et al. [56] compared the effect of SiC and PTFE particles individually in electroless nickel coating and found that the average coefficient of friction for PTFE particles (0.48) is significantly lower than for SiC (0.59). They obtained an intermediate value of 0.52 for the friction coefficient with the incorporation of a combination of both particles. Other second phase particles used in electroless composite coatings to provide better lubrication include carbon nanotubes and boron nitride [10], [62], [63].

Surface roughness is an important parameter that influences the coefficient of friction as it provides the contact area between materials. It is usually considered when determining the quality of the coating. Composite coatings with soft particles have lower surface roughness, relative to monolithic electroless coatings, while hard particles produce rougher surfaces [10], [64].

2.2.2.4 Corrosion Resistance

Corrosion resistance is one of the advantages of electroless coatings. However, composite coatings are being developed to further improve this property in order to be used in more challenging applications [65].

Electroless coatings are naturally passive and very corrosion-resistant in a wide range of temperatures and pH values [66]. A group of researchers believed that the incorporation of second phase particles in the matrix would reduce the passivity and corrosion resistance, thus resulting in significantly less corrosion resistance for the composite coating, compared to the electroless nickel. Therefore, composite coatings were not normally recommended for applications requiring high corrosion resistance [67]. However, several electroless composite coatings were developed and found to have enhanced the corrosion resistance, leading to more research into composite coatings with the objective of increasing the corrosion resistance [67]–[71].

Balaraju et al. [67] evaluated the corrosion resistance of electroless Ni-P-Si3N4, Ni-P-CeO2, and Ni-P-TiO2 composite coatings, comparing them to electroless Ni-P. All three composite coatings exhibited much higher corrosion resistance in a 3.5 wt.% NaCl solution at room temperature. This was attributed to the decrease in the effective metallic area available for corrosion. The co-deposition of Si3N4 and CeO2 particles resulted in higher corrosion resistance than the TiO2 particles.

Mohammadi and Ghorbani [72] investigated the effect of the incorporation of PTFE and MoS_2 particles, separately and combined, into electroless nickel coatings regarding the corrosion resistance in acidic and brine solutions. The PTFE composite coating showed improved performance due to the particles blocking the pores of the electroless coating. However, the MoS_2 particles led to poorer results and the combination of both particles led to extremely poor corrosion resistance with five and ten times the corrosion rate of the monolithic coating in the acidic and brine solutions, respectively. This adverse effect was ascribed to some porosities existing in the coatings.

More composite coatings were developed with the objective of protecting pipeline steel from corrosion through the co-deposition of Graphene and titanium by Masry et al.

[66]. The corrosion performance of Ni-P-Ti and Ni-P-Graphene composite coatings were measured using polarization methods and electrochemical impedance spectroscopy in a 3.5% NaCl solution and compared to Ni-P coating. The composite coating with titanium showed superior corrosion resistance to the monolithic coating, and the graphene particles provided the best corrosion resistance. Composite coatings with polymer particles, like polyvinyl chloride and polyvinyl alcohol were also found to enhance the corrosion resistance of electroless Ni-P coatings [73].

2.3 Tribaloy Alloys

The Tribaloy alloys are a series of cobalt-based alloys, or less commonly nickel-based, containing a large volume fraction of a hard intermetallic Laves phase that is dispersed in a softer solid solution cobalt matrix that allows the alloy to withstand challenging and unlubricated conditions. They exhibit high strength, hardness, as well as corrosion and wear resistance at a wide range of temperatures, due to their unique microstructure and alloying elements [74], [75].

Tribaloy alloys are used extensively in coating and cladding applications in various industries including the automotive and aerospace industries, as well as uses as hard-phase particles in powder metallurgy of automotive valve seats and other drivetrain components that requires outstanding wear performance at elevated temperatures [75]. Tribaloys are developed primarily for applications where components are used under a combination of extreme wear, high temperatures, and corrosive environments, where direct lubrication is not possible, withstanding temperatures of up to 1000 °C [76], [77].

The main alloying elements of the Tribaloy alloys are chromium, molybdenum, and silicon, each influencing the mechanical properties and the microstructure significantly. The chromium content improves the corrosion resistance, while the addition of molybdenum and silicon improve the wear resistance [74]. High molybdenum accounts for the outstanding dry running properties of these alloys, making them suitable in adhesive metal-to-metal applications [77].

2.3.1 Laves Phase

The intermetallic Laves phase present in cobalt-based Tribaloy alloys have varying proportions in the microstructure for different alloys. They are characterized as the C-14 (MgZn2) type and its compositions are approximately CoMoSi and/or Co3Mo2Si [74]. Higher content of molybdenum and chromium favors the formation Laves phase [78]. They have high hardness values, up to 1000–1200 HV [79], and high melting point of about 1560 °C [74]. Tribaloys are usually hypereutectic, and the different variations consist of between 30–70 vol.% of the primary Laves phase [74], [80].

The presence of this phase greatly influences all the material properties. It is primarily responsible for the excellent abrasion resistance, however, it limits the alloy's ductility and impact strength [81]. Both molybdenum and silicon are added at levels exceeding their solubility limits to promote the precipitation of the Laves phase. Chromium is split up to about a third in the Laves phase and two thirds in the solid solution, and its addition improves the corrosion resistance of both phases individually, and therefore, the overall corrosion resistance of the alloys [81]–[83].

The primary dendrite of the Laves phase in the alloy is a hexagonal structure, while both the face centered cubic and hexagonal close packed crystal structures of cobalt can be present, depending on the heat treatment, due to the cobalt's allotropic nature. This forms a eutectic matrix of smaller intermetallic particles distributed in a cobalt solid solution. Also, there are regions of cobalt solid solution present that are free from the secondary Laves phase [74], [84], [85]. Figure 2–3 depicts the microstructure of a Tribaloy T-800 coating deposited by laser cladding showing the Laves phase dispersed in solid solution cobalt matrix.

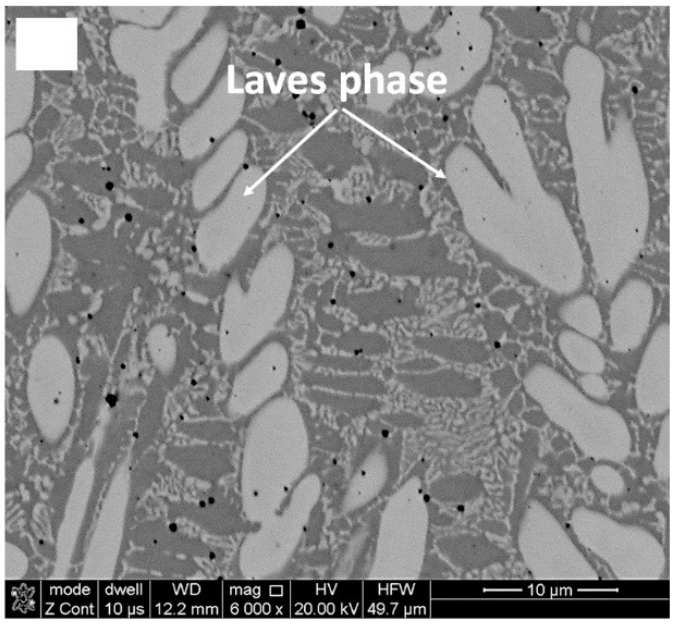

Figure 2 – 3: Microstructure of Tribaloy [76].

2.3.2 Types of Tribaloys

Two of the most common commercial types of Tribaloy alloys are T-400 and T-800 alloys. They are considered wear resistance alloys that depend on a large fraction of the intermetallic Lave phase dispersed in the cobalt solid solution for their properties. Both alloys vary in their composition, and thus, their properties [74], [76].

T-400 is composed of 8.5 wt.% Cr, 2.6 wt.% Si, 28.5 wt.% Mo, and balance Co. Its microstructure consists of about 35% of the Laves phase dispersed in the softer cobalt alloy matrix. This alloy is designed for outstanding wear performance in metal-to-metal contact at high temperatures. The high cobalt and molybdenum content and high laves phase percentage results in very high hardness with reasonable workability, and a relatively lubricious surface due to the formation of molybdenum oxides at high temperatures [74], [75], [82].

T-800 is composed of 17.5 wt.% Cr, 3.4 wt.% Si, 28.5 wt.% Mo, and balance Co. Its microstructure consists of about 60% of the Laves phase. This composition exhibits the largest content of the Laves phase providing it with high hardness and wear resistance. This alloy is designed for the highest possible service temperature out of all the Tribaloy alloys, with the ability of operating at temperatures up to 1000 °C for certain environments. The

Laves phase itself has a melting point of about 1560 °C, which helps the alloy retain its wear resistance up to high temperatures. In T-800, 10% of the cobalt content of T-400 is replaced with chromium, providing additional protection against oxidation, while sacrificing some of the workability provided by high cobalt content [74], [76], [77], [82].

Tribaloy T-800's higher fraction of Laves phase and higher chromium content than T-400 results in an alloy with higher hardness, better corrosion resistance and wear resistance. Hardness values are HRC 55 and HRC 60 for T-400 and T-800, respectively [74], [81]. However, the Laves phase is brittle, therefore, the higher content has a disadvantage since it favors the brittle crack formation and propagation. This tendency for brittle behavior makes the coating processes more difficult since cracking must be avoided especially in small parts [84], [86], [87].

New types of Tribaloy alloys have been developed in order to mitigate this problem through modification of the alloy composition. One example is Tribaloy T-900, where the cobalt and molybdenum content is lowered and nickel is added. This alloy showed better resistance to brittle fracture and more improved plasticity than T-800, while sacrificing some hardness. Alloying T-800 with iron was also found to improve some properties. Adding iron to alloy in above 10 wt.% results in a significant alteration to the microstructure where the dendrites are refined and the Laves phase disappears causing the alloy to become more fracture resistant, while reducing the wear resistance and hardness [76], [88].

Research was done by Xu et al. [74] to develop two new cobalt base Tribaloy alloys as an improvement on the T-400 alloy through altering its chemical composition in an attempt to improve the ductility, fracture toughness, and corrosion resistance, with the expectation that wear resistance, a necessity in some applications, may be reduced as improvements in one aspect is often achieved at the expense of another [74], [80]. For the first alloy, T-401, the amounts of silicon and molybdenum were reduced greatly to decrease the percentage of the Laves phase. Chromium was increased to increase corrosion resistance. The obtained alloy had a primary phase of cobalt solid solution, instead of Laves phase as is the case in most Tribaloys. This provided higher ductility, lower hardness, and lower wear resistance. The second alloy, T400C, had the same silicon content as T-400, but

with lower molybdenum content and higher chromium content. This alloy still had the Laves phase as the primary one, but the Laves phase fraction is less than the base alloy, which improves the ductility but lowers the hardness and wear resistance [74].

Tribaloy T400C was the focus of further research due to its enhanced oxidation and hot-wear resistance. It is advantageous in high temperature applications where excessive oxidation may cause sticking in moving parts [81]. It was shown that during the self-mated wear of this alloy, stable wear protective oxide films, or glazes, were formed on the surface [89]. In another study, this alloy showed excellent metal-on-metal wear resistance and less wear damage on the mating stainless steel alloy at 482 °C in a friction test [79]. It also showed significant improvement in corrosion resistance in several conditions [81], [90].

2.3.3 Tribaloy Coatings

Cobalt-based alloys are suitable to be applied as coating to provide better wear and corrosion resistance to components working under severe conditions [76]. Tribaloy coatings were initially deposited by thermal spraying, particularly High velocity oxygen-fuel (HVOF) spraying. However, thermal methods did not achieve good adherence of the deposited coating via metallurgical bonding with the substrate, due to characteristics of the process [91], [92].

By studying the tribological properties of HVOF-sprayed Co-Mo-Cr-Si coatings, Bolelli and Lusvarghi [93] found that the coating showed significant splat boundary oxidation due to exothermic oxidation reactions at a high temperature, and that it is mainly amorphous. The coating had low hardness and toughness and exhibited poor tribological performance. Significant adhesive wear was observed through pin-on-disk testing, and the coefficient of friction became very high, raising the contact point temperature up to the critical oxidation temperature, thus causing rapid oxidation. Post-spraying heat treatment of the coating at 600°C increased the microhardness, reducing the adhesive wear rate and the friction coefficient.

Other studies have reported the use of laser techniques to apply Tribaloy coatings, with the potential for obtaining coatings with favorable properties [76]. Laser cladding is a process where a laser beam is used to melt the coating material together with the substrate

at a controlled thickness [94], achieving a high temperature gradient at the coating–substrate interface and rapid cooling of the coating material [95]. It produces a strong microstructure refinement, solid solution supersaturation in alloying elements and high residual stresses in the coating [96], [97]. Several studies have reported positive sliding and abrasive wear resistance for laser cladding of cobalt-based coatings [97], [98].

A study investigating the solid particle erosion behavior of T-400 coating deposited by laser cladding has found that this coating was susceptible to extensive erosive wear. This was attributed to the lack of feasibility of the coated material to plastic deformation during erosion [97].

One issue that arises in the laser cladding process is for Tribaloy alloys with a higher percentage of the intermetallic Laves phase to have a tendency of brittle fracture, as mentioned in the previous section for Tribaloy T-800. This presents a problem due to the substantial thermal stresses that occur during rapid cooling, which amplifies this tendency for brittle fracture [76].

To mitigate the cracking that is observed in T-800 laser cladded coatings as a result of residual stresses caused by the high temperature gradient as well as the rapid heating and solidification during this process, pre-heating of the substrate is suggested as a viable solution [99]. Laser cladding assisted with pre-heat (LCAP) entails heating the substrate before the laser irradiation of the coating and the substrate, with the pre-heat temperature being a vital parameter in reducing the amount of cracks formed, as deduced by several studies [97], [99], [100].

There is a lack of literature on the deposition of cobalt-based Co–Mo–Cr–Si alloys as reinforcement particles in composite coatings, either by electroplating or electroless plating, and the tribological/mechanical properties of the coatings.

2.4 Cracking and Toughening Mechanisms

2.4.1 Hertzian Contact

Fracture in brittle materials, such as electroless nickel coatings, is generally studied through indentation tests. Hertzian indentation tests using a spherical indenter have been utilized in studying the fracture of brittle materials, in addition to, evaluating a coating's ability to support static and dynamic loads, as hertzian contacts occur in practical applications such as in bearings and gears [28], [101].

Hertzian contact, developed by Hertz [102] in 1881 for elastic contact, is often used to approximately predict a material's behavior under elastic-plastic contact. Cracking types and damage modes that develop during the contact process can be predicted through the analysis of the Hertzian stress distribution [28]. This stress field is developed when two bodies, the indenter and the substrate, come into contact and it is influenced by the shape of the indenter. In order to analyze the stress distribution of the stress field between two elastic bodies in indentation contact, Hertz assumed that the surfaces are non-conforming, frictionless, and the strains are small and within the elastic limit [102], [103]. Figure 2–4 shows the Hertzian indentation process. Hertzian indentation analysis can also used to predict the initiating position and driving stresses of cracks [104], as well as, determining the propagation angle of hertzian cone cracks [105].

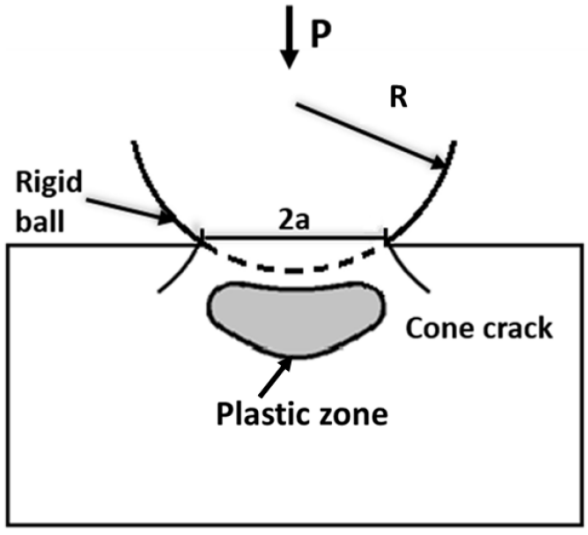

Figure 2 – 4: Hertzian indentation process [103].

Hertzian-type indentation testing is an effective method of characterizing the mechanical behaviour of brittle coatings [12] and will be used in this research to evaluate the coatings' fracture toughness and toughening mechanisms.

2.4.2 Crack Types

There are different types of cracks that may be generated on the surface of brittle materials under indentation contact. The five major types of cracks, according to Cook and Pharr [106], are: cone, radial, median, half-penny, and lateral cracks, as illustrated in Figure 2–5. Cone cracks, or Hertzian ring cracks, initiate on the coating surface as a ring crack just outside the area of contact then spreads downwards and outwards forming a cone shape at an angle that depends on the material's Poisson's ratio. They are typically generated by elastic loading of spherical indenters. Radial cracks initiate at the edge of the contact zone and propagate outwards. They are generated parallel to the loading axis, by spherical or sharp indenters. Median cracks usually occur under sharp indentation, and they are generated beneath the plastic deformation zone, then propagate parallel to the loading axis. Half-penny cracks are the result of median crack growth towards the surface, downward propagation of radial cracks, or merging of median and radial cracks. Lateral cracks are usually circular, and they are formed beneath the deformation zone, propagating parallel to the surface. They only occur during unloading, indicating that they are driven by residual stresses [12], [28], [103], [106]–[108].

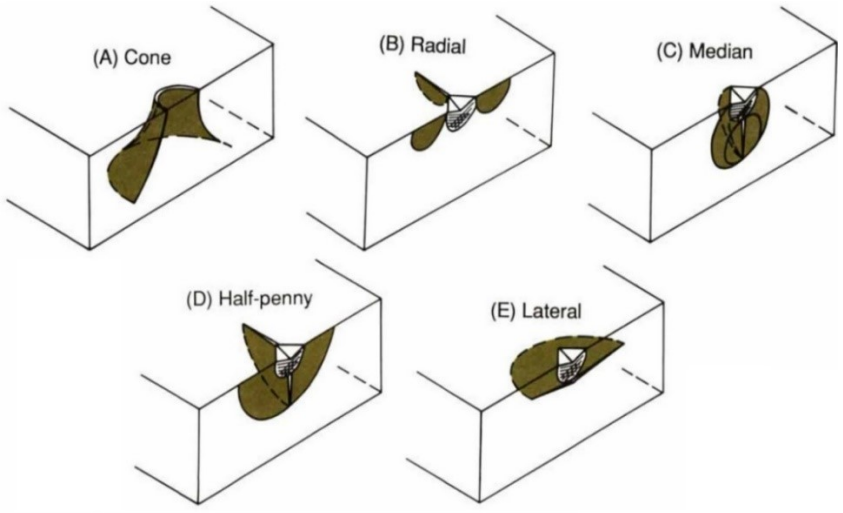

Figure 2 – 5: Crack types under indentation [106].

2.4.3 Toughening Mechanisms

Toughness is a major factor to be considered when evaluating the wear resistance of a material. The toughening of brittle materials can be achieved by the addition of second phase particles through several toughening mechanisms that involve the interactions between cracks and said particles preventing crack initiation and propagation, and in turn increasing the fracture toughness. The principle behind those mechanisms is diminishing the driving force that allows for the crack to propagate through the material after the initiation of the crack. Those mechanisms include micro-cracking, crack bridging, crack deflection, and crack arresting [28].

Micro-cracking allows for dissipation of the crack driving energy by breaking up major cracks into a series of micro-cracks. Their formation close to a large crack tip reduces the stress adjacent to it. The addition of second phase particles has been proven to promote micro-cracking and improving fracture toughness [109], [110]. Crack bridging involves the absorption of propagation energy by a particle as it is plastically deformed when it comes into contact with a crack. The energy lost by the crack going through the particle reduces the crack severity. With every instance of a particle's plastic deformation, there is less energy available for crack propagation until it eventually stops. High adhesion between the matrix and the second phase particles is required for crack bridging to take place [29], [111], [112]. Crack bridging is illustrated in Figure 2–6.

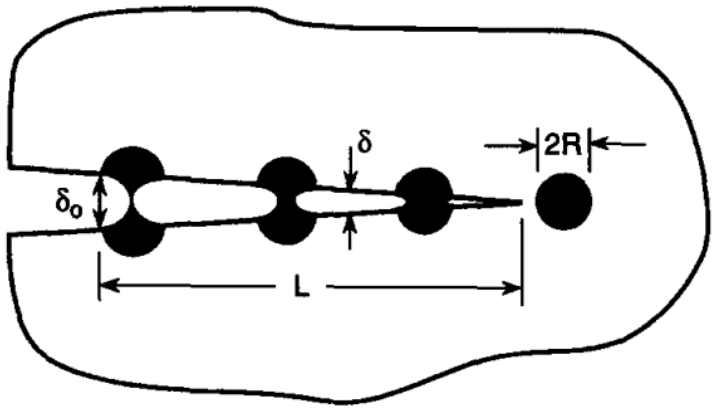

Figure 2 – 6: Crack bridging toughening mechanism [113].

Crack deflection is another toughening mechanism that is induced by second phase particles where the crack changes direction upon interacting with the particles. It can occur with or without direct contact. Deflection without contact occurs as the stress field at the crack tip causes elastic deformation of the particle, which absorbs the driving energy and deflects the crack tip. Deflection with contact occurs as the crack tip reaches the particle and causes its plastic deformation with a driving force that is insufficient to de-bond the particle. Figure 2–7 illustrates both cases of crack deflection. The deviation of the crack path consumes energy, thus depleting the driving force behind crack propagation. A crack is arrested when it loses its driving force completely upon contact with a particle [6], [28], [114], [115].

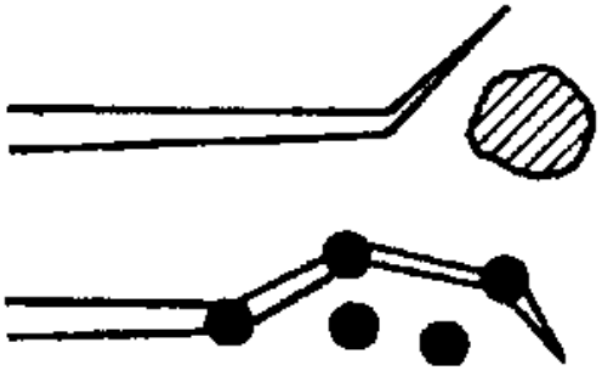

Figure 2 – 7: Crack deflection toughening mechanism [114].

The indentation behavior and stress fields of composite materials are more complex than that of monolithic materials and most models predicting their wear mechanisms are simplified [6]. Shen and Chawala [116] observed, during the indentation of a particle reinforced metal matrix composite, a local increase in the concentration of particles directly below the indenter in the deformation zone, as shown schematically in Figure 2–8 with SiC particles dispersed in an aluminum matrix. The increasing local density of hard particles resulted in a local increase in hardness and a reduction in the stress applied to the matrix.

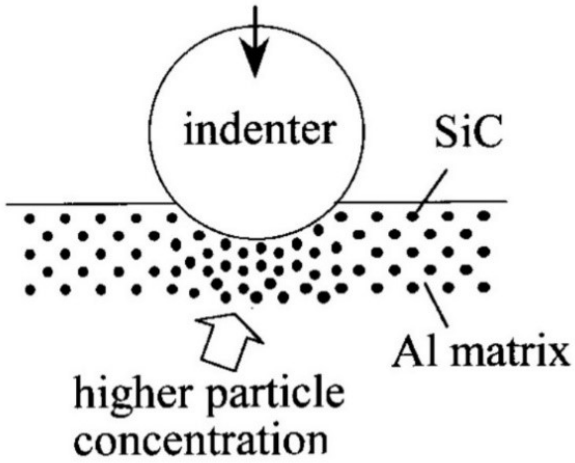

Figure 2 – 8: Schematic of particle concentration increase due to indentation [116].

2.5 Sliding Wear

2.5.1 Forms of Wear

Wear is "the surface damage or removal of material from one or both of two solid surfaces in a sliding, rolling, or impact motion relative to one another" as defined by Bhushan [117]. It is generally expressed in terms of the loss of material (mass or volume loss), although wear damage can occur due to material displacement with no change in volume as damage precedes material loss [117].

One of the types of wear is abrasive wear. It occurs as asperities on a harder/rougher surface are sliding against a softer surface [117]. Figure 2–9 shows the different wear mechanisms of abrasive wear according to Stachowiak and Batchelor [118]. Cutting refers to a harder asperity cutting the softer material forming a chip that is removed as wear debris. Fracture may occur when the abraded material is brittle. Moreover, a ductile material fails by fatigue when it is deformed repeatedly with a blunt grit as cutting is unlikely. Lastly, grain pull-out or detachment is a rare mechanism and is mainly found in ceramic materials [118]. The term plowing refers to the sideways displacement of the material from the surface forming a groove with a ridge on both sides. In an ideal case, micro-plowing due to a single pass of one abrasive particle does not result in material removal from the surface, in contrast to chip formation from cutting, however, material loss will occur by multiple abrasive particles acting simultaneously. [28], [117], [119].

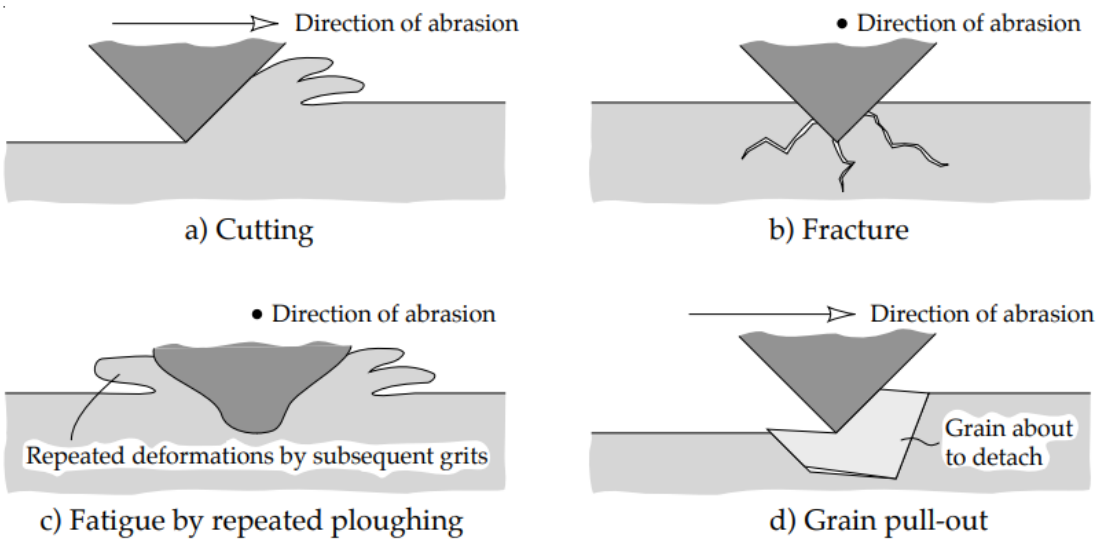

Figure 2 – 9: Possible mechanisms of abrasive wear [118].

Adhesive wear is another type of wear. It occurs when two opposing asperities become bonded to each other during sliding contact between two surfaces. The bonding, or adhesion, occurs at the point of contact and is sheared off by sliding, resulting in detachment and loss as debris from the softer material [117], [118].

One notable situation for abrasive wear is when the hard abrading surface is a third body, as opposed to a harder surface abrading a softer surface, and it occurs when loose hard particles are trapped between the two sliding surfaces, abrading one or both of them. This is referred to as three-body abrasive wear [117], [120]. In some cases, the initial wear mechanism is adhesive, followed by three-body abrasive wear resulting from the trapped particles from the adhesive wear [117].

2.5.2 Wear Testing

One way to evaluate wear in a material is scratch testing, where a sample is scratched with an indenter of a known radius, under various load conditions. The wear rate can be determined through measuring the scratch track width and subsequently calculating the volume loss in the sample. The scratch test can also be used to determine the coefficient of friction as well as to monitor crack initiation and propagation during the test using an acoustic emission sensor [117], [121], [122].

The low-stress abrasion testing, using the ASTM G65 standard, is a dry sand/rubber wheel abrasion test that is often used to simulate wear in different applications [119], [123], [124]. In low-stress abrasion, there is low applied contact pressure between the test specimen and the abrasive particles, and the particles remain unbroken during the wear process, as opposed to high-stress abrasion where they are crushed. Higher contact pressure is associated with deeper indentations and promotes the cutting mechanism [119], [120]. ASTM G65 test is a standardized abrasion test that allows for comparison of different materials based on their measured volume loss following this test procedure [124].

2.5.3 Delamination

Delamination can also occur in coatings at the coating–substrate interface when the coating bonding to the substrate is weak or under high loads [103]. It is defined as a "crack that forms between adjacent plies" [125]. Figure 2–10 shows an example of a delaminated coating from the substrate. This fracture can develop during unloading with the substrate's elastic recovery or develop due stresses caused by layer mismatch [103], [125]. For brittle materials, cracks initiate under the surface by shear stress, then propagate parallel to the surface, often extending to the surface causing delamination [28]. The shear stresses develop in or around the interface as a result of the difference in Young's modulus between the coating and the substrate, which is more pronounced when the substrate is more ductile than the coating layer [6], [126].

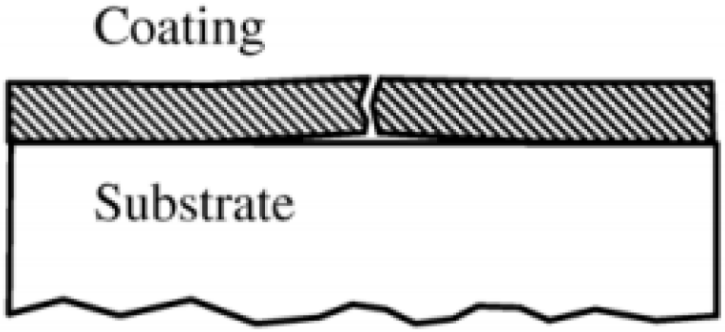

Figure 2 – 10: Illustration of coating delamination [6].

Chapter 3 – Methodology

3.1 Substrate and Powder Characterization

3.1.1 Low Carbon Steel Substrate

The substrates for all experiments were made of AISI 1018 steel. For the micro-hardness, scratch, and indentation tests, as well as the general characterization of the coating, the substrates used were discs of 16 mm diameter and 10 mm thickness. For the purpose of the low-stress abrasion test only, the substrates used were 25.4 mm by 76.2 mm rectangular specimens having a 12.7 mm thickness. The elemental composition of AISI 1018 low carbon steel is listed in Table 3–1. The steel substrate was etched and examined under confocal laser scanning microscopy (CLSM). The surface micro-structure of the AISI 1018 steel is shown in Figure 3–1. The substrate's micro-structure consists of α-ferrite and pearlite.

Table 3 – 1: Composition of AISI steel [127].

Element	Weight %
C	0.182
Mn	0.754
Cu	0.186
Cr	0.181
Si	0.095
P	0.040
S	0.021
Ti	0.008
Fe	Balance

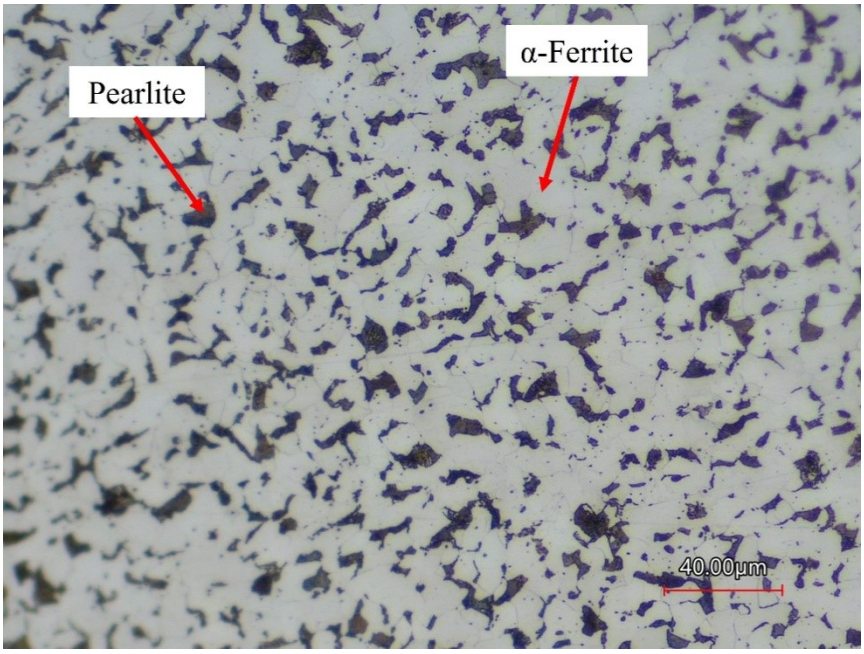

Figure 3 – 1: Microstructure of AISI 1018 steel.

3.1.2 Tribaloy Powder

Commercial CoCrMo powder supplied by Nanoshel UK Ltd. was used as a second phase particle in the composite coating. It was advertised to have a composition of 29 wt.% molybdenum, 17 wt.% chromium, 3.5 wt.% silicon, and balance cobalt. Inductively coupled plasma optical emission spectrometry (ICP-OES) was performed to analyze the chemical composition of the powder. The composition in weight % was found to be Co: 50.53%, Mo: 29.15%, Cr: 17.82%, Si: 2.50%. The particle size distribution of the powder is shown in Figure 3–2. The powder exhibits a bimodal particle size distribution. The two major particle sizes observed are approximately 3 µm and 40 µm, while some particles are larger than 100 µm. The values of D10, D50, D80, and D90 were found to be 1.65 µm, 7.21 µm, 39.1 µm, and 54.8 µm, respectively. Hitachi S-4700 (Hitachi High-Tech, Tokyo, Japan) scanning electron microscope (SEM) was used to examine the powder morphology of the supplied powder, shown in Figure 3–3. The powder morphology can be described as spheroidal, not perfectly spherical, and the broad size distribution can also be seen.

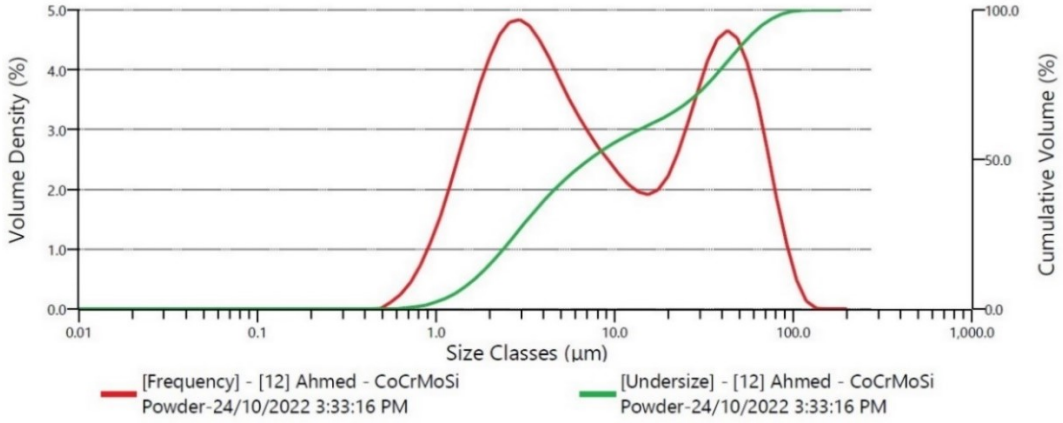

Figure 3 – 2: Particle size distribution of powder.

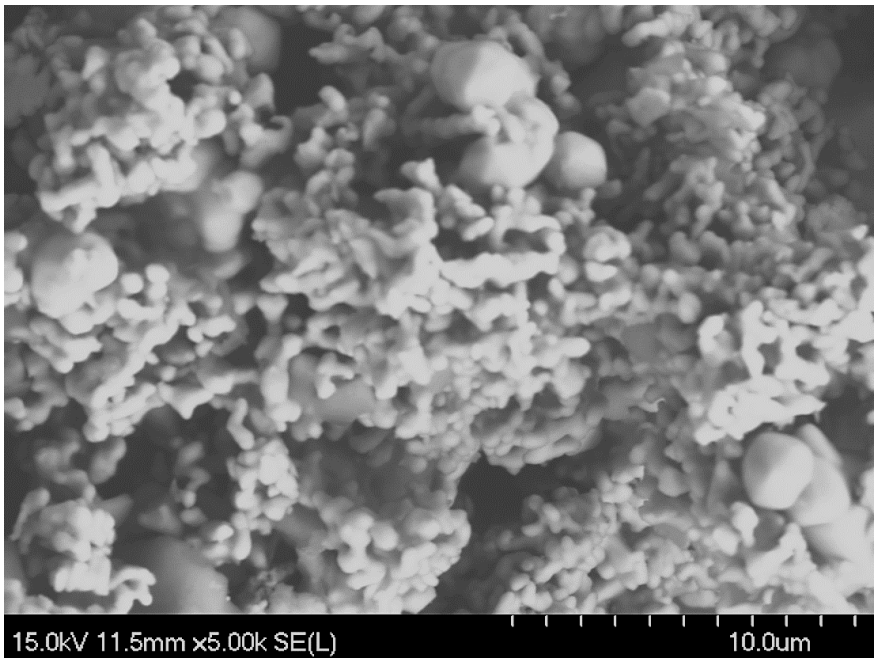

Figure 3 – 3: SEM image of the powder.

3.2 Coating Preparation

The coating samples were prepared as follows: each substrate was ground up to 600 grit SiC paper and polished using 9 µm, 3 µm, and 1 µm monocrystalline diamond suspension polishing solution. The substrates were then submerged in an alkaline cleaning solution at 80 ± 5°C for 5 minutes. The composition of the alkaline solution is 30g/L sodium phosphate, 50g/L sodium hydroxide, 30g/L sodium carbonate. Afterwards, the substrates were rinsed with distilled water then immersed in 20 vol% sulfuric acid for 15

seconds at room temperature. Following the pretreatment steps, the substrates were rinsed with distilled water and hung horizontally in the coating solution. A commercial electroless Ni-P solution containing sodium hypophosphite as the reducing agent and nickel sulfate as the source of nickel was used as plating solutions for both monolithic and composite baths. A thin layer of Ni-P was deposited as a pre-coat layer first in order to enhance the adhesion of the composite coating. Samples were kept in a 1 L Ni-P bath for 30 minutes then moved to a 1 L Ni-P bath containing 0.1 g/L of Tribaloy powder for 4 hours. The bath temperature was maintained at 88 ±2 °C and the pH at 4.7 ±0.2. Ammonium hydroxide (28–30%) solution was dripped into the plating solution periodically to adjust the pH. The plating bath was stirred at 300 RPM using a magnetic stirring bar throughout the coating process to keep the particles suspended in the solution and prevent agglomeration. The Monolithic Ni-P coatings were prepared following the same procedure except for 2.5 hours deposition time and stirring at 100 RPM. The coating set-up used in the deposition of coatings in this research is shown in Figure 3–4, including both 1 L coating baths and the heating equipment.

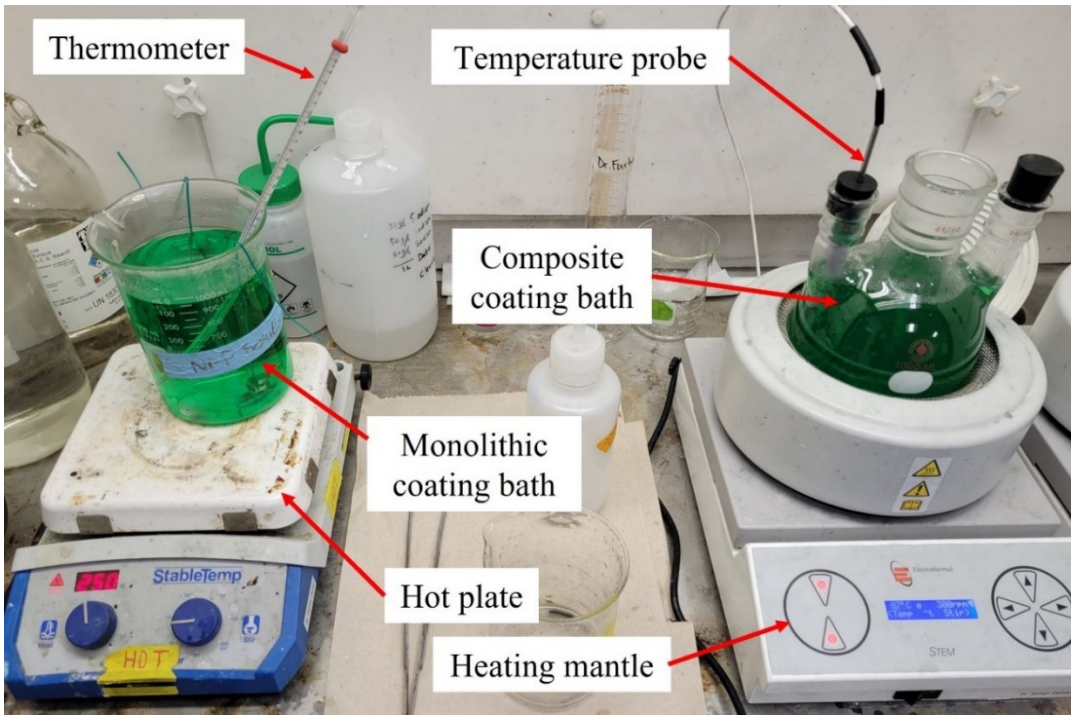

Figure 3 – 4: Coating deposition set-up.

Prior to conducting the tests described in this work, coating samples were polished using 600 grit SiC paper, 9 μm and 3 μm polish to ensure a flat surface for the tests to be carried out.

For the low-stress abrasion test specimens, the coating times were extended. The coating times were 40 minutes in the pre-coating bath and 4.5 hours in the composite bath for the Ni-P-Tribaloy coating samples, and 3 hours for the Ni-P coating samples. The coated samples were not polished following the deposition for this experiment.

3.3 Coating Characterization

Coating samples were sectioned using Buehler isomet 1000 precision saw with diamond blade at 250 RPM and a 200 g load for the analysis of the cross-section. X-ray Diffractometry (XRD) analysis was carried out on the composite coating surface, the monolithic coating surface, the Tribaloy powder, and the uncoated steel substrate. Each sample was scanned with Bruker D8 Advance diffractometer (Bruker Corporation, Billerica, MA, USA) using Cu Kα radiation with a wavelength of 1.54 λ. The scan angle ranged from 20°–120° to ensure that all peaks are included. Keyence (Keyence Corporation, Osaka, Japan) confocal laser scanning microscopy (CLSM), Hitachi S-4700 Scanning Electron Microscope (SEM), equipped with Energy Dispersive Spectroscopy (EDS) were utilized to examine the surface and the cross section of the coatings and to determine the coating composition. The surface topography and the surface roughness of the coatings were analyzed using the CLSM's 3D topographic scanning capabilities.

3.4 Micro-Hardness Testing

The hardness of each coating was measured using NANOVEA PB 1000 mechanical tester (NANOVEA Inc., Irvine, CA, USA). Micro-hardness tests were performed on both the composite and the monolithic coatings' surfaces with a Vickers indenter under an applied load of 6 N. Multiple tests were performed on each sample to ensure the repeatability of the results. Load–depth plots were generated for each measurement, and the hardness (GPa), elastic modulus (GPa), and maximum indent depth (μm) were determined for each sample and subsequently compared. The mechanical tester used in this

test is shown in Figure 3–5, and the indenter along with an example its produced indent in Figure 3–6.

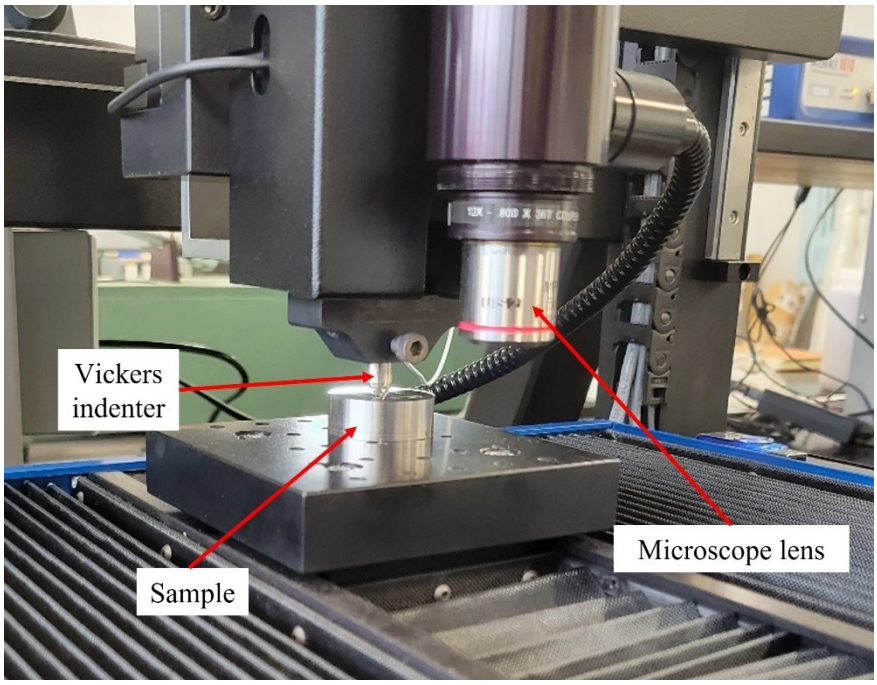

Figure 3 – 5: NANOVEA PB 1000 mechanical tester.

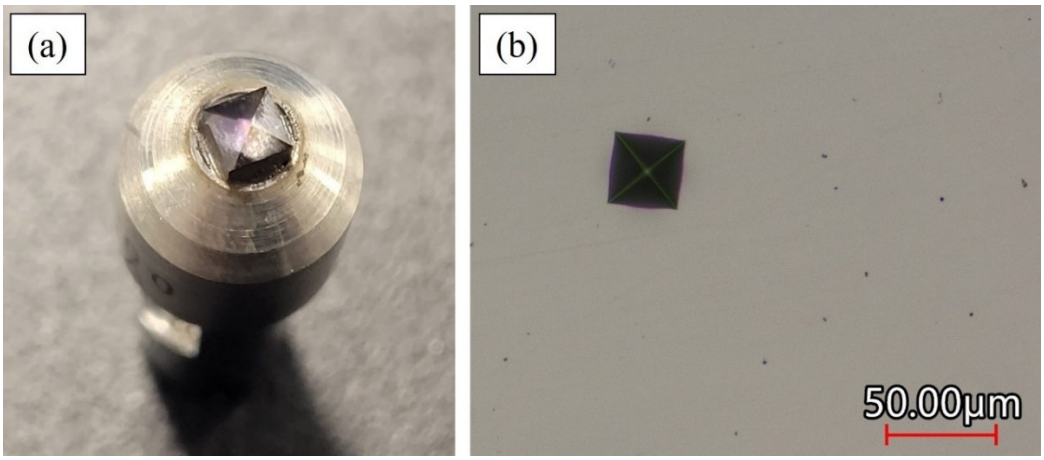

Figure 3 – 6: (a) Vickers indenter. (b) Example of produced indent.

The hardness and Young's modulus values can be determined analytically from the generated load–depth curves using the Oliver and Pharr method [29], [128]. A typical load–depth curve is provided in Figure 3–7, featuring elastic-plastic loading and elastic unloading.

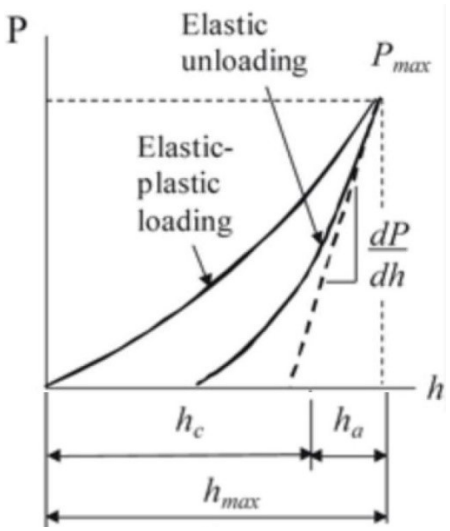

Figure 3 – 7: Typical load–depth curve [128].

Consider this curve, the gradient of the unloading curve is denoted by dP/dh and the maximum load applied by P_{max}. The maximum depth reached by the indenter relative to the surface (at the maximum load) is h_{max} and the indentation contact depth is h_c. The hardness, H, can then be calculated through the contact area by the following equations [29], [128]:

$$H = \frac{P_{max}}{A_C} \quad \text{(Equation 3–1)}$$

$$A_c = kh_c^2 \quad \text{(Equation 3–2)}$$

$$h_c = h_{max} - \left[\frac{2(\pi - 2)}{\pi}\right]\left[\frac{P_{max}}{dP/dh}\right] \quad \text{(Equation 3–3)}$$

Where A_c is the contact area between the indenter and the surface, k is a constant which is assumed to be 24.5 for Vickers indenter. Furthermore, the Young's modulus, E, can be calculated using the following equations [29], [128]:

$$\frac{1}{E^*} = \frac{1 - \nu^2}{E} - \frac{1 - \nu i^2}{E_i} \quad \text{(Equation 3–4)}$$

$$E^* = \left(\frac{dP}{dh}\right)\left(\frac{\sqrt{\pi}}{2\sqrt{A_c}}\right) \quad \text{(Equation 3–5)}$$

Where E* is the effective elastic modulus of the system, which is the combined modulus for the system. E_i and ν_i are the Young's modulus and the Poisson's ratio of the indenter, respectively. The tested material's Poisson's ratio, ν, is taken as 0.29.

3.5 Indentation Testing

PASCO ME-8236 (PASCO scientific, Roseville, CA, USA) materials testing apparatus, shown in Figure 3–8, was used to perform the indentation tests on the coatings' surfaces in order to investigate their indentation behaviour and crack formation. A spherical WC-6Co indenter with a radius of 0.795 mm was used to conduct the tests. A load of 2000 N was applied at an average loading rate of 0.5 mm/min. The applied indentation load can be considered as a quasi-static load as the loading rate was low. An acoustic emission (AE) sensor was attached to the samples during the tests to monitor cracking events.

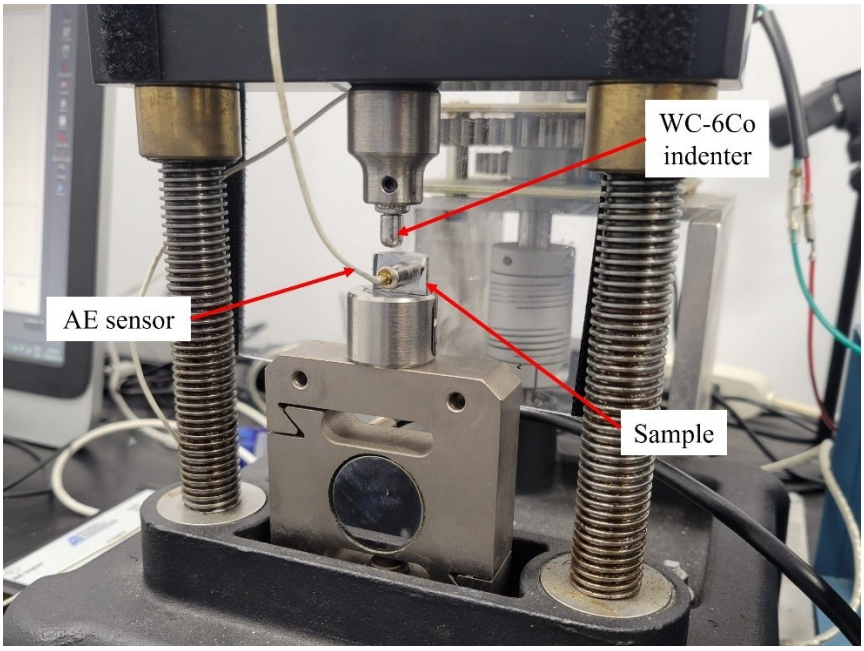

Figure 3 – 8: PASCO ME-8236 materials testing apparatus.

Following the indentations, the indented samples were sectioned, and both the surface and the cross section were analyzed using CLSM and SEM to examine the indents thoroughly. The PASCO Capstone (v1.4.1) software automatically recorded the load–depth data throughout the indentation process.

3.6 Scratch Testing

To evaluate the wear resistance of the coating, scratch tests were carried out using a Universal Micro Tribometer (UMT), shown in Figure 3–9. A sharp diamond indenter having a radius of 0.2 mm was used to perform the scratch tests with multiple passes, under a constant load of 1 kg. Each sample was subjected to five scratches with varying number of passes: 1, 25, 50, 75, and 100 passes. Each scratch had a sliding distance of 5 mm, and each pass took 30 seconds with the indenter sliding at a speed of 0.17mm/s. An acoustic emissions (AE) sensor was attached to the indenter to monitor the acoustic signals due to cracking during scratches. The coefficient of friction (COF) for each test was also recorded throughout the duration of the scratch.

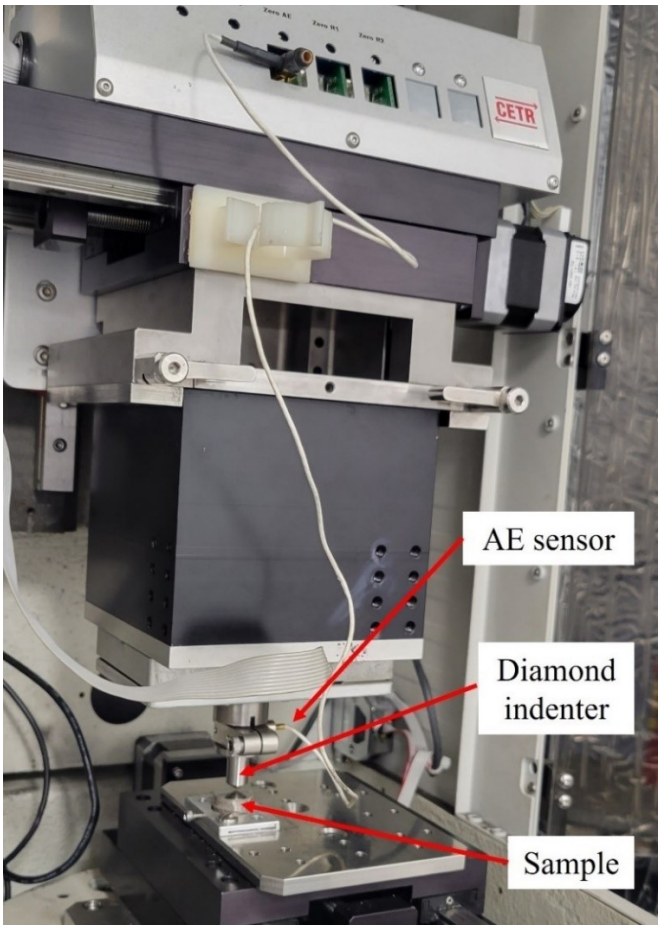

Figure 3 – 9: Universal Micro Tribometer.

CLSM and SEM were employed to characterize the wear tracks and to calculate the volume loss associated with each sliding distance. The volume loss was determined using

the CLSM's topographic scanning on the wear track. It can also be calculated based on the relationship between the indenter radius and the measured widths of the wear scars given by the following equation [129]:

$$\text{Volume loss} = \frac{D^2 t}{8}\left[2sin^{-1}\frac{b}{D} - sin\left(2sin^{-1}\frac{b}{D}\right)\right] \qquad \text{(Equation 3–6)}$$

Where D is the diameter of the indenter, t is the scratch length, b is the width of the scar measured by confocal microscopy.

3.7 Low-Stress Abrasion Testing

Low-stress abrasion tests were carried out according to ASTM G65 standard in order to evaluate the abrasion resistance using a dry sand/rubber wheel apparatus. A schematic diagram of the test apparatus is provided in Figure 3–10. The tests performed in this research followed procedure D as outlined in the ASTM G65 standard, which is a relatively lighter load variation of the test. This procedure is appropriate for thin coatings such as the coatings being tested here.

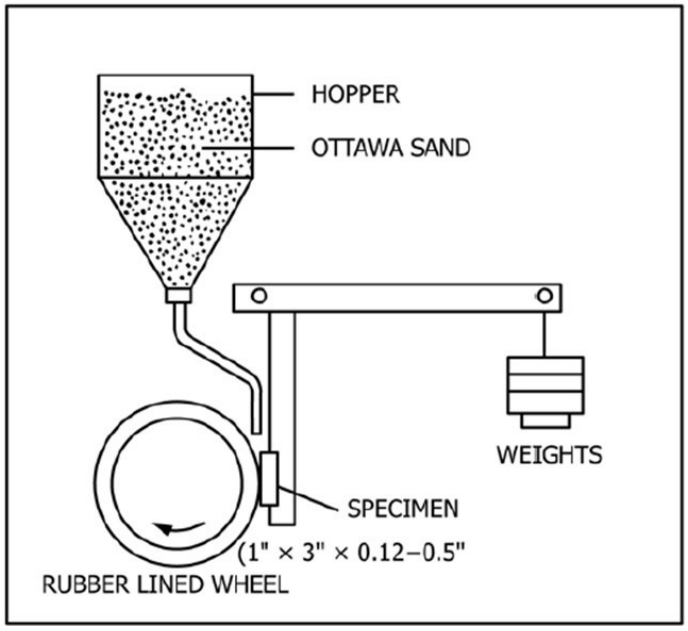

Figure 3 – 10: Schematic diagram of dry sand/rubber wheel test apparatus [124].

The force applied against the specimen in this test was 45 N, and the test was performed at 10 revolutions increments, at 200 RPM, until coating failure is observed, which is indicated by the exposure of the substrate underneath the coating layer. The samples were weighed between each step (10 cycles) and recorded to express the abrasion rate in terms of material loss. The volume loss was calculated by dividing the measured mass loss by the known density of the coating. A rubber wheel of 221.4 mm diameter and 12.84 mm width was used, along with semi-rounded Ottawa silica sand having an average particle size of 212–300 µm. The sand flow rate was between 300–400 g/min. The abrasive particle size distribution used in this test is provided in Figure 3–11.

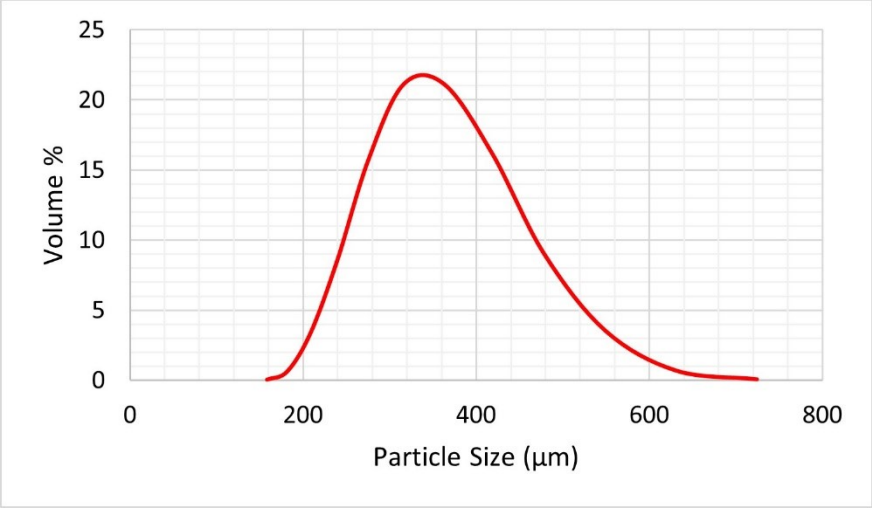

Figure 3 – 11: Ottawa silica sand particle size distribution.

After the abrasion tests, CLSM and SEM were used to examine both the surface and the cross-section of the abrasion wear scars for wear mechanisms analysis. CLSM's topographic scanning was used to produce 3D scans of the wear scars and examine the surface roughness.

Chapter 4 – Results and Discussions

4.1 Coating Characterization

Composite Ni-P-Tribaloy coatings were successfully plated on AISI 1018 steel substrates. Figure 4–1 shows the X-ray diffraction patterns generated from the steel substrate, Tribaloy powder, monolithic Ni-P coating, and composite Ni-P-Tribaloy coating as deposited. AISI 1018 steel reveals diffractions from the 110 and 200 planes. Here, the generated diffraction pattern shows the first two peaks occurring at 44.459° and 64.701°, which matches the Fe powder diffraction file (PDF ID: 00-006-0696). The monolithic Ni-P coating was mostly amorphous, having a broad peak at 44.775° extending from 42° to 48°, consistent with the literature and closely matching a nickel phosphide powder diffraction file (PDF ID: 04-003-6331). The broad peak in the form of a hill is a typical feature in amorphous materials [130]. The first high intensity peak observed in the as-received Tribaloy powder diffraction pattern occurs at 40.340°, followed by a smaller peak at 44.203°, and the next major peak observed at 73.570°. This fairly matches a $Co_{1.539}Cr_{0.549}Mo_{0.912}$ powder diffraction file (PDF ID: 00-026-0425). The Tribaloy powder exhibits diffractions from the 100, 111, and 220 planes, as indexed on the X-ray diffraction patterns. The Ni-P-Tribaloy coating was found to be mostly amorphous. It exhibited a broad peak similar to that of the Ni-P diffraction pattern from 42° to 48° that includes a smaller peak corresponding to the largest peak observed in the Tribaloy powder's diffraction pattern. The other Tribaloy peaks have lower intensity and are difficult to detect in the composite coating due to the low powder concentration. Also, the steel peaks are not detected due to the fact that the coating thickness is higher than the depth of the XRD beam penetration.

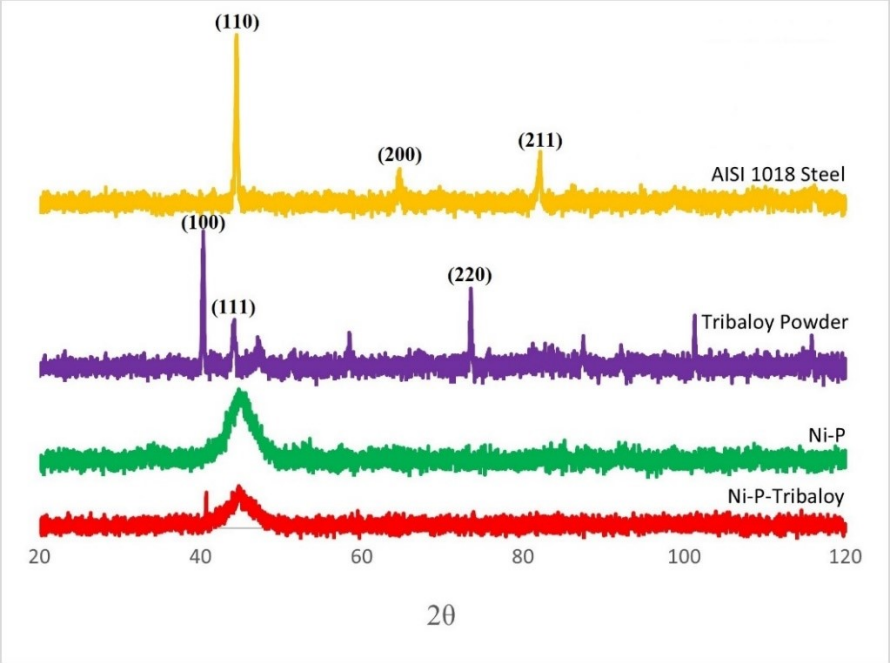

Figure 4 – 1: X-ray diffraction patterns for AISI 1018 steel, Tribaloy powder, Ni-P, and Ni-P-Tribaloy.

Figure 4–2 shows images of the Ni-P-Tribaloy coating surface and cross section after polishing with 3 μm monocrystalline diamond suspension polishing solution. It is clear that the second phase particles were successfully embedded in the coating matrix. The presence of the black areas seen in Figure 4–2 (a) is due to the surface roughness. The coating thickness was approximately 30 μm and the substrate–coating interface exhibits excellent bonding as seen in Figure 4–2 (b), evident from the distinct difference in color between the coating layer and the substrate. The addition of the Tribaloy particles resulted in a rougher surface, compared to the monolithic Ni-P surface. Using the Keyence CLSM's 3D topographic scanning, the surface roughness of the Ni-P-Tribaloy coating was measured and the surface topography shown in Figures 4–3 was generated, at 250% height magnification. The surface roughness Sa value was measured to be 2.30 μm based on four different aerial measurements of 1.49 mm^2. On the other hand, the Ni-P coating's Sa value was measured to be 0.430 μm, and its surface topography is shown in Figure 4–4 for comparison, also at 250% height magnification.

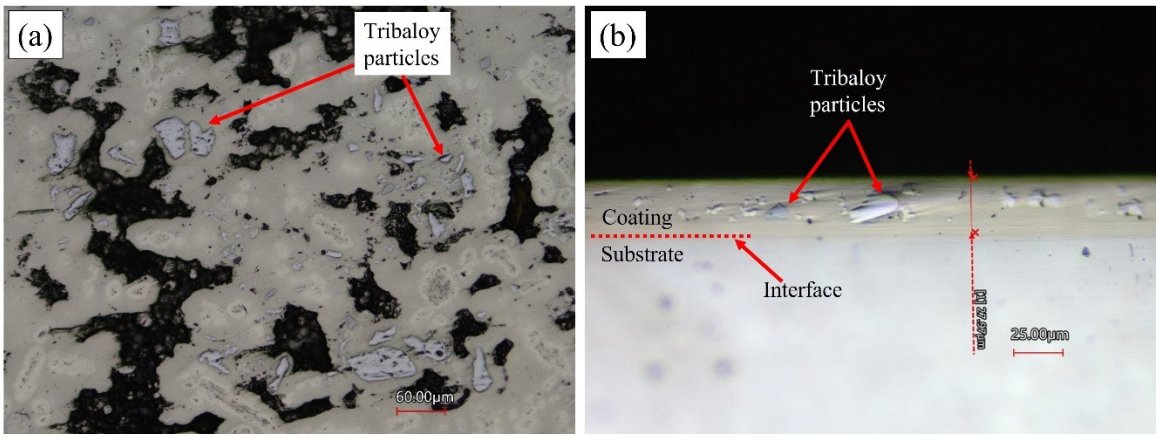

Figure 4 – 2: (a) Polished surface and (b) cross-section of Ni-P-Tribaloy.

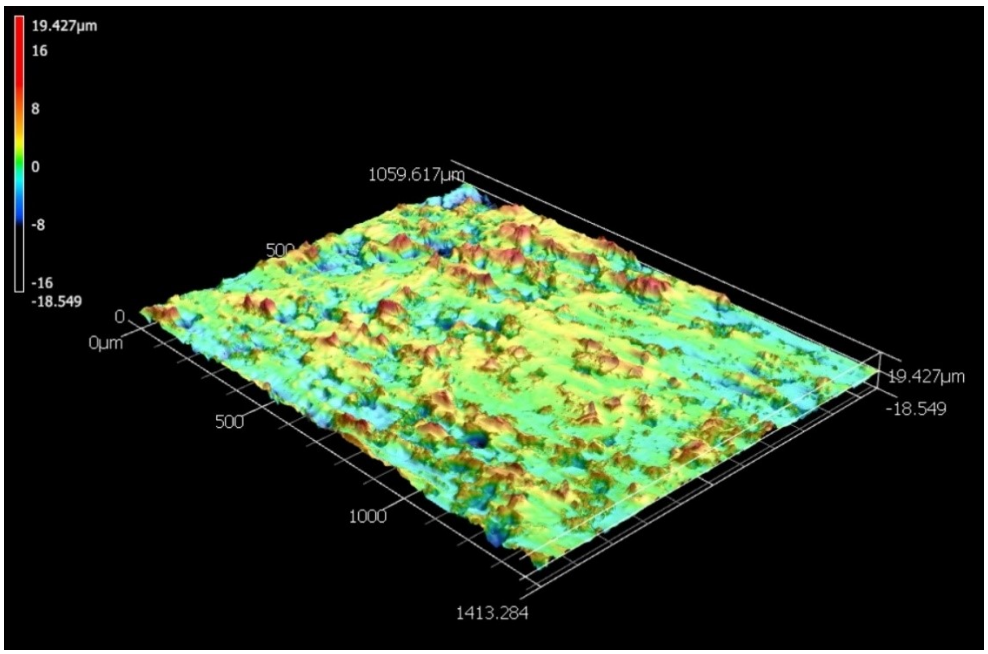

Figure 4 – 3: Surface topography of Ni-P-Tribaloy.

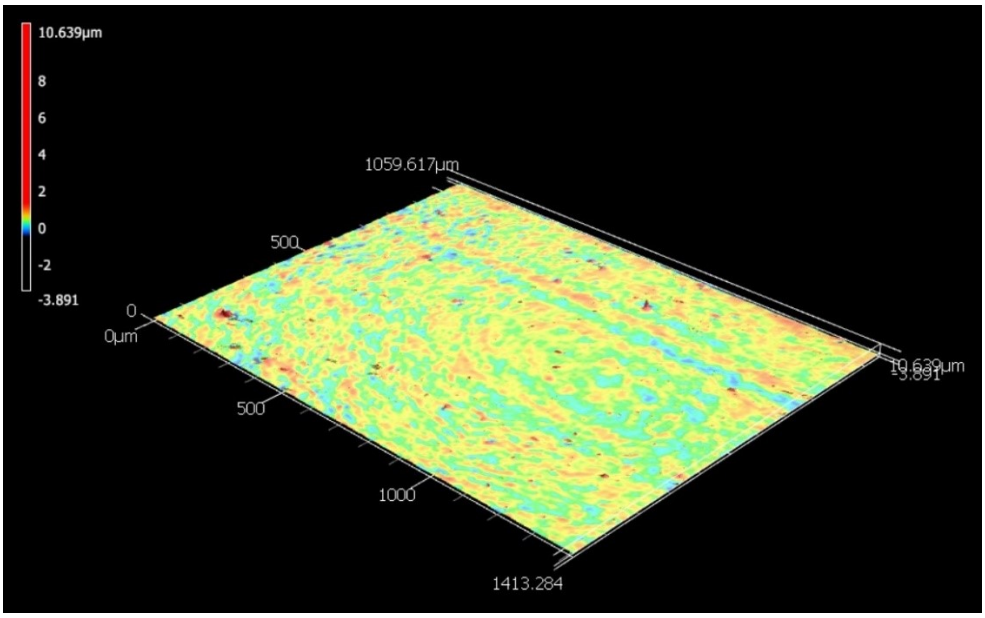

Figure 4 – 4: Surface topography of Ni-P.

EDS analysis was performed on the surface of the composite Ni-P-Tribaloy coating to determine its chemical composition. Table 4–1 contains the results of the EDS analysis and Figure 4–5 shows the results of the elemental mapping to visualize the distribution of the elements present. This reinforces the fact that the composite coating consists of the Ni-P matrix with second phase particles dispersed within the matrix. The presence of the four constituents of the Tribaloy was detected in the coating: Cobalt, Molybdenum, Chromium, and Silicon. The reason for the low cobalt content detected by EDS is due to peak overlap with nickel in the EDS spectra [131]. Adjusting for this based on the cobalt wt.% in the powder's composition (section 3.1.2), the cobalt content can be estimated to be 8.33 wt.% in the coating, and 74.6 wt.% for the nickel. Thus, the coating can be described as having 16.5 wt.% Tribaloy, which is equivalent to 15.7 vol.%, and its actual chemical composition is listed in Table 4–2.

Table 4 – 1: Surface EDS analysis results of Ni-P-Tribaloy.

Element	Ni	P	Cr	Mo	Si	Co
Weight %	82.40%	8.88%	3.94%	2.81%	1.42%	0.55%

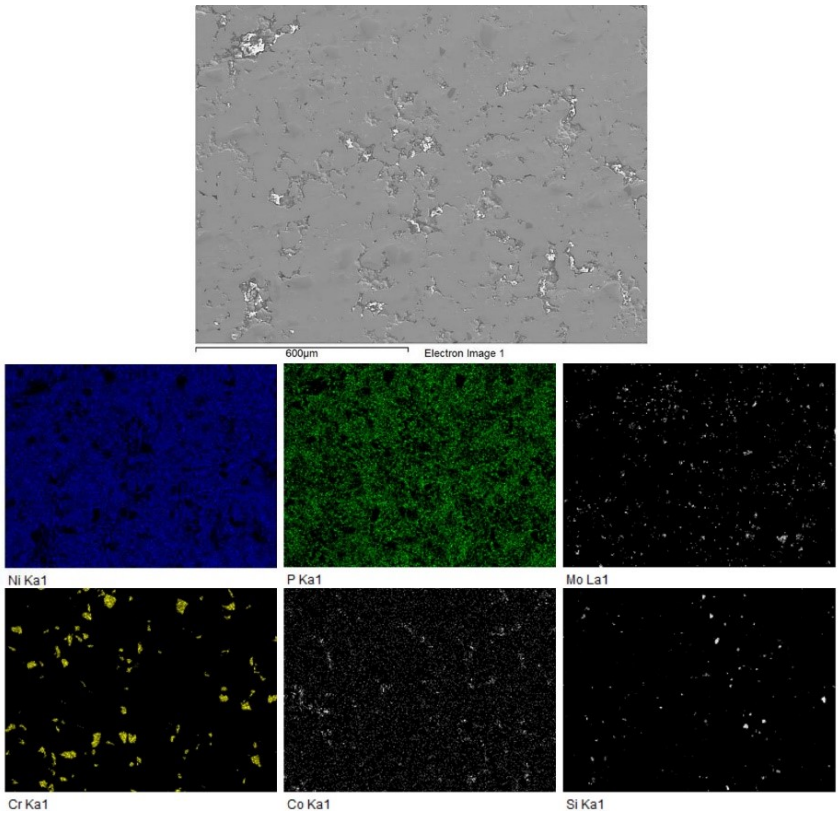

Figure 4 – 5: Surface EDS mapping of Ni-P-Tribaloy.

Table 4 – 2: Composition of Ni-P-Tribaloy.

Element	Ni	P	Co	Cr	Mo	Si
Weight %	74.62%	8.88%	8.33%	3.94%	2.81%	1.42%

Figure 4–6 shows an example of the cross-sectional EDS analysis over a smaller area. It can be seen that the particles that are present in this particular area are distinct from the matrix proving their successful incorporation in the composite coating. This example is representative of the entire coating layer. The substrate–coating interface is clearly defined in Figure 4–6 as represented by the noticeable interface between the Fe and the Ni-P matrix in the elemental map. This EDS map serves as further evidence of the successful deposition of the composite coating.

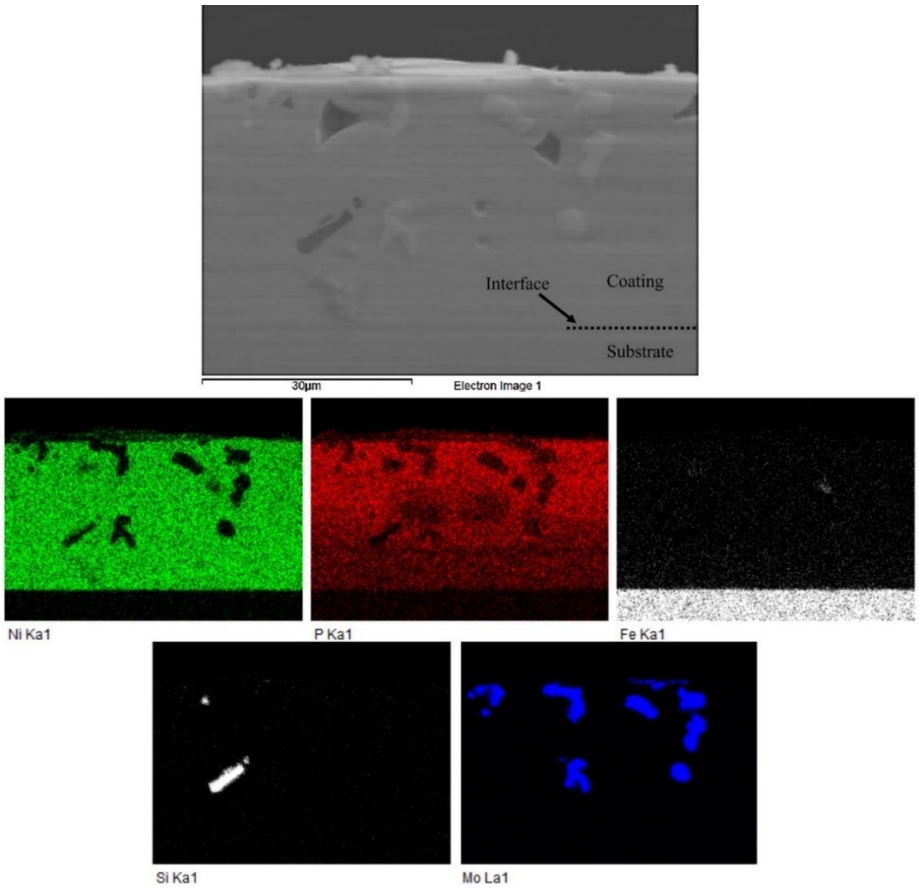

Figure 4 – 6: Cross-sectional EDS mapping of Ni-P-Tribaloy.

Regarding the unpolished composite coating samples that were used in the low-stress abrasion test, the as-deposited coating was also examined. The thickness of the coating varies across the surface ranging from approximately 32 µm to 50 µm, including an 8 µm pre-coating layer for adhesion with the substrate. The variation in thickness is due to the presence of the Tribaloy particles in the coating as the larger particles themselves are being coated with Ni-P, as seen in Figure 4–7. This occurrence has resulted in a rough surface of the composite Ni-P-Tribaloy coatings. The surface roughness value Sa was measured to be 35 µm, considerably higher than the roughness of the polished samples used in the rest of the experiments. SEM images of the surface and cross-section revealing the roughness of the coating surface are provided in Figures 4–8 and 4–9, respectively. More SEM images of the as-deposited coating's cross-section and its EDS mapping are provided in Appendix A.

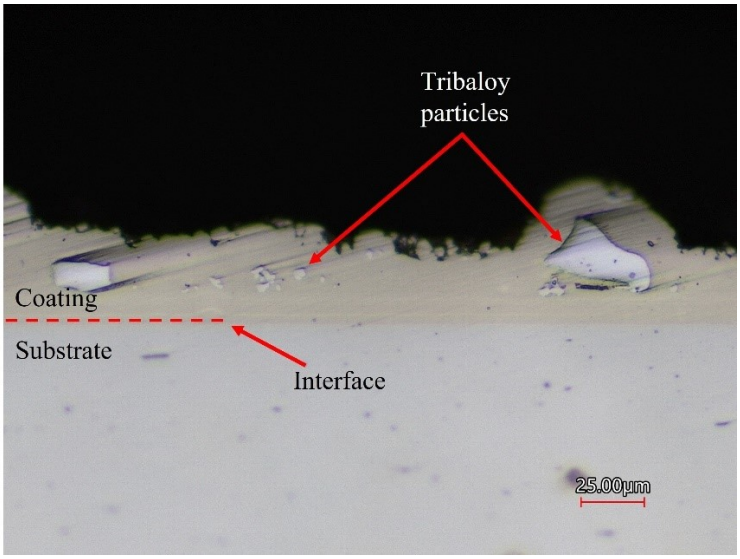

Figure 4 – 7: Cross-section of as-deposited Ni-P-Tribaloy coating.

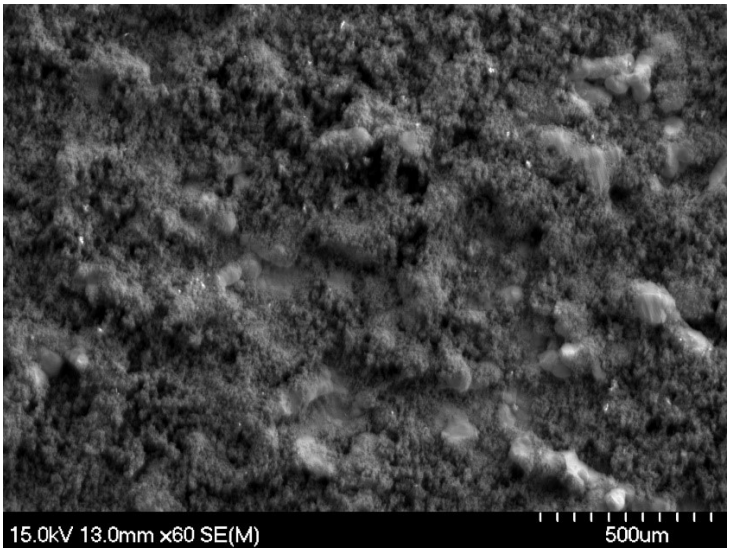

Figure 4 – 8: SEM image of as-deposited Ni-P-Tribaloy surface.

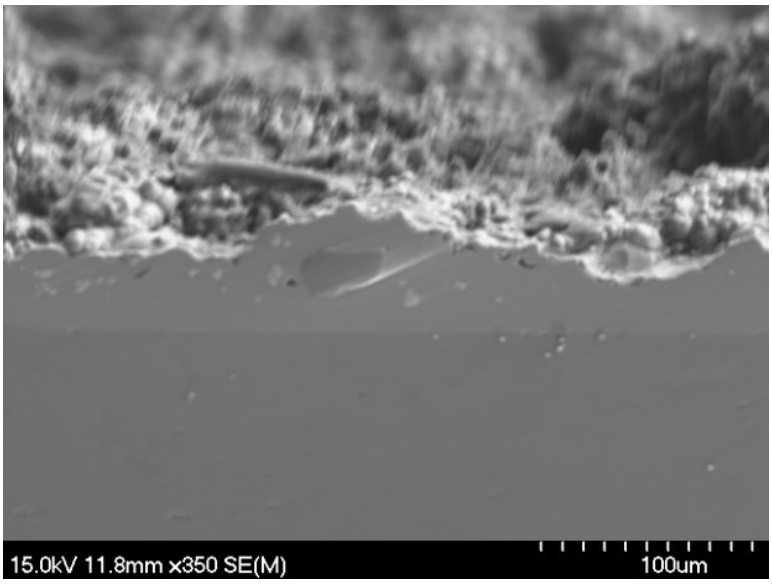

Figure 4 – 9: SEM image of as-deposited Ni-P-Tribaloy cross-section.

4.2 Micro-Hardness

Four micro-hardness measurements were taken on each coating sample. The measurement values for the Ni-P coating are tabulated in Table 4–3 and the Ni-P-Tribaloy coating measurements in Table 4–4, including the hardness, the elastic modulus, and the maximum penetration depth reached by the indenter. The average micro-hardness values are presented graphically in Figure 4–10 with the error bars representing the standard deviation of the measurements. The monolithic Ni-P coating has a Vickers micro-hardness of 5.36 GPa, which falls within the range of the reported values 5–6.5 GPa [132], and an elastic modulus of 125.1 GPa. The composite Ni-P-Tribaloy coating has Vickers micro-hardness of 6.00 GPa and an elastic modulus of 135.9 GPa, exhibiting a 12% increase in hardness over the monolithic coating. The increase in hardness is attributed to the addition of the harder Tribaloy particles to the Ni-P coating. AISI 1018 steel typically has a hardness of 1.7 GPa and elastic modulus of 205 GPa [28], [103]. Both coatings increase the hardness significantly when coated over AISI 1018 steel substrates.

Table 4 – 3: Ni-P micro-hardness measurements.

Hardness (GPa)	Elastic Modulus (GPa)	Maximum Depth (um)
5.041	123.47	7.922
5.357	123.69	7.734
5.468	120.11	7.698
5.556	133.29	7.573

Table 4 – 4: Ni-P-Tribaloy micro-hardness measurements.

Hardness (GPa)	Elastic Modulus (GPa)	Maximum Depth (um)
5.711	118.84	7.589
5.583	136.08	7.533
6.537	141.13	7.070
6.180	147.45	7.195

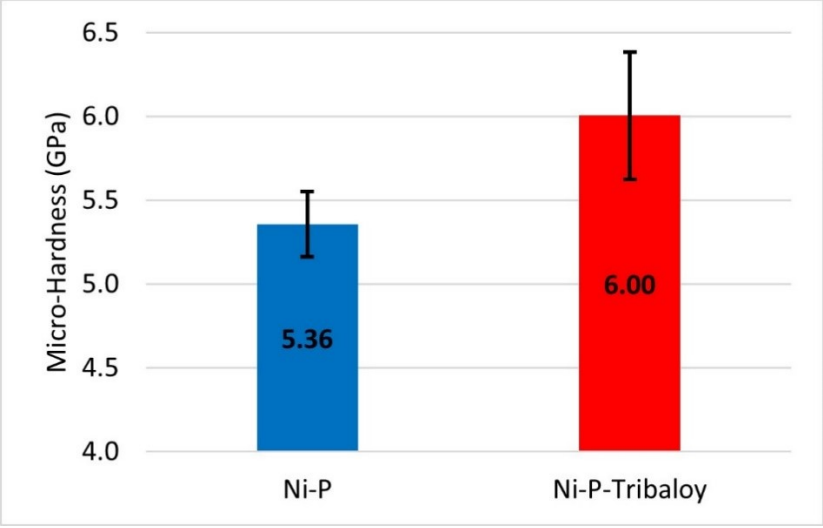

Figure 4 – 10: Micro-hardness of Ni-P and Ni-P-Tribaloy.

On average, the maximum depth reached by the indenter was 7.73 µm in the monolithic coating samples, compared to 7.35 µm in the composite coating samples. The

indenter penetrated deeper in the monolithic coating as expected, due to the higher hardness of the Ni-P-Tribaloy composite coating. Figure 4–11 contains representative examples of the load–depth curves produced for both types of coatings showing the difference in indent depth under a 6N load. For the same maximum load, the Ni-P-Tribaloy coating experienced less penetration depth from the indenter. Those load–depth curves correspond to the second Ni-P measurement datapoint tabulated here and the third Ni-P-Tribaloy. The load–depth curves for the rest of the datapoints are provided in Appendix B.

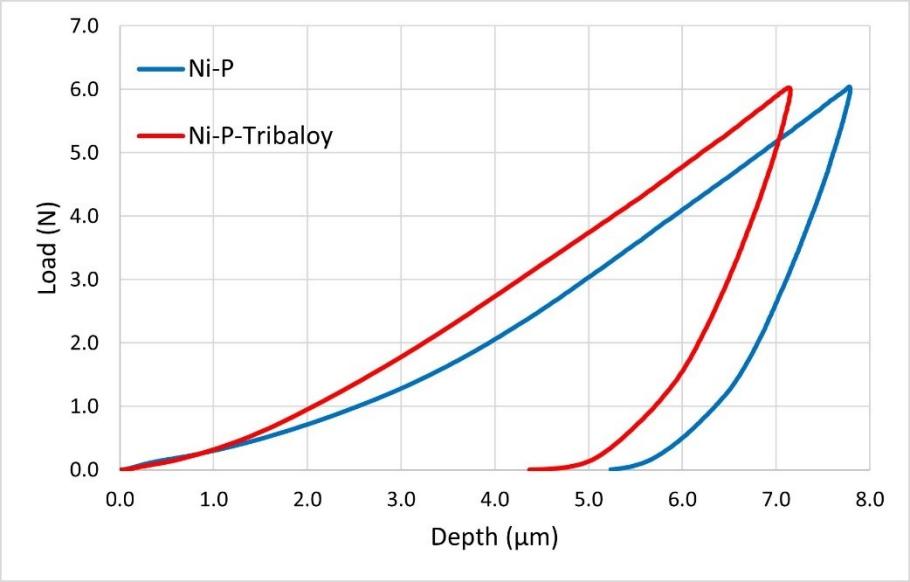

Figure 4 – 11: Load–depth curves of Ni-P and Ni-P-Tribaloy.

4.3 Indentation Behaviour

4.3.1 Load–Depth Curves and Acoustic Emissions

Both the monolithic Ni-P and the composite Ni-P-Tribaloy coated samples were subjected to Hertzian-type indentation at a maximum applied load of 2000 N. The load–depth curves generated from both indents are shown in Figures 4–12 and 4–13, and microscopic images of the indents revealing the cracks that occurred as a result of the indentation are shown in Figures 4–14. Acoustic emissions energy is related to fracture energy and is established as a parameter for investigating crack initiation and propagation [133]. Thus, the acoustic emission signals, during loading and unloading, were also

collected and plotted over their corresponding load–depth curves to support the findings from microscopy. The load–depth curves reveal that the monolithic Ni-P coating had a slightly higher penetration depth of 348 µm, compared to 341 µm for the composite Ni-P-Tribaloy coating.

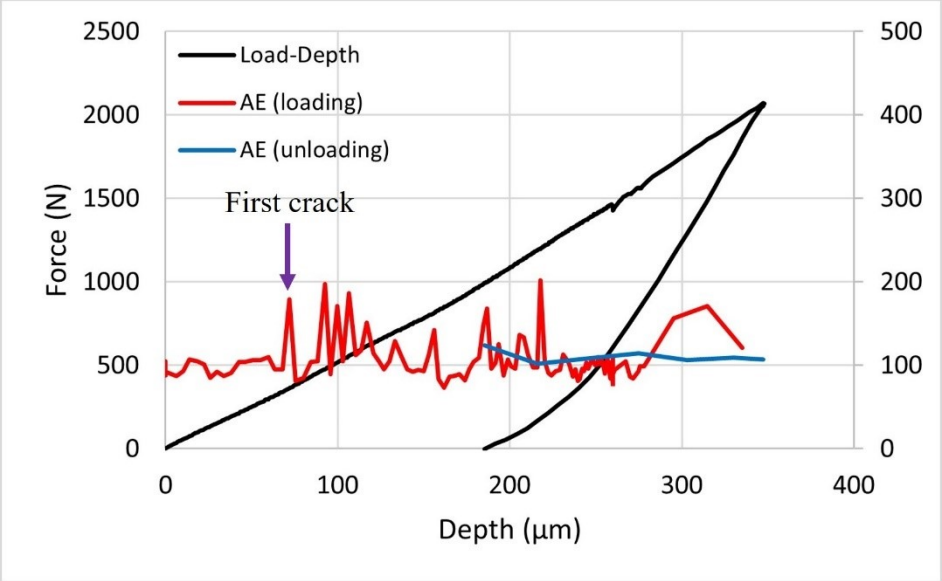

Figure 4 – 12: Ni-P Indentation load–depth curve with AE.

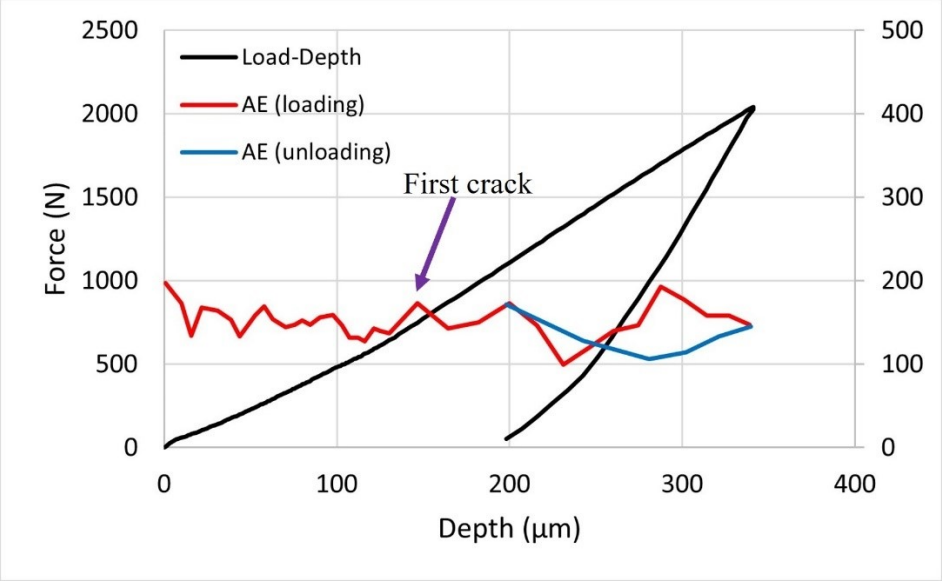

Figure 4 – 13: Ni-P-Tribaloy indentation load–depth curve with AE.

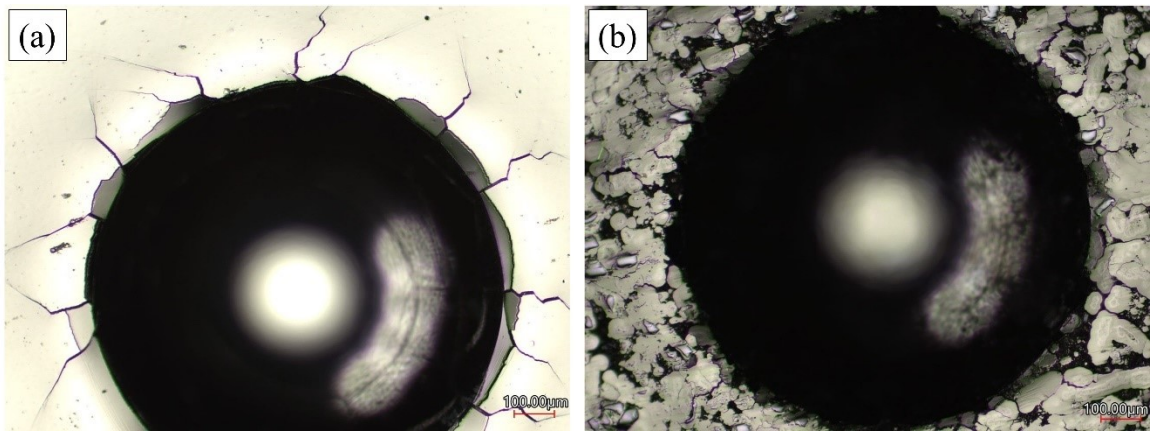

Figure 4 – 14: Confocal microscopy images of indents for (a) Ni-P and (b) Ni-P-Tribaloy.

The area surrounding the indent on the monolithic coating shows evidence of coating delamination and large radial cracks, which are typical for the brittle Ni-P coatings [12], while the composite coating exhibited visibly less cracking and delamination. The reduction in crack size is evidence of toughening [134]. Based on the measured AE signals, the Ni-P coating had significantly higher acoustic activity, including a large initial spike at 361 N. This confirms that it had exhibited a higher severity of cracking events than the composite coating. On the other hand, there are no clear spikes in AE energy observed during the indentation of the Ni-P-Tribaloy coating. Slight changes in the AE signals can be attributed to delamination and/or the formation of small radial cracks [134]. There were no cracks detected during unloading.

The area under the load–depth curve up to the first crack force of the indentation test can be used to determine the toughness of coating [108]. The toughness of the Ni-P coating is calculated to be 13.05 mJ, corresponding to the first major crack that occurs at 361 N. For the Ni-P-Tribaloy coating, it can be assumed that the small peak at 748 N is the first significant crack. This is the highest peak with the highest jump from its previous data point. There are no clear spikes as in the other coating, so this point is assumed to be the most significant crack in this case. Thus, the toughness of the composite coating is estimated to be 51.80 mJ, four times higher than that of the monolithic coating. This is evidence that the addition of Tribaloy particles did in fact increase the fracture toughness of the Ni-P coating.

4.3.2 Cracking Behaviour

Confocal microscopy images of the indentations' cross sections are shown in Figures 4–15 and 4–16 for the monolithic and composite coatings, respectively. Figure 4–15 shows severe ring cracking, typical under Hertzian-type contact [107], just outside the area of contact and inside the indent that extend across the entire layer of the Ni-P coating. Figure 4–16 (a) shows delamination that developed near the edge of the indent on the Ni-P-Tribaloy, where cracks join under the surface causing a piece of the coating to detach. Figure 4–16 (b) shows another example of coating delamination inside the indentation area with no major cracks visible, whereas the monolithic coating had severe cracks at a similar location. The features discussed here are representative of the rest of the indent. More confocal images of the indentations are provided in Appendix C. Cracks observed on the cross section of the composite coating after indentation were shallow cracks, as opposed to the monolithic coating where cracks reached the substrate. The difference in the crack depth between the Ni-P and Ni-P-Tribaloy coatings can be seen clearly in Figure 4–17. It should also be noted that no coating delamination was observed at the substrate–coating interface due to the quality of the coating adherence.

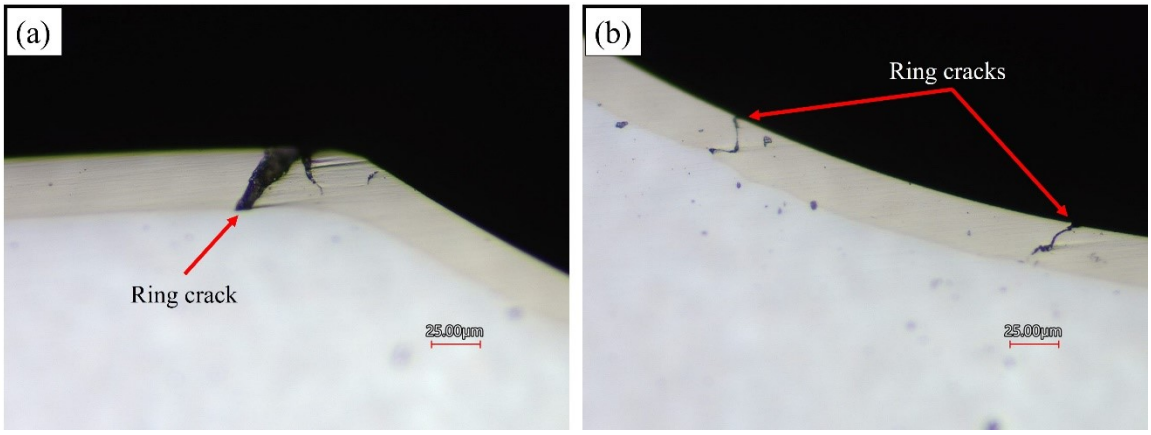

Figure 4 – 15: Select confocal images of indent cross-section for Ni-P.

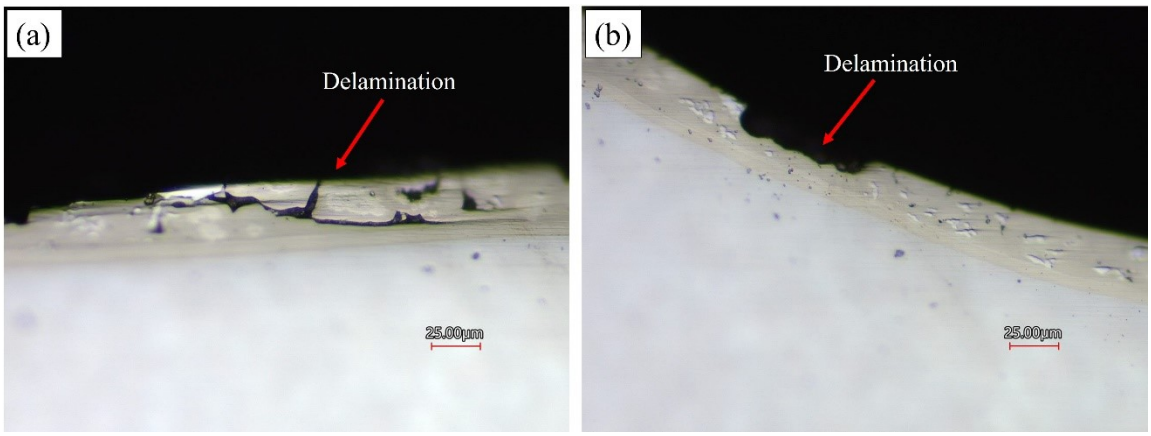

Figure 4 – 16: Select confocal images of indent cross-section for Ni-P-Tribaloy.

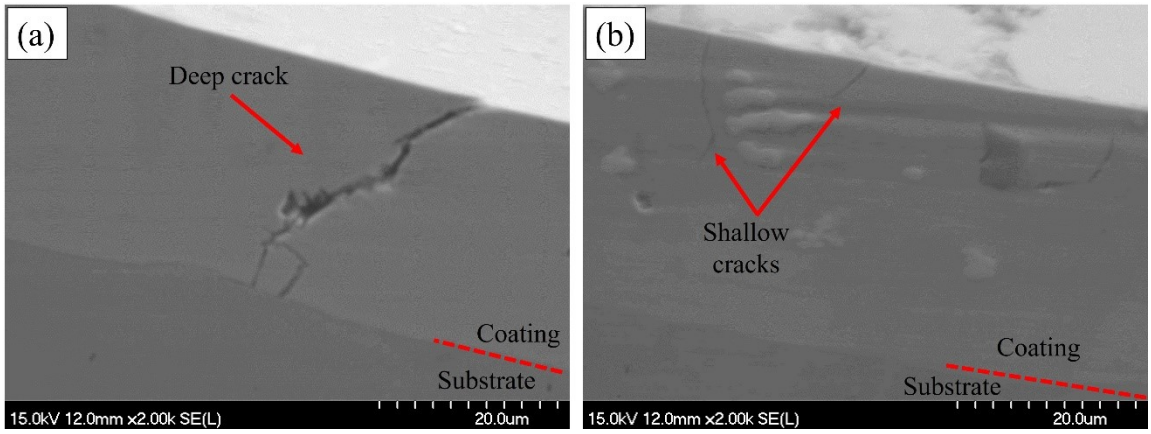

Figure 4 – 17: Crack depth in (a) Ni-P and (b) Ni-P-Tribaloy.

4.3.3 Toughening Mechanisms

Several toughening mechanisms were found to be operating within the Ni-P-Tribaloy coating. First, the dominant crack mode around the indent in the Ni-P coatings were the severe radial cracks seen in Figure 4–18 accompanying delamination and ring cracks. In contrast, the Ni-P-Tribaloy coating appears to have a high density of micro-cracking around the edge of the indent instead of large radial cracks as shown in Figure 4–19, which is supported by the AE data indicating the presence of micro-cracks over major crack. Generally, the presence of cracks is undesirable, however, micro-cracking can reduce the initial crack propagation energy (driving force) for major cracks to grow, leading to improved toughness [134]. Figure 4–19 also shows instances of crack bridging and crack arresting toughening mechanisms. Upon the propagation of major radial cracks, they

encountered several particles that absorbed the energy, eventually leading to limiting the severity of the cracks and in some cases stopping them. For a crack to pass through a reinforcement particle, energy is dissipated, thus reducing the intensity of the crack [111]. The energy driving the cracks propagation is consumed in plastically deforming the Tribaloy particles until the energy is completely depleted, which inhibits further propagation in the material. Appendix C contains more close-up images around the indent on the Ni-P-Tribaloy surface.

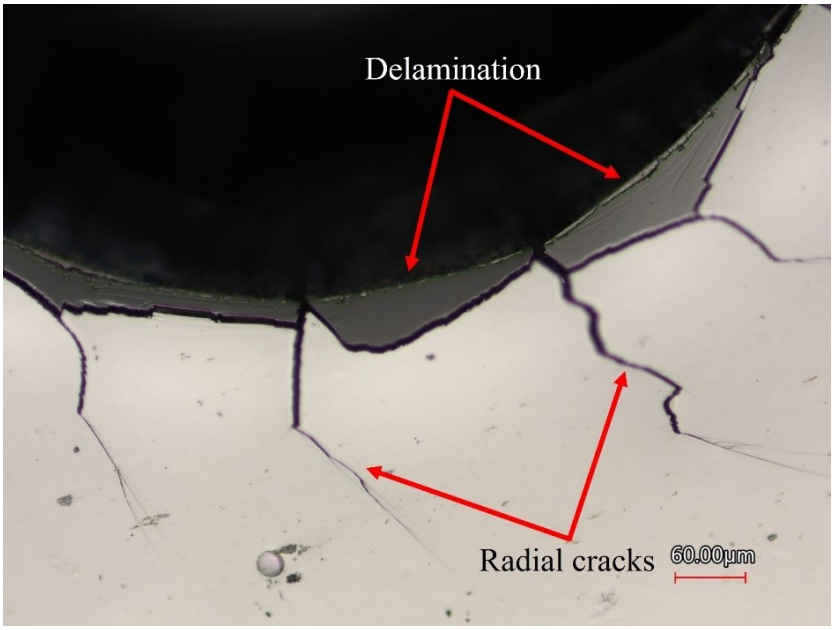

Figure 4 – 18: Ni-P close-up surface indent.

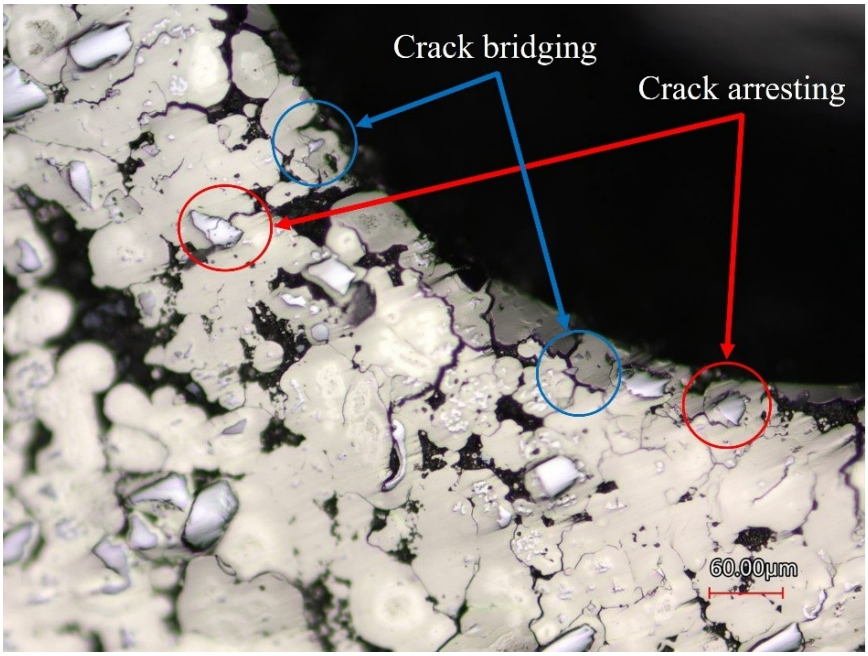

Figure 4 – 19: Toughening mechanisms in Ni-P-Tribaloy.

Further evidence of toughening was found using SEM imaging. Figure 4–20 shows an example of crack deflection on the cross section of the indent as a crack interacts with the second phase particles. When a crack tip approaches a particle, it deflects and deviates to another direction, releasing energy in the process. In this case, deflection occurs without direct contact due to the compressive area forming around the particle impeding the tensile forces associated with crack propagation [135]. The change in crack path requires energy, and dissipating the energy available in turn contributes to toughening. The toughening mechanisms discussed in this section, namely micro-cracking, crack bridging, crack arresting, and crack deflection, have all been proven to enhance the toughness of brittle materials in the literature.

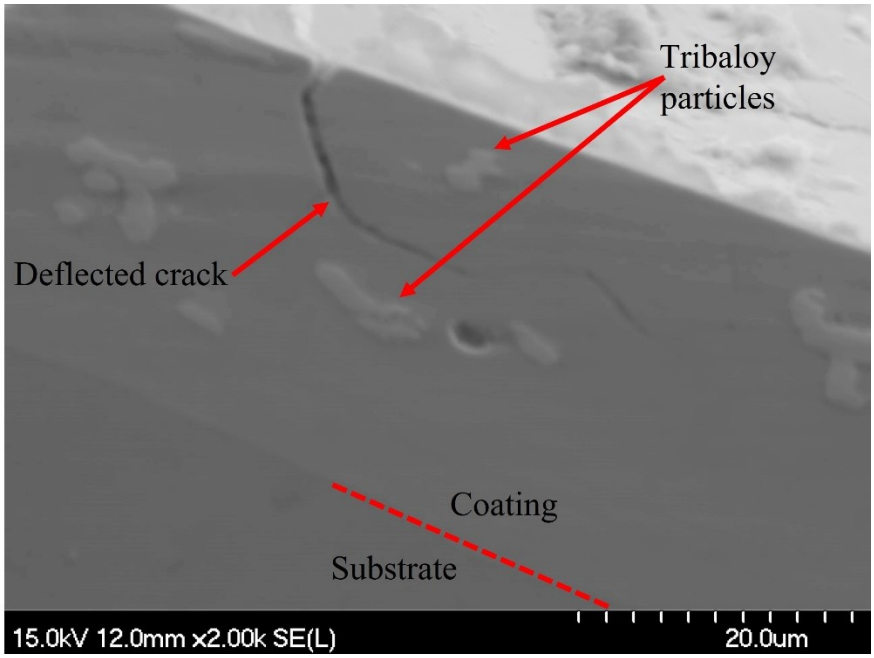

Figure 4 – 20: SEM image of crack deflection in Ni-P-Tribaloy.

Moreover, 3D scans of both indents were generated using Keyence CLSM's topographic scanning to examine the area around the indent on the surface of each coating. Figures 4–21 and 4–22 contain the 3D images of the indent for the Ni-P and Ni-P-Tribaloy coatings, respectively. It is clear that the composite coating exhibits pile-up around the indent just outside the area of contact, while the cracking is very prominent in the monolithic coating with no significant pile-up. This indicates that the Ni-P-Tribaloy is more ductile than the Ni-P coating. The energy that was used for crack initiation and propagation in the monolithic coating was expended in the plastic deformation of the composite coating surface to form the pile-up observed here [136]. The contrast of pile-up and major cracks observed in both 3D images supports the fact that the addition of Tribaloy second phase particles alleviates the brittleness problem of Ni-P.

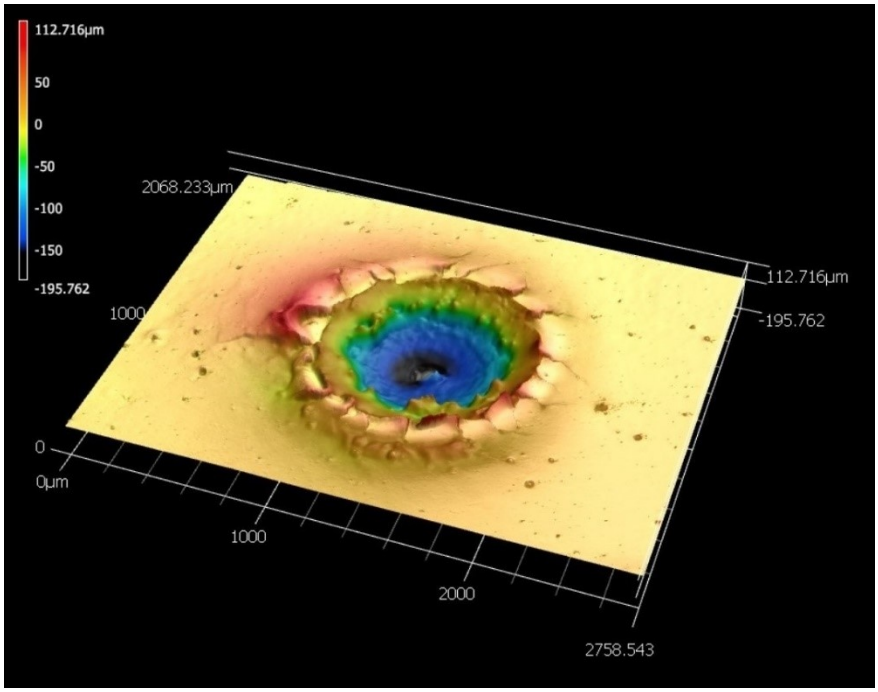

Figure 4 – 21: 3D image of indentation for Ni-P.

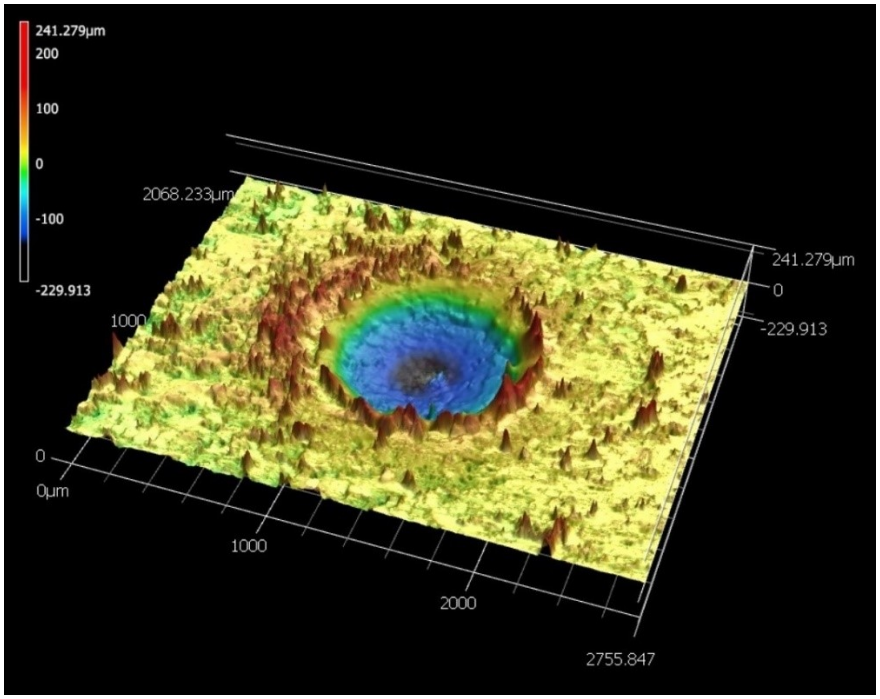

Figure 4 – 22: 3D image of indentation for Ni-P-Tribaloy.

4.4 Scratch Behaviour

4.4.1 Wear Tracks and Acoustic Emissions

Each coating was subjected to five scratches of varying number of passes, all under a constant load of 1kg. The number of passes for the scratches are 1 pass, 25 passes, 50 passes, 75 passes, and 100 passes. The wear tracks can be described as follows: each wear track is 5 mm long with mostly constant width throughout. A higher number of passes represents a greater degree of wear, thus generating wider and deeper tracks. Microscopic images of multi-pass wear tracks from both coatings, showing the main features observed along the wear tracks, are given in Figure 4–23. Visible cracks were observed on the Ni-P coating outside the wear track throughout the length of the scratch, as well as some instances of delamination inside the track. The Ni-P-Tribaloy coating showed material pile-up along the wear track and noticeably more delamination. Ni-P is known to be brittle and susceptible to cracking [137], and the Ni-P-Tribaloy coating appears to exhibit more ductile behavior under the same test conditions. This is representative of the entire wear tracks beyond the portion that is presented here, the same features were observed along the length of the wear tracks and different number of passes. Microscopic images of the full lengths of the 5 scratches on Ni-P and Ni-P-Tribaloy are provided in Appendix D.

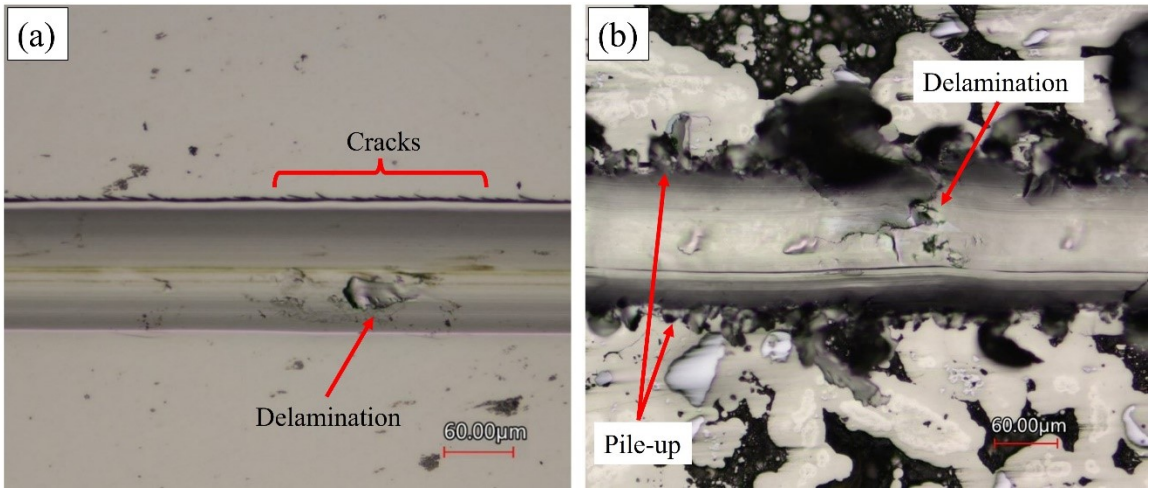

Figure 4 – 23: Examples of scratch wear tracks from (a) Ni-P and (b) Ni-P-Tribaloy.

Acoustic emissions (AE) were measured during scratching to detect signals due to cracking activity. The AE signals, in volts, during a single-pass scratch test are shown in

Figure 4–24. It is clear that the AE signals emitted as the Ni-P coating is scratched have greater intensity and reaching higher levels than that of the Ni-P-Tribaloy coating, which is free of high noise signals. This can be attributed to the formation of cracks [134], and it is supported by the observation of cracks developed along the Ni-P wear track during the scratch test. On the other hand, the low noise signals that are detected in the Ni-P-Tribaloy sample are likely due to both micro-cracking and the surface topography as the indenter is sliding over a particle producing those signals [134]. The low noise signals are expected in composite coatings due to the presence of second phase particles and their effect on the surface, in contrast to the smooth surface of the Ni-P coating. The Ni-P acoustic emissions signals have reached up to 8.9 V in the first scratch pass, while the highest peak reached by Ni-P-Tribaloy is only 1.6 V.

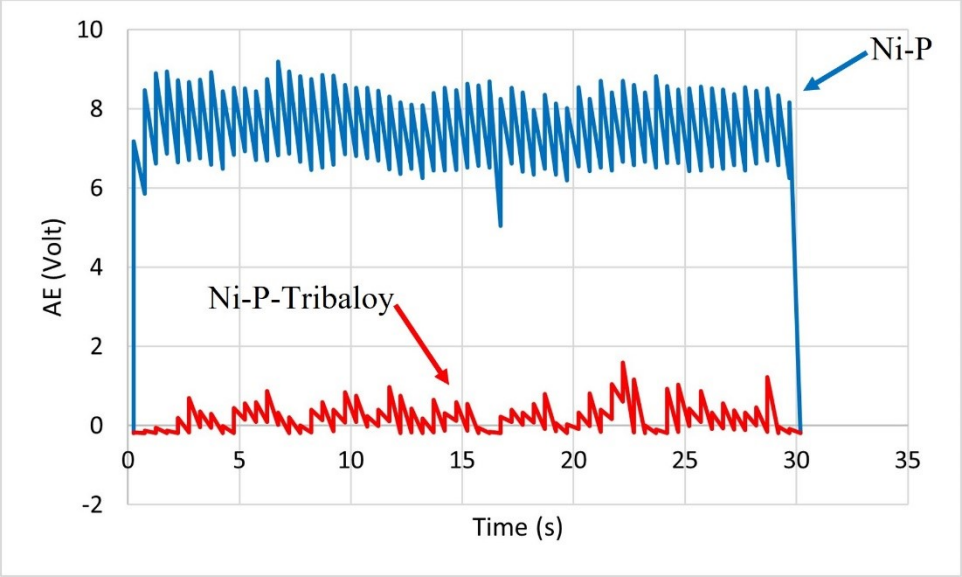

Figure 4 – 24: AE signals of single-pass scratch.

Keyence CLSM's 3D scanning was employed to analyze the wear tracks. Figures 4–25 and 4–26 illustrate the shape of the wear track for both types of coatings as the number of passes progresses, including a 3D image of a portion of the track and the average profile of the whole track for each scratch. Scans of different areas revealed that Ni-P-Tribaloy coatings experiences significant pile-up along the wear tracks, compared to minimal pile-up in the Ni-P coating at the same height magnification. This indicates that the composite coating exhibits higher ductility. The average profile of each scratch was generated by

taking an average of 1000 lines across the scratch at 5 µm intervals, encompassing the entire 5 mm length of each scratch. The extent of material loss from the wear tracks was quantified based on their average profiles. The depth and width of each wear track can also be determined from the average profile. The depths of the scratches were found to be increasing from 2.2 to 4.8 µm, and from 2.9 to 9.3 µm for the Ni-P and Ni-P-Tribaloy, respectively, with an increase in the number of passes. And the widths increased from 56.2 to 81.1 µm and from 84.4 to 127.0 µm, respectively. Greater degree of wear corresponds to deeper and wider wear tracks. The measured values of the widths and depths for both coatings are given in Table 4–5.

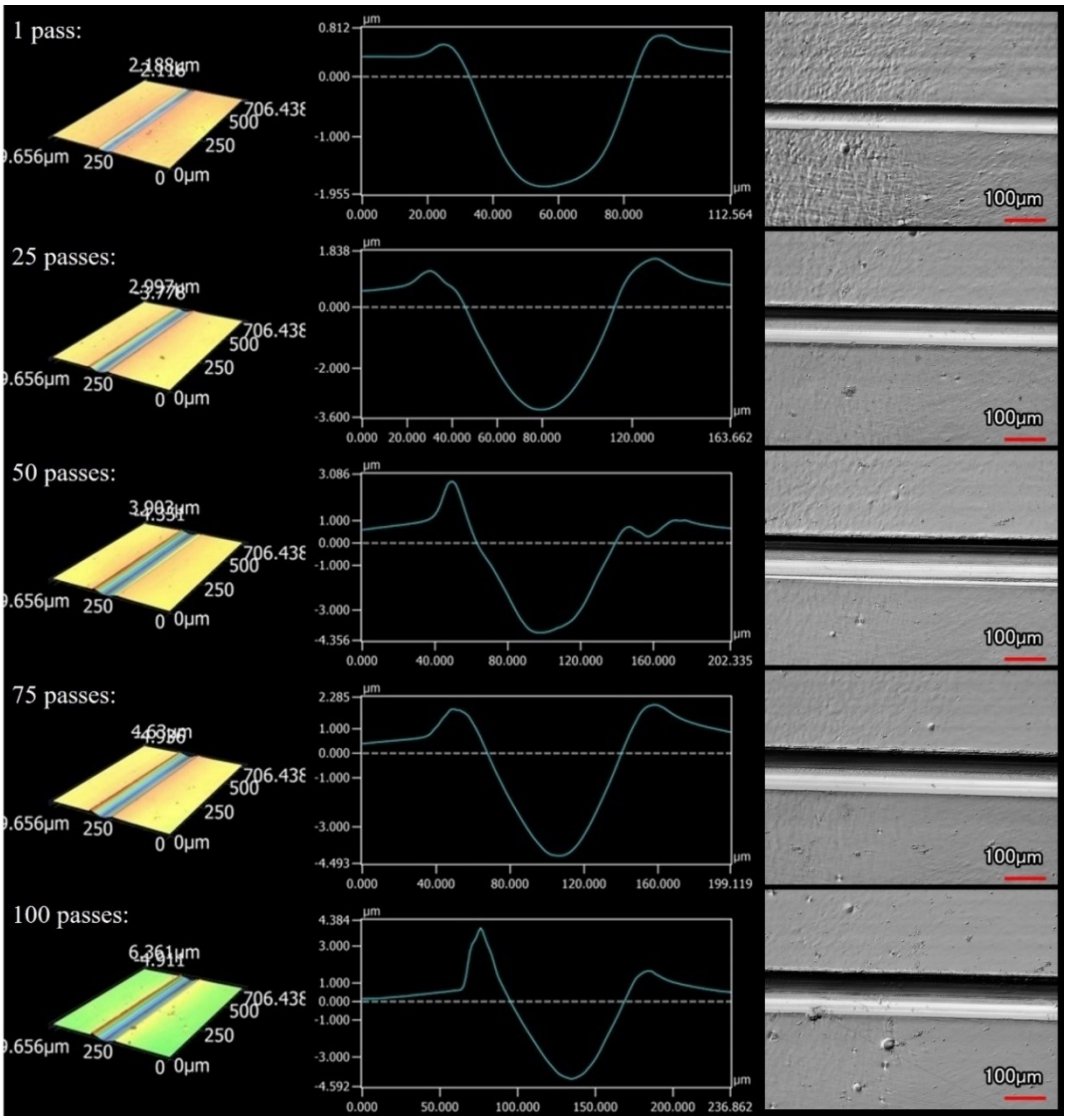

Figure 4 – 25: Shape and average profile of Ni-P scratches.

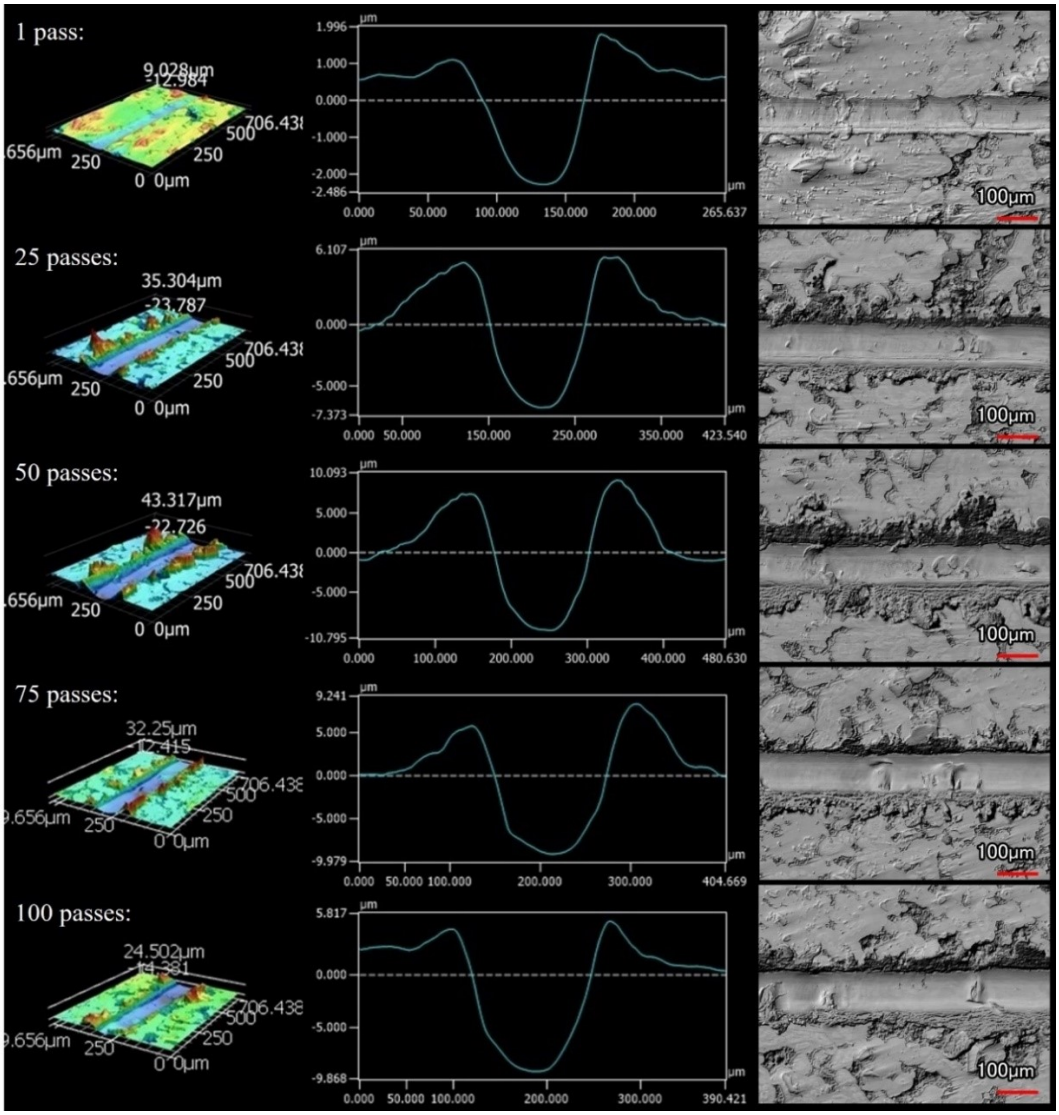

Figure 4 – 26: Shape and average profile of Ni-P-Tribaloy scratches.

Table 4 – 5: Widths and depths of Ni-P and Ni-P-Tribaloy scratch wear tracks.

Coating Type:	Ni-P		Ni-P-Tribaloy	
Number of Passes	Width (µm)	Depth (µm)	Width (µm)	Depth (µm)
1 Pass	56.2	2.16	84.4	2.93
25 Passes	74.7	3.99	109.6	6.67
50 Passes	78.5	4.25	121.3	8.86
75 Passes	79.7	4.75	123.8	9.26
100 Passes	81.1	4.78	127.0	9.29

4.4.2 Volume Loss and Wear Rates

The volume loss, after eliminating the pile-up effect at the edges, is plotted in Figure 4–27 against the sliding distance. The sliding distance is deemed as the number of passes multiplied by the length of one pass and is proportional to the amount of wear that a sample undergoes. As expected, the volume loss increases as wear progresses in both cases. It was found that the composite Ni-P-Tribaloy coating had greater volume loss than the monolithic Ni-P at each sliding distance, under the same test conditions. It should be noted that the wear rate, represented by the slope of the volume loss against scratch distance curve [137], is decreasing as wear progresses. The wear rates were calculated from the slope at a steady state to be 0.69 $\times 10^6$ and 1.88 $\times 10^6$ mm^3/mm, and the total volume loss after 100 passes is 1.18 $\times 10^3$ and 4.35 $\times 10^3$ mm^3 for the monolithic and composite coatings, respectively. The greater volume loss in the Ni-P-Tribaloy coating can be attributed to the Tribaloy particles becoming detached leaving gaps in the coating, and more importantly, getting trapped between the indenter and the surface causing three-body wear, which contributes significantly to the wear rate as the hard particles are wearing out the coating surface. The reduction of the Tribaloy particles size in the Ni-P composite coating is likely to reduce the coating's wear rate as proven in the literature [42].

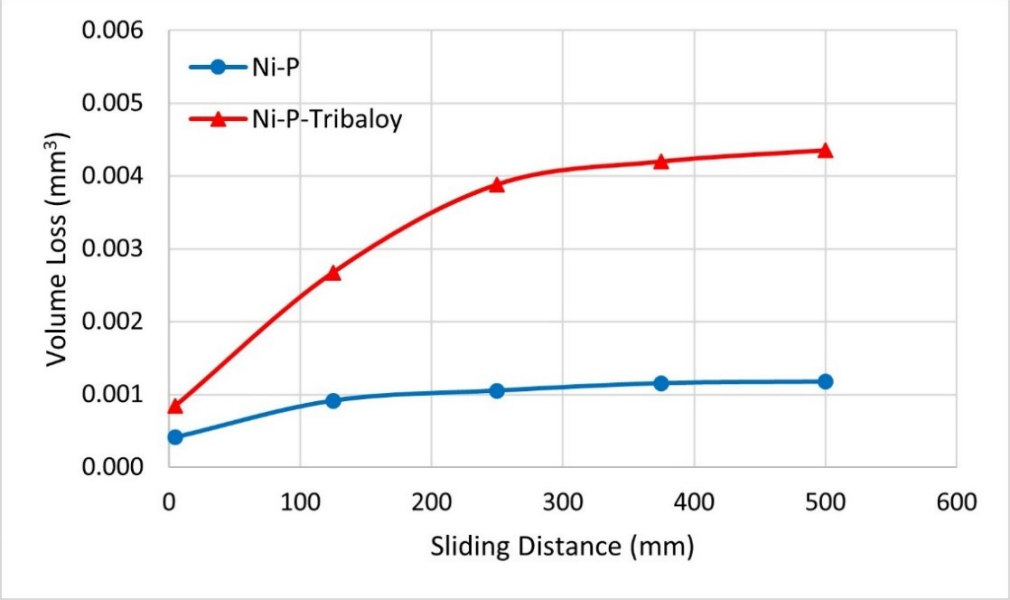

Figure 4 – 27: Volume loss per sliding distance from scratch test.

4.4.3 Wear Mechanisms

While the greater volume loss is unfavorable for the composite coating, it is important to consider the dominant wear mechanisms present in order to evaluate the wear resistance, especially when comparing a brittle material to a more ductile one, as volume loss does not account for fracture which is established to be prominent in the brittle Ni-P coatings [132]. SEM image in Figure 4–28 depicts the wear mechanism present in the Ni-P-Tribaloy after 100 passes. It can be seen that material was removed from the wear track and pushed to the sides of the track due to the plowing effect. Layers of materials were squeezed out successively with every pass by the indenter to accommodate the wear. The build-up of layers of material is pointed out in Figure 4–29 under higher magnification. The dominant wear mechanism for the Ni-P coating is brittle fracture, which does not particularly contribute to the removal of material in the same way, instead, the energy of the scratch indenter is converted to crack initiation and propagation [134]. The abundance of pile-up along the edges of the Ni-P-Tribaloy wear tracks and the dominant wear mechanism being material removal is indicative of improved toughness and ductility.

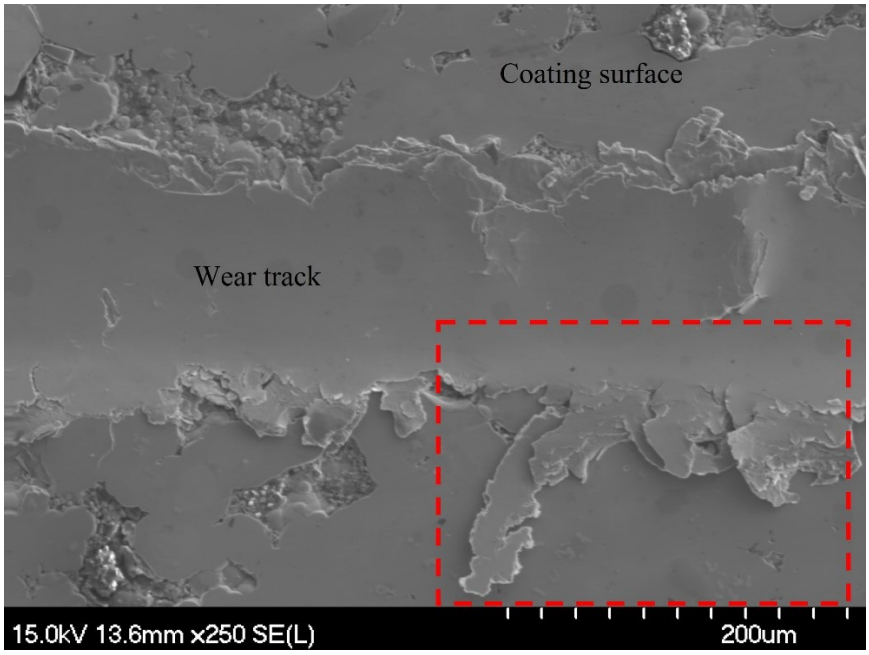

Figure 4 – 28: SEM image of material deformation wear mechanism for Ni-P-Tribaloy after 100 passes.

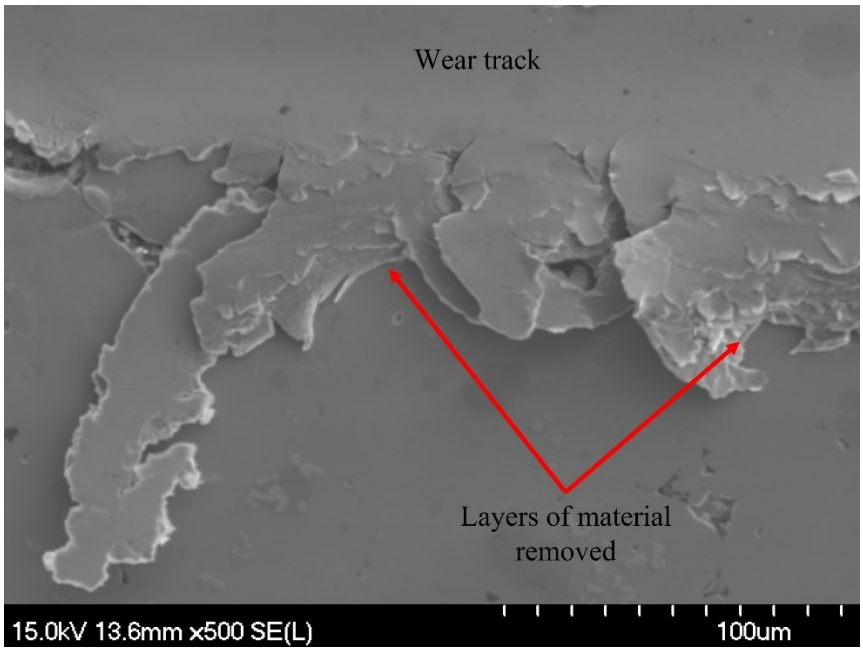

Figure 4 – 29: SEM image closeup of material deformation wear mechanism for Ni-P-Tribaloy after 100 passes.

To illustrate how wear debris forms, Figure 4–30 shows another example of the wear track after 100 passes on the Ni-P-Tribaloy coating surface. It can be seen that material from the wear track is extruded out forming plate-like debris with the repeated sliding. Those plates then fracture and breakaway as debris. Further examination of the wear track by EDS is shown in Figure 4–31 for the 100 passes, which is the highest degree of wear in this research. It is clear from the distribution of the Tribaloy particles that they exist in considerably less amounts inside the wear track after the 100 passes scratch test. This is due to the particles being removed from the track as the surface is scratched repeatedly. Although the particles can be seen on the rest of the surface, they were removed from the track, while the Ni and P elements are present throughout the captured area in the figure.

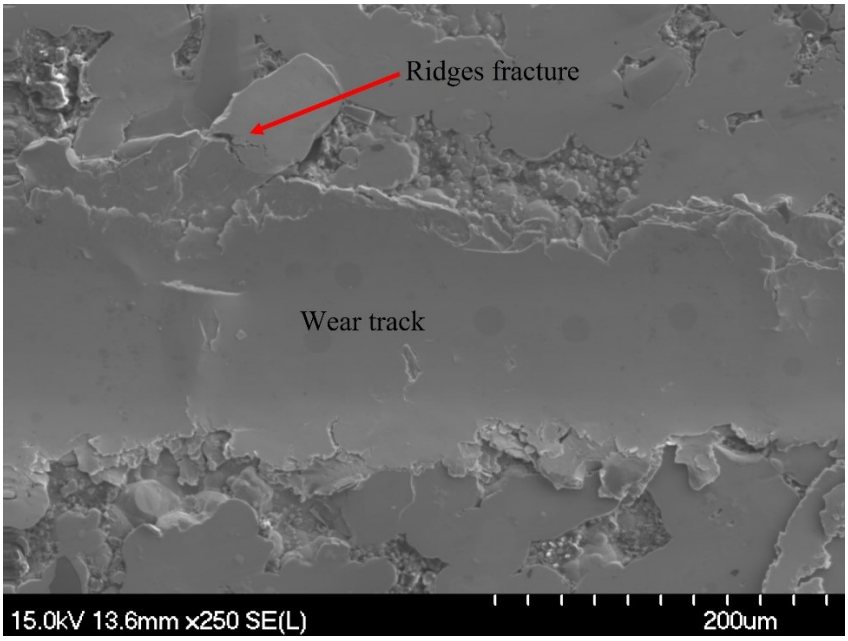

Figure 4 – 30: SEM image of fracture at the wear track ridges for Ni-P-Tribaloy after 100 passes.

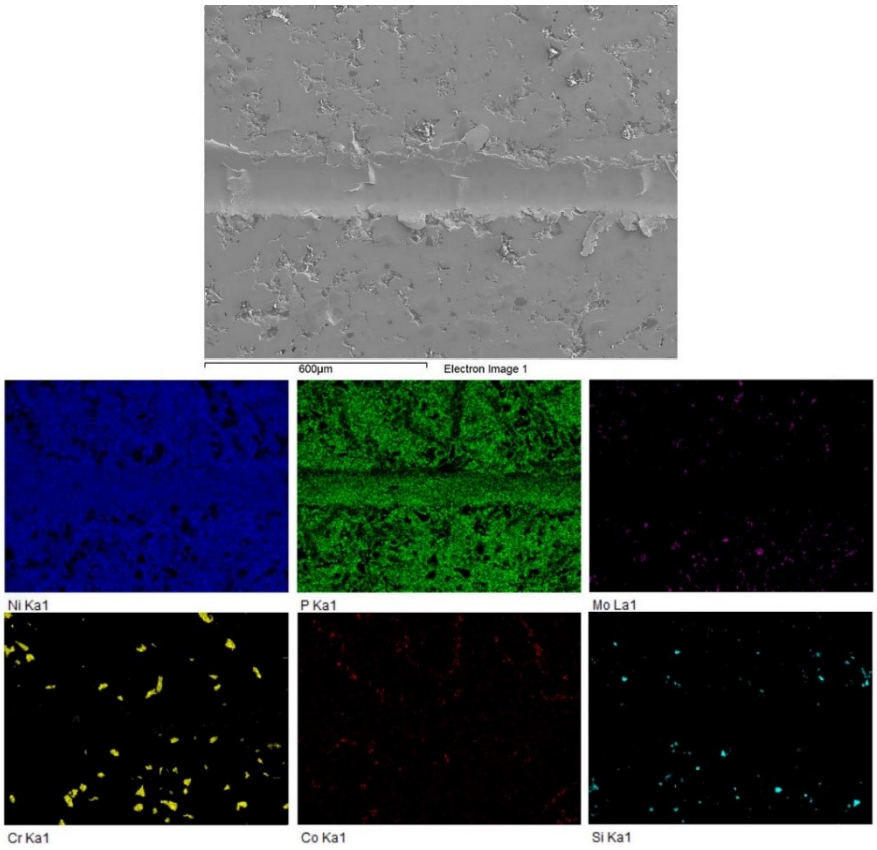

Figure 4 – 31: EDS mapping of scratch wear track for Ni-P-Tribaloy after 100 passes.

4.4.3 Coefficient of Friction

The coefficient of friction was also measured for both coatings during scratch testing. For the Ni-P-Tribaloy coating, the coefficient of friction was found to be 0.20 under a single-pass scratch test. And for the Ni-P coating, the coefficient of friction was found to be 0.11, which is consistent with the reported values in the literature from similar experiments on Ni-P coatings [134], [137]. The higher coefficient of friction value for the Ni-P-Tribaloy is a result of the higher roughness induced by the Tribaloy particles on the surface increasing friction between the indenter and the coating surface, thus affecting the ability of the indenter to slide smoothly. Furthermore, the trend of the coefficient of friction values as the coatings undergo more wear is presented graphically in Figure 4–32. It was observed that the composite coating's coefficient of friction drops initially then plateaus as wear progresses. The reduction in friction is attributed to the removal of the roughness-inducing particles in the later stages, as well as the increase in the indenter contact area with each pass. The monolithic coating exhibits a slight drop then plateaus.

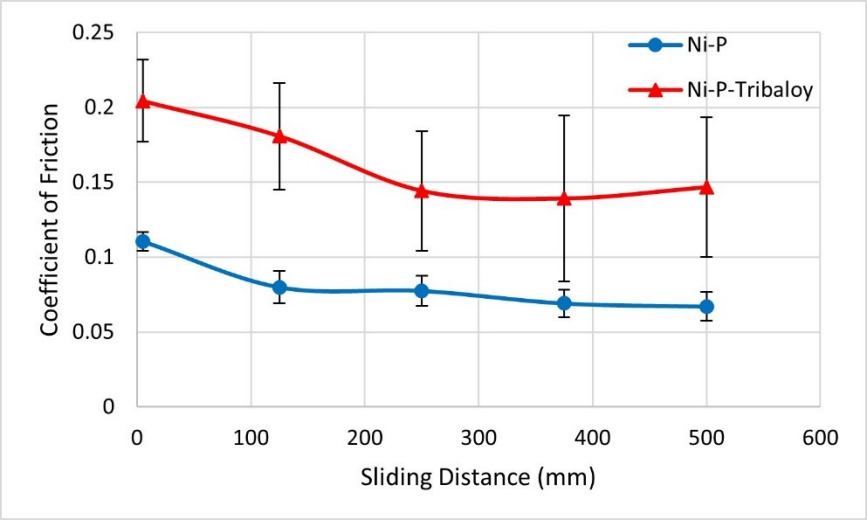

Figure 4 – 32: Coefficient of Friction as a function of sliding distance.

4.5 Low-Stress Abrasion

4.5.1 Abrasion Wear Scar

Low-stress abrasion tests were performed on Ni-P-Tribaloy coating samples, as well as Ni-P coatings samples, until the steel substrates were first exposed and detected by visual inspection after each step. The resulting wear scars on both coatings are shown in Figure 4–33. The wear scars are rectangular in shape, fitting the description of an even and uniform scar as described in the ASTM G65 standard [124]. This confirms the proper alignment of the apparatus setup and the accuracy of the test. The dimensions of the wear scars are roughly 25.4 mm long and 12.7 mm wide. Microscopic image of the wear scars are provided in Appendix E.

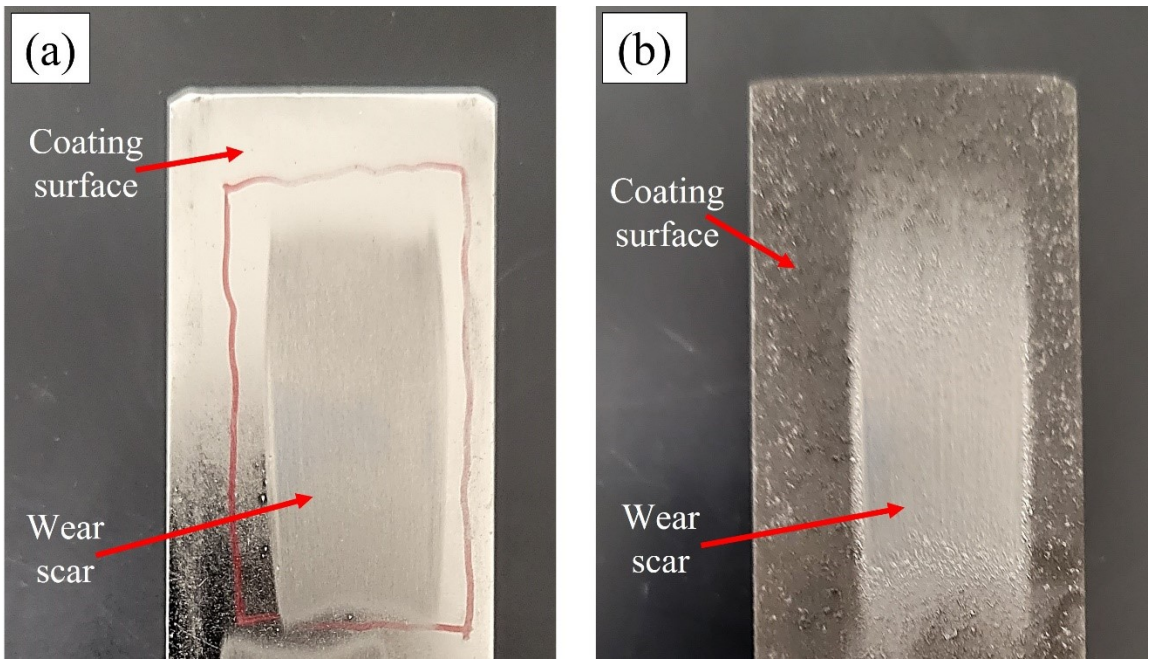

Figure 4 – 33: Pictures of wear scars on (a) Ni-P and (b) Ni-P-Tribaloy coating samples.

Keyence CLSM's 3D topographic scanning was utilized to analyze the wear scars. For each wear scar, a 3D scan was produced and the average profile across the scar width was generated by taking an average of 1500 horizontal lines across the middle at 5.3 μm intervals, covering 7.95 mm of the middle of each scar. The 3D scans of the scars are given in Figure 4–34 and the average profiles across the scars are in Figures 4–35 and 4–36 for the Ni-P and Ni-P-Tribaloy samples, respectively. It should be noted that the scar profile

of the Ni-P coating is smoother as expected due to the roughness of the Ni-P-Tribaloy coating surface prior to the abrasion leading to a rougher wear scar.

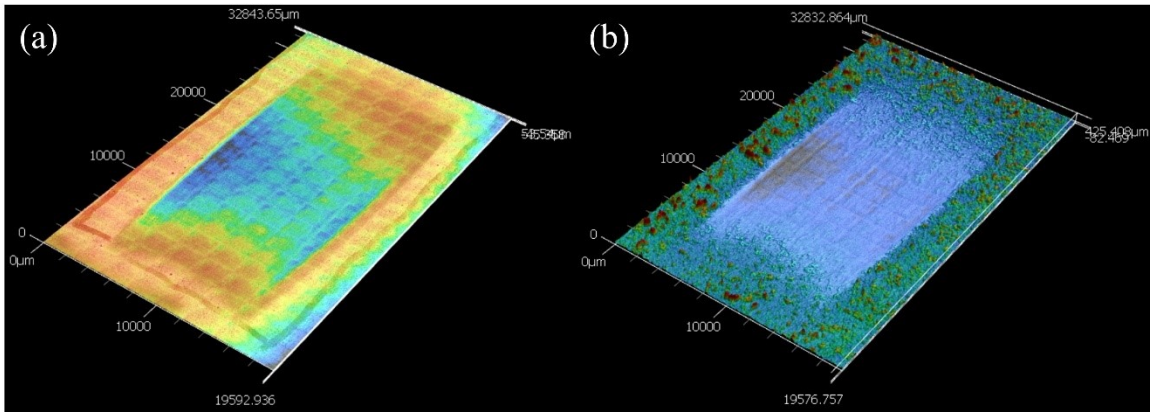

Figure 4 – 34: 3D images of the wear scars for (a) Ni-P and (b) Ni-P-Tribaloy.

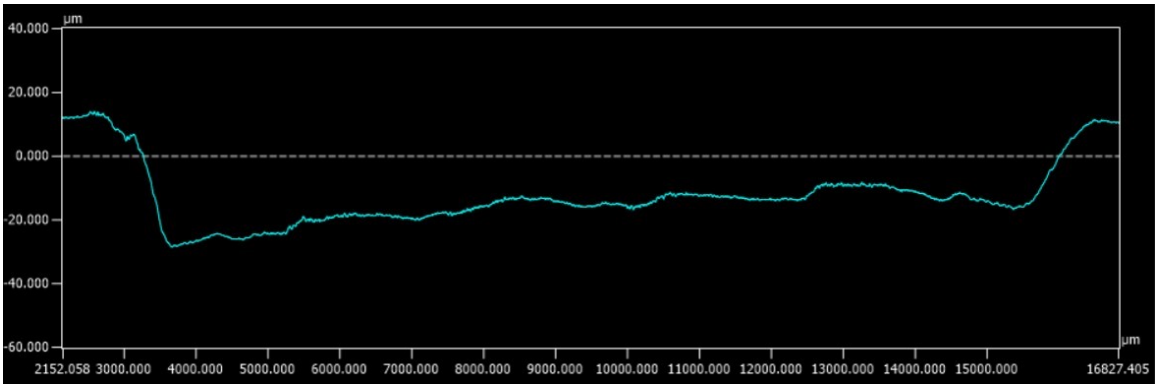

Figure 4 – 35: Average profile across the Ni-P wear scar.

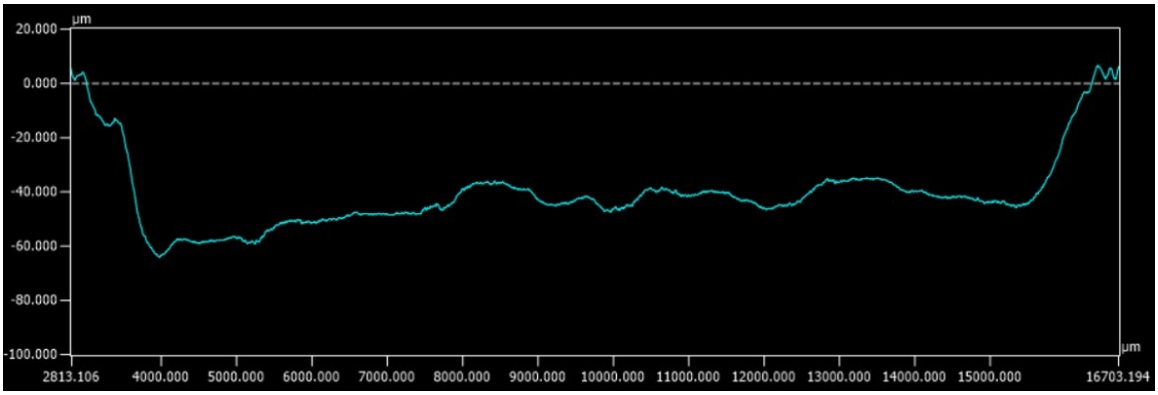

Figure 4 – 36: Average profile across the Ni-P-Tribaloy wear scar.

4.5.2 Abrasion Rate

All specimens were weighed at the start of the abrasion test and continuously after each 10-revolution step to track the material loss due to abrasion. The tests results were expressed as volume loss in mm^3 in accordance with the ASTM G65 standard [124] to allow for comparison with other materials. The cumulative abrasion volume loss is plotted in Figure 4–37 against the number of wheel revolutions for the Ni-P-Tribaloy and Ni-P coatings. The test was replicated on a separate sample for each material to ensure the repeatability of the results, and the average values were plotted with the standard deviation represented by error bars. The measurements for the Ni-P samples were extremely close in value, therefore, their error bars are too small to appear on the Ni-P curve.

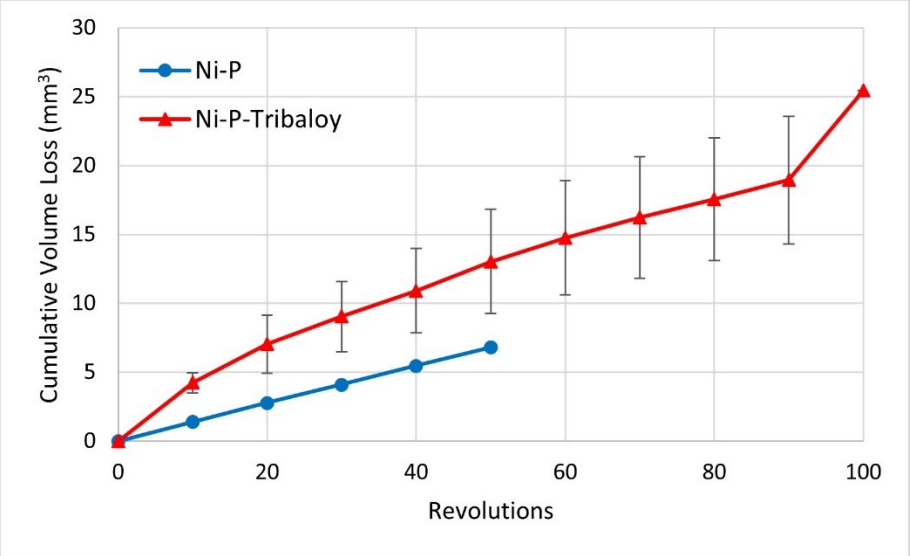

Figure 4 – 37: Volume loss per wheel revolution from abrasion test.

One Ni-P-Tribaloy specimen was deemed to fail after 100 revolutions upon visual inspection and noticing the initial exposure of the steel. The second sample failed after 90 revolutions. On the other hand, both Ni-P specimens failed after only 50 revolutions. The number of revolutions is proportional to the amount of wear that a sample undergoes. As expected, the volume loss in each case increases as wear progresses, which follows the general model of abrasion [138]. It was found that the composite Ni-P-Tribaloy coating had greater volume loss than the monolithic Ni-P at any given point, under the same test conditions. After 50 revolutions where the Ni-P coatings failed, the total volume loss of the

Ni-P-Tribaloy and the Ni-P coatings were 13.0 and 6.80 mm^3, respectively. The greater volume loss in the Ni-P-Tribaloy coating can be attributed to the Tribaloy particles becoming detached as the surrounding coating matrix is worn away, leaving gaps in the coating, and more importantly, getting trapped between the rubber wheel and the test surface, adding to the three-body wear effect, which contributes significantly to the wear rate as the hard particles are further wearing out the coating surface [139]. Studies have shown that the size of abrasive particles relative to the reinforcing particles in a metal matrix composite has an influence on wear, such that particle pull-out or plough-off becomes prominent during ASTM G65 testing when the abrasive particles are larger than the reinforcing particles, which is the case in this research (sections 3.1.2, 3.7), as opposed to wear being primarily caused by the loss of matrix when the abrasive particles are small [140], [141].

It is important to note that the Ni-P-Tribaloy coating specimens lasted longer in this test despite more material loss due to the discrepancy in the initial thicknesses. The Ni-P coatings tested in this study had a thickness of 33 μm, which is thinner than that of the composite coating discussed in section 4.1. The Ni-P-Tribaloy wear scar was deeper and it was subject to more abrasion.

The abrasion wear rate was taken as the slope of the linear portion of the volume loss curve in mm^3 per revolution. It can be seen that the wear rate decreases as wear progresses for the Ni-P-Tribaloy coating, while the wear rate of Ni-P remained constant throughout the experiment. The wear rate of the Ni-P-Tribaloy coating was found to be 0.170 mm^3 per revolution. In comparison, the Ni-P coating had a lower wear rate of 0.135 mm^3 per revolution. This can be attributed to the considerably higher roughness of the composite coating, as reported in several studies correlating higher wear rates to higher surface roughness [142]–[144].

4.5.3 Wear Scar Analysis

Upon the examination of the wear scar on the Ni-P-Tribaloy coating surface using SEM, the first feature observed at low magnification is the flattening of the coating surface. The rough coating surface prior to the test is due to some of the Tribaloy particles on the surface being coated over by the Ni-P around them, as discussed in section 4.1, resulting

in a high roughness by creating the asperities on the surface seen in Figure 4–7 and Figure 4–8. The SEM images in Figure 4–38 illustrate the flattening that occurs at the edge of the abrasion wear scar, indicating their location on the scar. The insert images in the upper right corners are where the larger images were taken relative to the wear scar. It can be seen in Figure 4–38 (b) that the surface at the edge of the wear scar is relatively smoother compared to the coating surface in Figure 4–8 using the same image scale, as the roughness is being flattened (rather than polished) caused by the sliding. As the specimen is inspected further towards the middle of the scar, in Figure 4–38 (a), it was found that the surface is even smoother as the asperities are being further flattened and pressed in. This is due to the nature of the contact between the rubber wheel and test specimen and their respective orientations as illustrated by the diagram in Figure 4–39 showing the contact area between the wheel and the specimen. There is less/shallower contact between the two at edge of the wear scar and it is undergoing less abrasion, whereas inside the scar there is deeper contact, thus more flattening of the material.

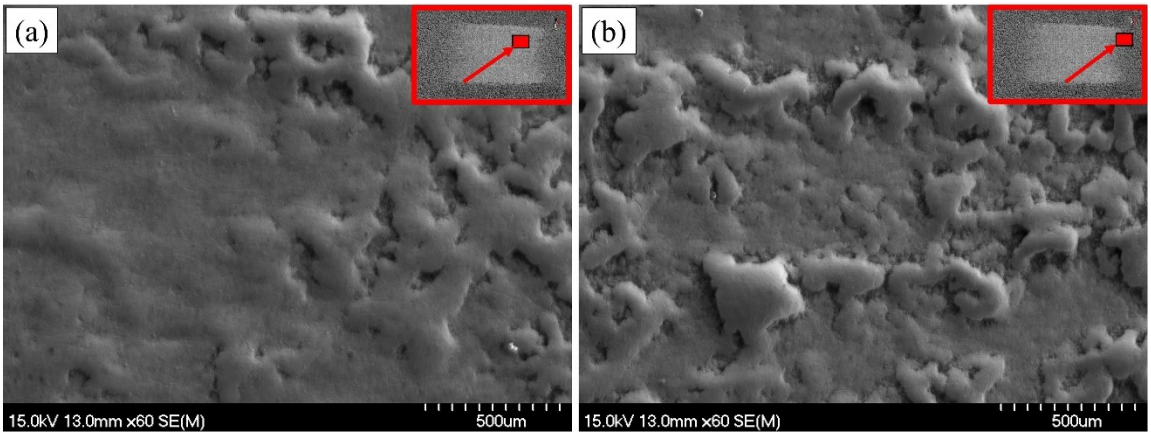

Figure 4 – 38: Ni-P-Tribaloy surface depicting the flattening (a) inside and (b) at the edge of the abrasion scar.

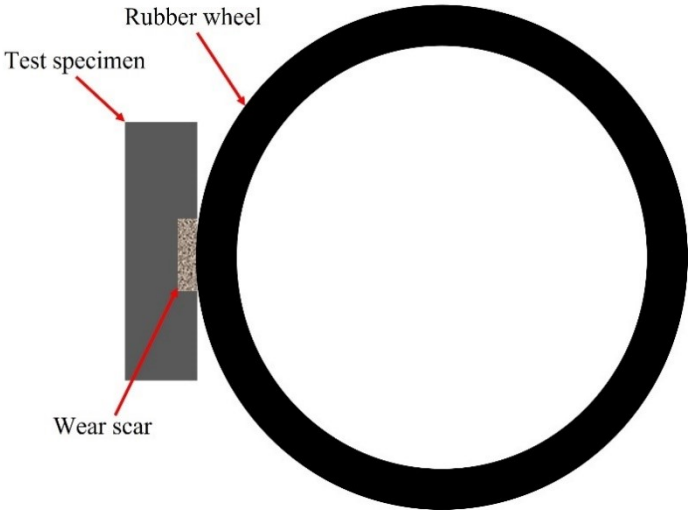

Figure 4 – 39: Illustrative diagram of the contact area between the wheel and specimen.

This effect can also be seen from the average profile along the length of the wear scar. Figures 4–40 and 4–41 show the average profiles for Ni-P and Ni-P-Tribaloy obtained from the 3D scans by taking an average of 500 vertical lines at 5.3 μm intervals along the length of the scar. It is clear that the profiles of both coatings are curved with the middle of the scars being deeper than the edges. The further away from the edge, the deeper that contact with the rubber wheel.

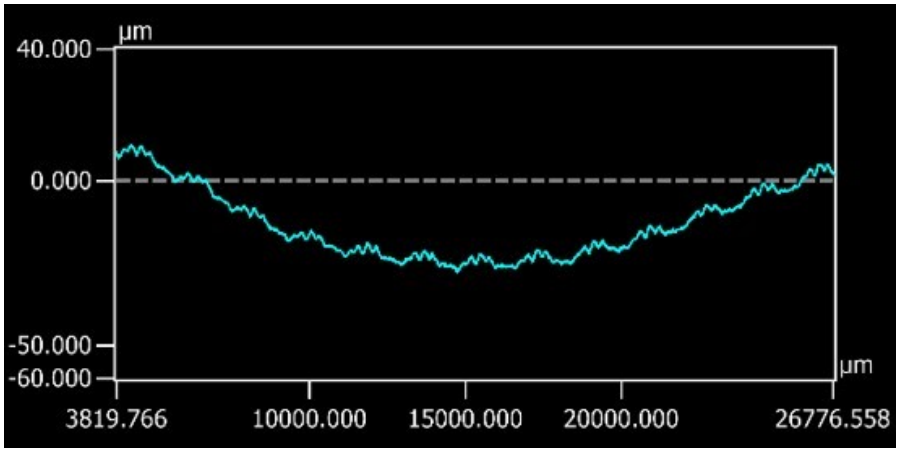

Figure 4 – 40: Average profile along the Ni-P wear scar.

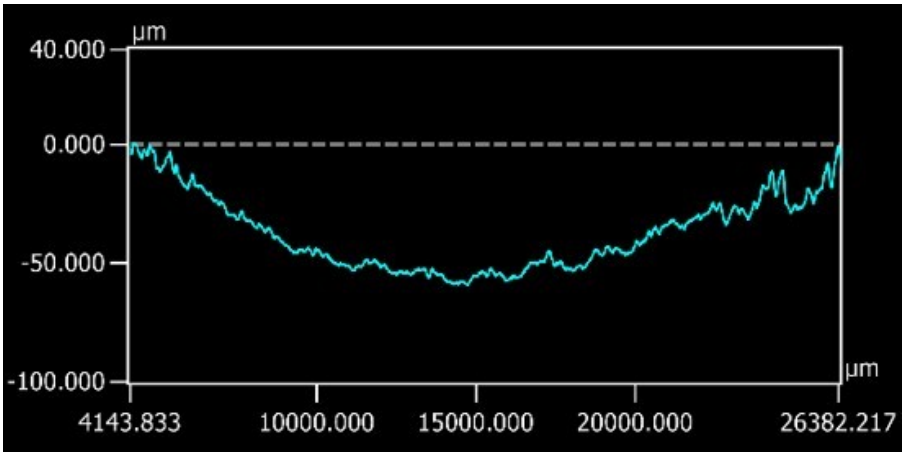

Figure 4 – 41: Average profile along the Ni-P-Tribaloy wear scar.

Figure 4–42 shows representative images of the abrasion from inside the wear scar. It was found that plowing is the dominant wear mechanism in the abrasion of this Ni-P-Tribaloy coating. Material is being squeezed out and pushed to the sides to form ridges, which is typical of the plowing mechanism. The coating is being deformed by plastic deformation as the abrasive is extruding the surface and sliding over it. Large and semi-angular abrasive particles slide on the surface and cause wide and shallow grooves as seen here, as opposed to deeper grooves and cutting mechanism that would occur in the case of sharp abrasive particles with sharp corners resulting in more damage. An instance of a deep groove, likely due to a sharp corner on an abrasive particle is shown in Figure 4–43. Although some deep grooves that are indicative of a cutting mechanism were found, they are not significant, and they cannot be considered the dominant mechanism. It should be noted that the ridges formed are not sliding in one direction, particles are being pushed against the surface and they slide in different directions, and the grooves intersect as seen in Figure 4–42 (a). The hardness of the Ni-P-Tribaloy coating also contributes to its wear resistance as studies have shown that the penetration depth on the worn surface by the abrasive particles is proportional to the ratio of hardness to applied force [145], [146].

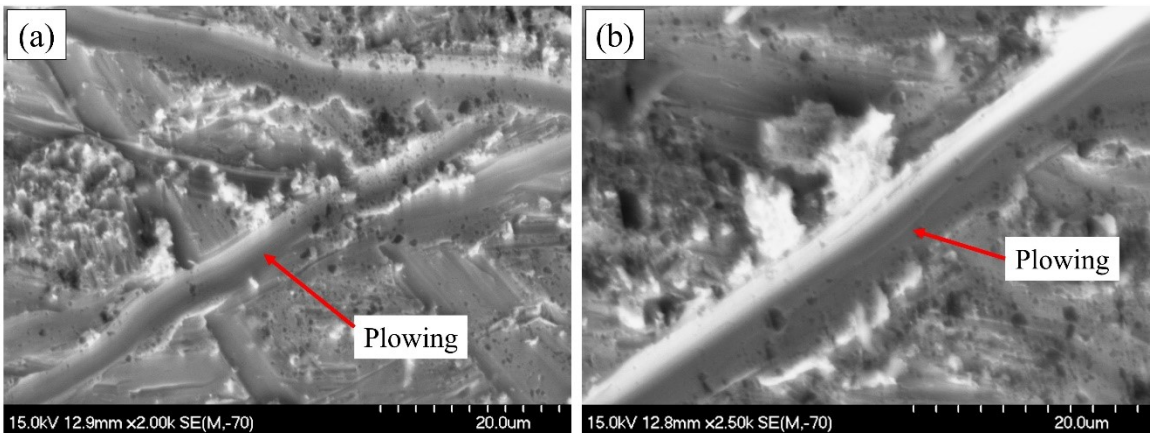

Figure 4 – 42: SEM images of plowing in Ni-P-Tribaloy.

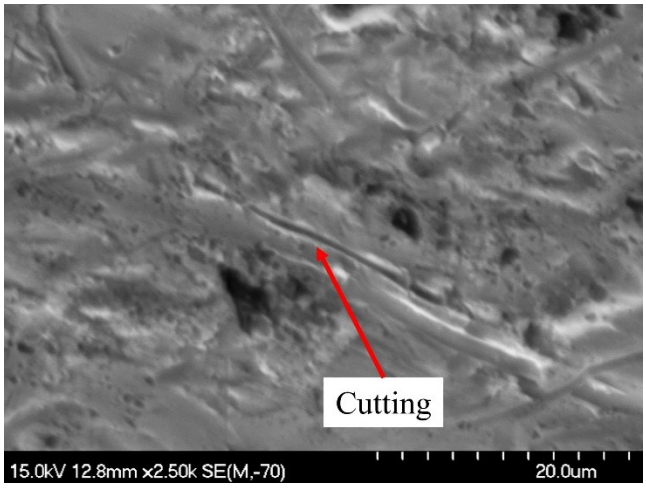

Figure 4 – 43: SEM image of a cutting in Ni-P-Tribaloy.

Furthermore, there is also compaction that occurs, along with plowing, arising from the applied load and the contact between the rough surface and the rubber, where the material is pressed in by that contact. Areas where the rough surface is being pressed in can be seen in the SEM image provided in Figure 4–44. While in the Ni-P samples in Figure 4–45, mainly plowing is present. The compaction in the Ni-P-Tribaloy abrasion can be attributed to the hardness of the Tribaloy particles. They cannot be easily removed from the coating by plowing, the coating is plowed over them and they are compressed in. This is also evident in Figure 4–46, showing the cross-section, where the Tribaloy particles are protruding from the Ni-P matrix while the material around them is removed by plowing, and subsequently the particles are removed.

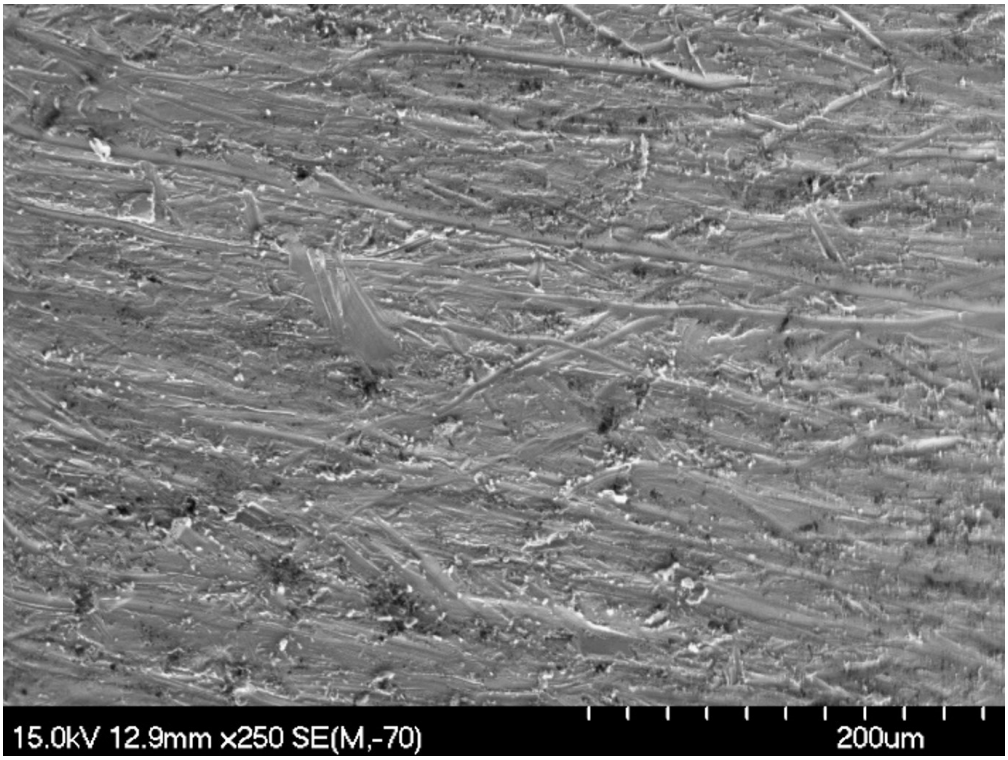

Figure 4 – 44: SEM image of Ni-P-Tribaloy abrasion wear scar.

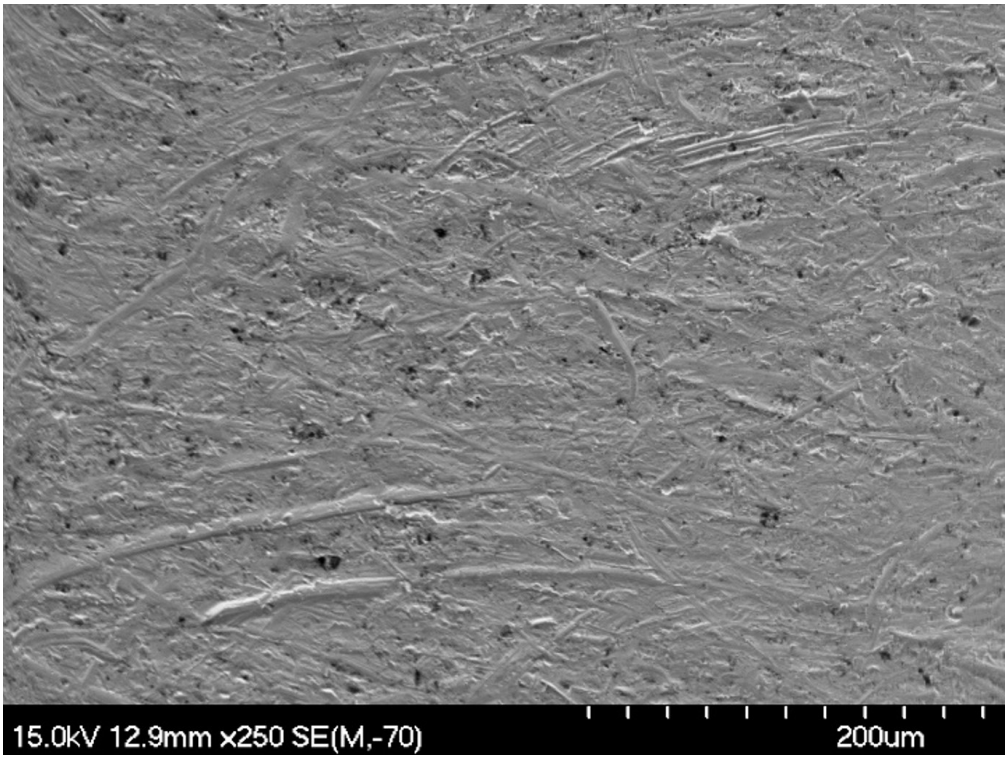

Figure 4 – 45: SEM image of Ni-P abrasion wear scar.

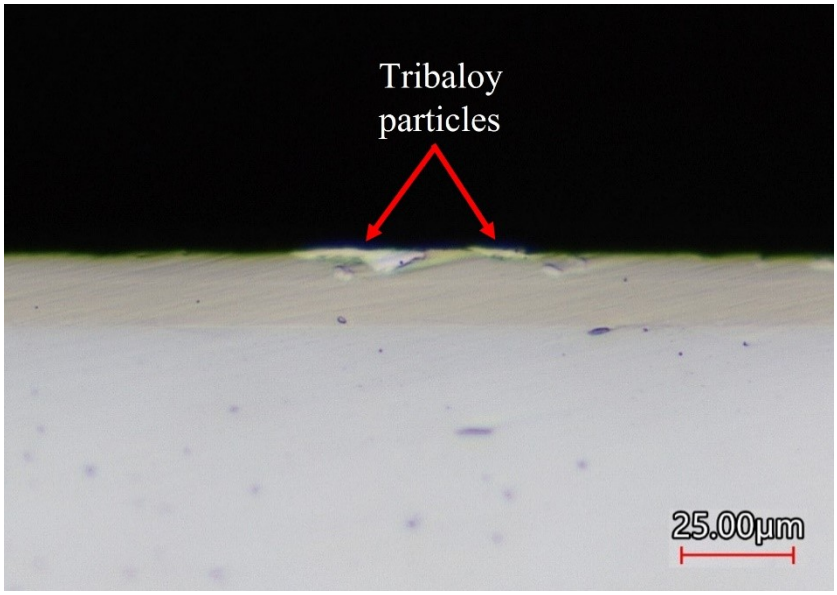

Figure 4 – 46: Cross-section of Ni-P-Tribaloy wear scar.

4.5.4 Wear Mechanisms

Based on the findings presented here, the wear mechanism of the Ni-P-Tribaloy composite coating can be described as follows: the Ni-P matrix above and around the Tribaloy particles is plastically deformed by the plowing mechanism while the particles are held in the matrix. Once the matrix around the particles is worn out and the particles are protruding, the particles are then pulled out leaving large gaps as they are large particles. The continuous plowing carries on removing the matrix material until the entire coating thickness is worn out. This mechanism is illustrated in the schematic given in Figure 4–47. The four steps are: plowing of the matrix, protrusion of reinforcement particles, particle pull-out, removal of the rest of the matrix while the trapped reinforcement particles contribute to the three-body abrasive wear. A similar wear mechanism was reported by Surzhenkov et al. [147] as they observed the wear process happening in two stages where the matrix is destroyed first then the loose reinforcement particles (WC-Co) were lost.

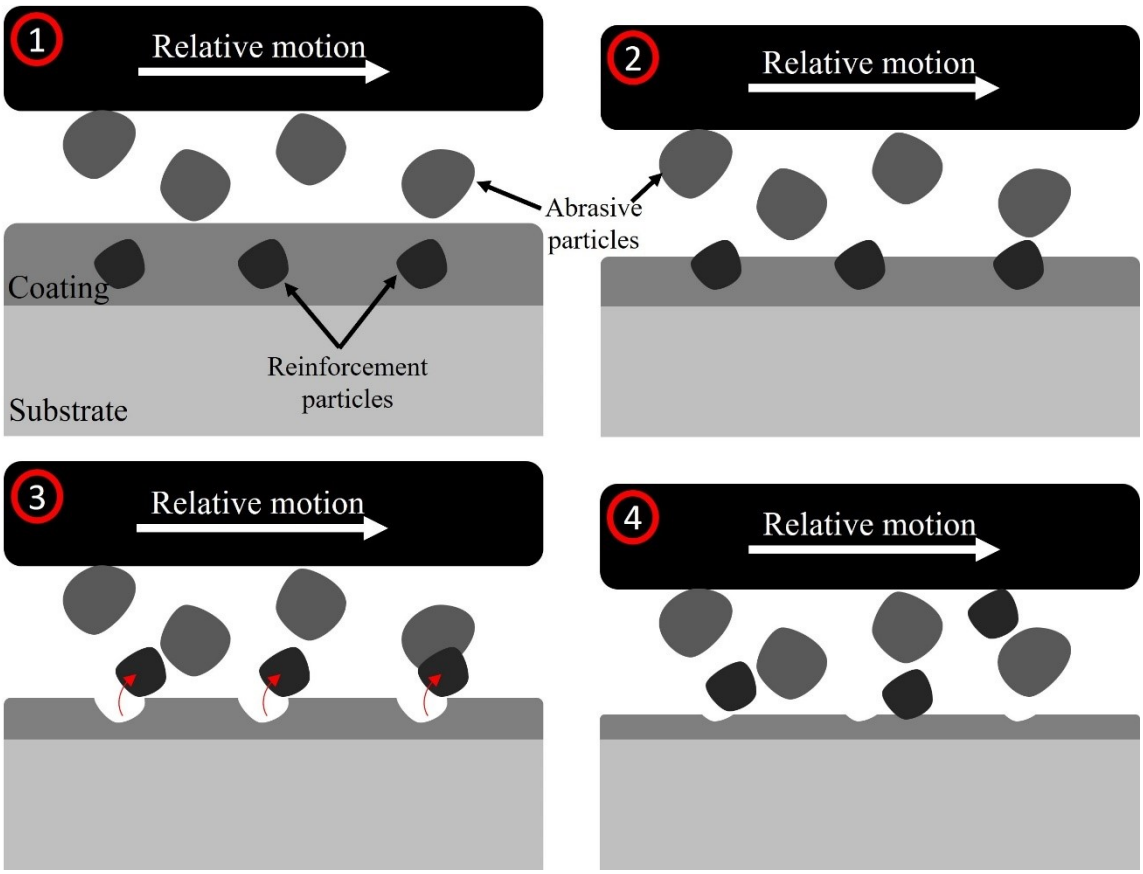

Figure 4 – 47: Schematic diagram of Ni-P-Tribaloy wear mechanism during abrasion.

Instances of this mechanism were captured by SEM in the abraded cross-section of the composite, verifying the existence of this wear mechanism. Figure 4–48 (a) points out a Tribaloy particle, in the worn-out matrix, that is slightly protruding and on the verge of being exposed as the Ni-P matrix around it continues to undergo further wear. This particle would then protrude out of the matrix enough to be pulled out of the matrix. Figure 4–48 (b) reveals areas of particle removal where the pulled out Tribaloy particles leave gaps in the matrix where they were once situated. It should be noted that those images are from different locations in the coating, however, they depict the steps outlined here as they are in different stages of the wear mechanism and they would follow the same steps under further wear.

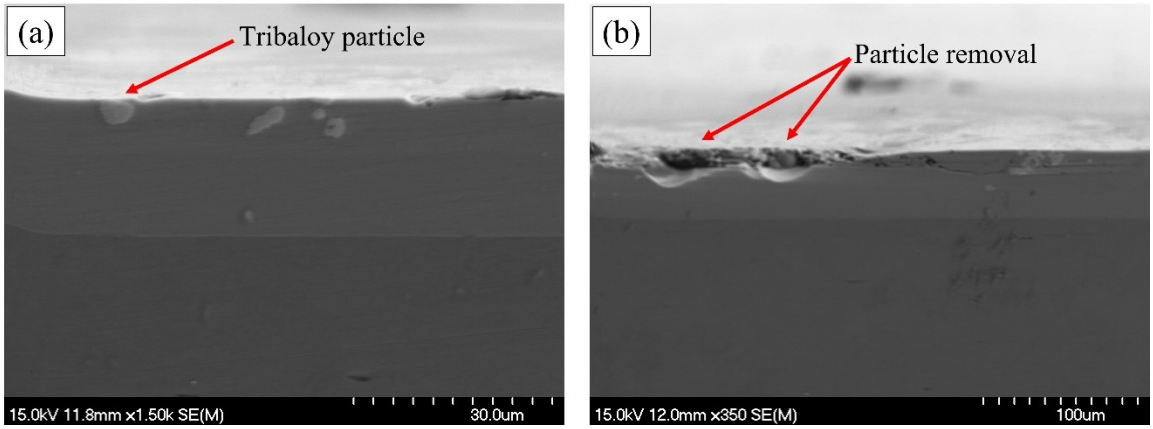

Figure 4 – 48: SEM images of (a) first step and (b) second step of particle removal.

Regarding the particle removal process itself within the described wear mechanism, consider the microscopic image given in Figure 4–49. It can be seen that the Tribaloy particle is beginning to detach from the matrix, likely accelerated by delamination. Delamination occurs under loading where the cracks develop beneath the surface, at maximum shear stress, and extend parallel to the surface ultimately causing delamination. When reinforcement particles are present, delamination will occur at the interface between the matrix and the particle as it is a weaker area, compared to the matrix and the particles. Researchers have reported that the interface plays an important role in this delamination mechanism. The particle–matrix interface has been established in the literature as a favorable area for crack formation and propagation during sliding wear of metal matrix composites (MMC), and that interfacial bond is stronger when the reinforcement particles are nano-sized over micro-sized [148]–[150]. Thus, the Tribaloy particle in Figure 4–49 is exhibiting detachment caused by delamination at the coating particle–matrix interface.

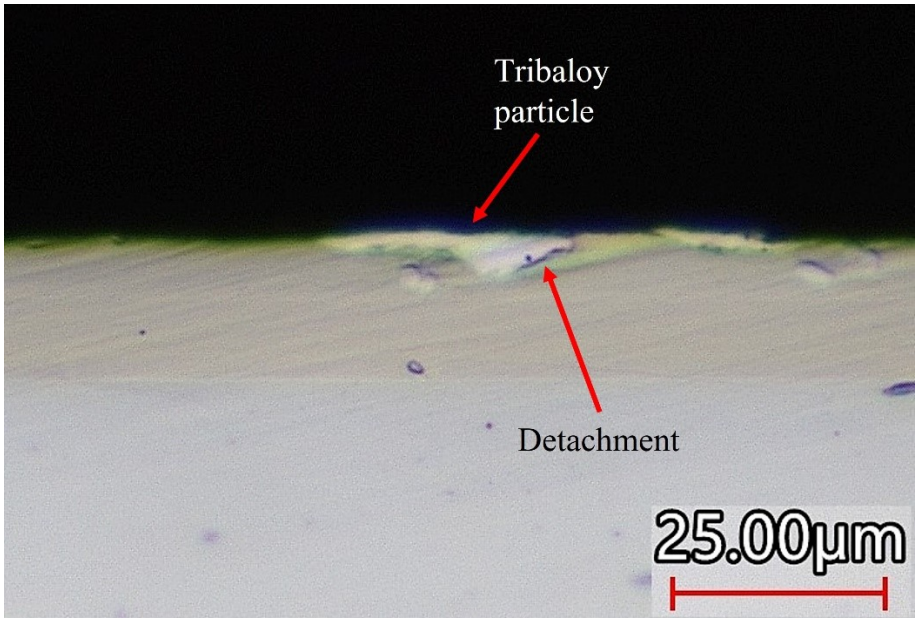

Figure 4 – 49: Detachment of Tribaloy particle from coating matrix.

Hence, the controlling parameters that influence the wear mechanism of the Ni-P-Tribaloy coating are the sizes of the reinforcing particles and abrasive particles, and the hardness of the overall coating matrix, the reinforcing particles, and abrasive particles.

Reddy et. al [42] suggested that the integrity of a Ni-P composite coatings can be improved with smaller particles as they are easier to be held by the matrix in a study that ascribed worse wear resistance to larger second phase particles. Smaller particles also ensure the uniform distribution of reinforcing particles across the coating thickness. The higher wear rate of the Ni-P-Tribaloy compared to the monolithic Ni-P coating in the results (section 3.3) was mainly attributed to the high surface roughness and particle pull-out, both are directly linked to the large Tribaloy particles size. Moreover, studies comparing micro- and nano- sized particles in MMCs have shown that micro-sized particles exhibit higher wear loss due to delamination, while nano-sized particles provided better resistance to delamination due to having stronger bonding at the particle–matrix interface where delamination occurs [148], [150]. Also, larger particles leave larger gaps when they are pulled out, hence, the measured wear loss will be higher.

Particle pull-out was also linked to the abrasive particles size in the results presented earlier. The larger the abrasive particles, the more prominent particle pull-out

becomes over wear by loss of matrix. Also, the more rounded the abrasive particles are, plowing becomes the more dominant mechanism over cutting, which is more severe and leads to deeper grooves when the abrasives have sharp edges [118]. Some micro-cutting was observed here because the abrasive particles used are semi-angular. The literature suggests that micro-cutting is present when the hardness of the abrasives are higher than the hardness of the abraded surface [147]. The composite coating hardness is 6.00 GPa and the Ottawa silica sand used in this test typically has hardness values around 10.7–13.0 GPa [151], [152].

The overall hardness of the composite coating matrix influences the wear resistance positively such that depth of the wear grooves on the abraded surface is shallower when the surface of the material is harder. The hardness of the Tribaloy particles themselves makes it more difficult for them to be pulled out from the matrix from plowing. Wear loss from particle pull-out is discussed extensively in this study, however, as long as the particles are embedded in the matrix and not protruding out of it, they are able to resist plowing. The hardness of the Tribaloy particles is also evident in all the provided figures where none of particles were fractured at different stages of wear.

Chapter 5 – Conclusions and Recommendations

In conclusion, electroless Ni-P-Tribaloy composite coatings were successfully deposited on AISI 1018 steel substrates. XRD and SEM/EDS verified the deposition of the coating and showed the distribution of the second-phase particles in the matrix with excellent bonding to the substrate. The composite coating contained 15.7 vol.% Tribaloy and had the chemical composition of 74.62 wt.% Ni, 8.88 wt.% P, 8.33 wt.% Co, 3.94 wt.% Cr, 2.81 wt.% Mo, and 1.42 wt.% Si. The composite coating was characterized through several tests to evaluate the effect of the addition of Tribaloy particles as second phase particles in Ni-P coatings. The Ni-P-Tribaloy coating had a micro-hardness of 6.00 GPa, a 12% increase over the Ni-P coating due to the high hardness of the Tribaloy particles. The composite coating also exhibited higher surface roughness and coefficient of friction.

The indentation behavior of the Ni-P-Tribaloy composite coating was found to be superior to the Ni-P coating under the same test conditions. It exhibited remarkably less severe cracking events from acoustic emissions, a reduction in crack size on the surface, and minimal cracking along with shallow cracks on the cross-section. The toughening mechanisms micro-cracking, crack bridging, crack arrest, and crack deflection were identified. The toughness of the composite coating was estimated to be four times higher than that of the monolithic coating, due to the inclusion of Tribaloy.

Despite greater volume loss during scratching, the Ni-P-Tribaloy displayed more ductile behavior having significantly more pile-up along the edges of the tracks at each number of passes. The dominant wear mechanism was recognized as material removal and minimal cracking was observed compared to the Ni-P coating, demonstrating an increase in toughness due to the addition of Tribaloy particles. The composite coating experienced greater volume loss due to the particles being removed from the wear track and causing three-body wear. The large particle size is believed to enhance the wear rate.

Low-stress abrasion test revealed greater volume loss and wear rate for the Ni-P-Tribaloy due to the large size of Tribaloy particles. The composite coating had almost double the volume loss after 50 revolutions and a higher wear rate of 0.170 mm^3 per revolution, compared to 0.135 mm^3 per revolution for the monolithic coating. The abrasive

wear in the Ni-P-Tribaloy coating was found has two main stages: plowing of the Ni-P matrix, followed by the removal of the Tribaloy particles which is caused by delamination that occurs at the coating particle–matrix interface. The large size of the Tribaloy contributes significantly to the wear of the composite coating as it increases the roughness, leaves large gaps, and enhances the delamination at the particle–matrix interface bonding.

Considering those findings, the following conclusions can be drawn:

1. The addition of Tribaloy particles enhances the hardness and the fracture toughness of Ni-P coatings, and they promote ductile behaviour during wear.
2. Tribaloy improves Ni-P's resistance to cracking by reducing the size and severity of cracks as they induce the toughening mechanisms of micro-cracking, micro-cracking, crack bridging, crack arrest, and crack deflection.
3. Ni-P-Tribaloy exhibits higher wear rates under sliding wear mainly due to the large size of the Tribaloy particles used in this research.

The following work is recommended to further understand the behaviour of this novel composite coating:

1. Further studies using finer Tribaloy particles, preferably nano-sized, to potentially improve the wear resistance of the composite coating.
2. Corrosion testing, especially erosion-corrosion, to further assess the suitability of Ni-P-Tribaloy for oil and gas pipeline protection applications.
3. Examine the effect of annealing heat treatment on the properties and wear behaviour of the Ni-P-Tribaloy coating.

Publications generated from this thesis include:

1. A. Mabrouk and Z. Farhat, "Novel Ni-P-Tribaloy Composite Protective Coating," *Materials*, vol. 16, no. 11, p. 3949, May 2023, doi: 10.3390/ma16113949.
2. A. Mabrouk, Z. Farhat, M.A. Islam, "Low-Stress Abrasion of Novel Ni-P-Tribaloy Composite Coating," Submitted, *Coatings*.

References

[1] M. Shehadeh, M. Anany, K. M. Saqr, and I. Hassan, "Experimental investigation of erosion-corrosion phenomena in a steel fitting due to plain and slurry seawater flow," *Int J Mech Mater Eng*, vol. 9, no. 1, p. 22, Dec. 2014, doi: 10.1186/s40712-014-0022-7.

[2] American Petroleum Institute, "Damage Mechanisms Affecting Fixed Equipment in the Refining Industry, Third Edition," Dallas, TX, API RP 571, Mar. 2020.

[3] D. Cronin, "Assessment of Corrosion Defects in Pipelines," University of Waterloo, Waterloo, ON, 2000.

[4] K. Green and T. Jackson, "Safety in the Transportation of Oil and Gas," Fraser Institute, Aug. 2015.

[5] Canadian Energy Pipeline Association, "CEPA 2021 Transmission Pipeline Industry Performance Report," Canadian Energy Pipeline Association, 2021. Accessed: Dec. 13, 2021. [Online]. Available: https://pr21.cepa.com/benefits-and-performance/

[6] M. MacLean, "Development and Characterization of Electroless Ni-P Composite Coatings with Superelastic nano-NiTi Additions," Dalhousie University, Halifax, NS, 2019.

[7] E. M. Fayyad, A. M. Abdullah, M. K. Hassan, A. M. Mohamed, G. Jarjoura, and Z. Farhat, "Recent advances in electroless-plated Ni-P and its composites for erosion and corrosion applications: a review," *emergent mater.*, vol. 1, no. 1–2, pp. 3–24, Jun. 2018, doi: 10.1007/s42247-018-0010-4.

[8] J. N. Balaraju, A. Priyadarshi, V. Kumar, N. T. Manikandanath, P. P. Kumar, and B. Ravisankar, "Hardness and wear behaviour of electroless Ni–B coatings," *Materials Science and Technology*, vol. 32, no. 16, pp. 1654–1665, Nov. 2016, doi: 10.1080/02670836.2015.1137683.

[9] R. C. Agarwala and V. Agarwala, "Electroless alloy/composite coatings: A review," *Sadhana*, vol. 28, no. 3–4, pp. 475–493, Jun. 2003, doi: 10.1007/BF02706445.

[10] J. Sudagar, J. Lian, and W. Sha, "Electroless nickel, alloy, composite and nano coatings – A critical review," *Journal of Alloys and Compounds*, vol. 571, pp. 183–204, Sep. 2013, doi: 10.1016/j.jallcom.2013.03.107.

[11] Y. F. Shen, W. Y. Xue, Z. Y. Liu, and L. Zuo, "Nanoscratching deformation and fracture toughness of electroless Ni–P coatings," *Surface and Coatings Technology*, vol. 205, no. 2, pp. 632–640, Oct. 2010, doi: 10.1016/j.surfcoat.2010.07.066.

[12] C. Wang, Z. Farhat, G. Jarjoura, M. K. Hassan, and A. M. Abdullah, “Indentation and erosion behavior of electroless Ni-P coating on pipeline steel,” *Wear*, vol. 376–377, pp. 1630–1639, Apr. 2017, doi: 10.1016/j.wear.2016.12.054.

[13] O. Fayyaz *et al.*, “Enhancement of mechanical and corrosion resistance properties of electrodeposited Ni–P–TiC composite coatings,” *Sci Rep*, vol. 11, no. 1, p. 5327, Mar. 2021, doi: 10.1038/s41598-021-84716-6.

[14] S. A. Alidokht *et al.*, “Microstructure and mechanical properties of Tribaloy coatings deposited by high-velocity oxygen fuel,” *J Mater Sci*, vol. 57, no. 42, pp. 20056–20068, Nov. 2022, doi: 10.1007/s10853-022-07843-z.

[15] C. A. Loto, “Electroless Nickel Plating – A Review,” *Silicon*, vol. 8, no. 2, pp. 177–186, Apr. 2016, doi: 10.1007/s12633-015-9367-7.

[16] G. O. Mallory and American Electroplaters and Surface Finishers Society, Eds., *Electroless plating: fundamentals and applications*. Orlando, Fla: American Electroplaters and Surface Finishers Soc, 1990.

[17] F. A. Roux, “Process of producing metallic deposits,” US1207218A, Dec. 05, 1916 Accessed: Dec. 09, 2021. [Online]. Available: https://patents.google.com/patent/US1207218A/en

[18] A. Brenner and G. E. Riddell, “Nickel plating on steel by chemical reduction,” *J. RES. NATL. BUR. STAN.*, vol. 37, no. 1, p. 31, Jul. 1946, doi: 10.6028/jres.037.019.

[19] A. Brenner and G. Riddell, “Deposition of nickel and cobalt by chemical reduction,” *J. RES. NATL. BUR. STAN.*, vol. 39, no. 5, p. 385, Nov. 1947, doi: 10.6028/jres.039.024.

[20] Electro-Coating, “Electroless Nickel Plating (Mil-C-26074E, ASTM B733-97, ASM 2404E, ASM 2404B) | Electro-Coating.” https://www.electro-coatings.com/electroless-nickel-plating.php (accessed Dec. 09, 2021).

[21] P. Sahoo and S. K. Das, “Tribology of electroless nickel coatings – A review,” *Materials & Design*, vol. 32, no. 4, pp. 1760–1775, Apr. 2011, doi: 10.1016/j.matdes.2010.11.013.

[22] L. Li, M. An, and G. Wu, “A new electroless nickel deposition technique to metallise SiCp/Al composites,” *Surface and Coatings Technology*, vol. 200, no. 16–17, pp. 5102–5112, Apr. 2006, doi: 10.1016/j.surfcoat.2005.05.031.

[23] O. C. Osifuye, “Electrochemical corrosion resistance of electroless plated mild steel.,” Tshwane University of Technology, South Africa, 2014.

[24] L. L. Lobanova, E. V. Batalova, and Y. P. Khranilov, “Reagent techniques for nickel recovery from spent electroless nickel-plating solutions,” *Russian journal of applied chemistry*, vol. 81, no. 2, pp. 202-, 2008, doi: 10.1007/s11167-008-2008-9.

[25] R. H. Guo, S. X. Jiang, C. W. M. Yuen, M. C. F. Ng, J. W. Lan, and G. H. Zheng, "Influence of deposition parameters and kinetics of electroless Ni-P plating on polyester fiber," *Fibers Polym*, vol. 13, no. 8, pp. 1037–1043, Oct. 2012, doi: 10.1007/s12221-012-1037-4.

[26] Z. Chen, X. Xu, C. C. Wong, and S. Mhaisalkar, "Effect of plating parameters on the intrinsic stress in electroless nickel plating," *Surface and Coatings Technology*, vol. 167, no. 2–3, pp. 170–176, Apr. 2003, doi: 10.1016/S0257-8972(02)00911-8.

[27] F. Braun, A. M. Tarditi, and L. M. Cornaglia, "Optimization and characterization of electroless co-deposited PdRu membranes: Effect of the plating variables on morphology," *Journal of Membrane Science*, vol. 382, no. 1–2, pp. 252–261, Oct. 2011, doi: 10.1016/j.memsci.2011.08.019.

[28] Z. Li, "ELECTROLESS Ni-P-Ti BASED NANOCOMPOSITE COATINGS," Dalhousie University, Halifax, NS, 2021.

[29] R. Jensen, "Wear and Erosion-Corrosion Behaviour of Electroless Ni-P Composite Coatings with NiTi Nanoparticle Additions," Dalhousie University, Halifax, NS, 2022.

[30] R. Taheri, "Evaluation of Electroless Nickel-Phosphorus (EN) Coatings," University of Saskatchewan, Saskatoon, 2003.

[31] J. Qi, B. Huang, Z. Wang, H. Ding, J. Xi, and W. Fu, "Dependence of corrosion resistance on grain boundary characteristics in a high nitrogen CrMn austenitic stainless steel," *Journal of Materials Science & Technology*, vol. 33, no. 12, pp. 1621–1628, Dec. 2017, doi: 10.1016/j.jmst.2017.09.016.

[32] M. Islam *et al.*, "Influence of SiO 2 nanoparticles on hardness and corrosion resistance of electroless Ni–P coatings," *Surface and Coatings Technology*, vol. 261, pp. 141–148, Jan. 2015, doi: 10.1016/j.surfcoat.2014.11.044.

[33] C. T. J. Low, R. G. A. Wills, and F. C. Walsh, "Electrodeposition of composite coatings containing nanoparticles in a metal deposit," *Surface and Coatings Technology*, vol. 201, no. 1–2, pp. 371–383, Sep. 2006, doi: 10.1016/j.surfcoat.2005.11.123.

[34] J. N. Balaraju, T. S. N. Sankara Narayanan, and S. K. Seshadri, "Electroless Ni–P composite coatings," *Journal of Applied Electrochemistry*, vol. 33, no. 9, pp. 807–816, Sep. 2003, doi: 10.1023/A:1025572410205.

[35] M. Lekka, D. Koumoulis, N. Kouloumbi, and P. L. Bonora, "Mechanical and anticorrosive properties of copper matrix micro- and nano-composite coatings," *Electrochimica Acta*, vol. 54, no. 9, pp. 2540–2546, Mar. 2009, doi: 10.1016/j.electacta.2008.04.060.

[36] Y. Z. Zhang, Y. Y. Wu, K. N. Sun, and M. Yao, “Characterization of electroless Ni--P--PTFE composite deposits,” *Journal of Materials Science Letters*, vol. 17, no. 2, pp. 119–122, 1997, doi: 10.1023/A:1006530732724.

[37] A. Grosjean, M. Rezrazi, J. Takadoum, and P. Berçot, “Hardness, friction and wear characteristics of nickel-SiC electroless composite deposits,” *Surface and Coatings Technology*, vol. 137, no. 1, pp. 92–96, Mar. 2001, doi: 10.1016/S0257-8972(00)01088-4.

[38] I. Apachitei, J. Duszczyk, L. Katgerman, and P. J. B. Overkamp, “Electroless Ni–P Composite Coatings: The Effect of Heat Treatment on the Microhardness of Substrate and Coating,” *Scripta Materialia*, vol. 38, no. 9, pp. 1347–1353, Apr. 1998, doi: 10.1016/S1359-6462(98)00054-2.

[39] S. Karthikeyan and B. Ramamoorthy, “Effect of reducing agent and nano Al2O3 particles on the properties of electroless Ni–P coating,” *Applied Surface Science*, vol. 307, pp. 654–660, Jul. 2014, doi: 10.1016/j.apsusc.2014.04.092.

[40] M. R. Kalantary, K. A. Holbrook, and P. B. Wells, “Optimisation of a Bath for Electroless Plating and Its Use for the Production of Nickel-Phosphorus-Silicon Carbide Coatings,” *Transactions of the IMF*, vol. 71, no. 2, pp. 55–61, Jan. 1993, doi: 10.1080/00202967.1993.11870987.

[41] B. Durkin, “Controlling Electroless Nickel Baths,” *Products Finishing*, Oct. 01, 1998. https://www.pfonline.com/articles/controlling-electroless-nickel-baths (accessed Dec. 11, 2021).

[42] V. V. N. Reddy, B. Ramamoorthy, and P. K. Nair, “A study on the wear resistance of electroless Ni–P/Diamond composite coatings,” *Wear*, vol. 239, no. 1, pp. 111–116, Apr. 2000, doi: 10.1016/S0043-1648(00)00330-6.

[43] J. N. Balaraju, Kalavati, and K. S. Rajam, “Influence of particle size on the microstructure, hardness and corrosion resistance of electroless Ni–P–Al2O3 composite coatings,” *Surface and Coatings Technology*, vol. 200, no. 12–13, pp. 3933–3941, Mar. 2006, doi: 10.1016/j.surfcoat.2005.03.007.

[44] J. N. Balaraju and S. K. Seshadri, “Preparation and Characterization of Electroless Ni-P and Ni-P-Si $_3$ N $_4$ Composite Coatings,” *Transactions of the IMF*, vol. 77, no. 2, pp. 84–86, Jan. 1999, doi: 10.1080/00202967.1999.11871253.

[45] Z. Abdel Hamid and M. T. Abou Elkhair, “Development of electroless nickel–phosphorous composite deposits for wear resistance of 6061 aluminum alloy,” *Materials Letters*, vol. 57, no. 3, pp. 720–726, Dec. 2002, doi: 10.1016/S0167-577X(02)00860-1.

[46] M. Izzard and J. K. Dennis, “Deposition and properties of electroless nickel/graphite coatings,” *Transactions of the IMF*, vol. 65, no. 1, pp. 85–89, Jan. 1987, doi: 10.1080/00202967.1987.11870778.

[47] M.-D. Ger and B. J. Hwang, “Effect of surfactants on codeposition of PTFE particles with electroless Ni-P coating,” *Materials Chemistry and Physics*, vol. 76, no. 1, pp. 38–45, Jul. 2002, doi: 10.1016/S0254-0584(01)00513-2.

[48] S. M. Moonir-Vaghefi, A. Saatchi, and J. Hejazi, “Deposition and properties of electroless nickel-phosphorus-molybdenum disulfide composites,” *Metal Finishing*, vol. 95, no. 11, pp. 46–52, Nov. 1997, doi: 10.1016/S0026-0576(97)81449-3.

[49] L.-G. Yu and X.-S. Zhang, “The friction and wear properties of electroless Ni-polytetrafluoroethylene composite coating,” *Thin Solid Films*, vol. 245, no. 1–2, pp. 98–103, Jun. 1994, doi: 10.1016/0040-6090(94)90883-4.

[50] B. Łosiewicz, A. Stępień, D. Gierlotka, and A. Budniok, “Composite layers in Ni–P system containing TiO2 and PTFE,” *Thin Solid Films*, vol. 349, no. 1–2, pp. 43–50, Jul. 1999, doi: 10.1016/S0040-6090(99)00175-3.

[51] J. K. Dennis, S. T. Sheikh, and E. C. Silverstone, “Electroless Composite Coatings for Wear Resistant Applications,” *Transactions of the IMF*, vol. 59, no. 1, pp. 118–122, Jan. 1981, doi: 10.1080/00202967.1981.11870574.

[52] B. Bozzini, C. Martini, P. L. Cavallotti, and E. Lanzoni, “Relationships among crystallographic structure, mechanical properties and tribological behaviour of electroless Ni–P(9%)/B4C films,” *Wear*, vol. 225–229, pp. 806–813, Apr. 1999, doi: 10.1016/S0043-1648(98)00389-5.

[53] W. Chen, W. Gao, and Y. He, “A novel electroless plating of Ni–P–TiO2 nano-composite coatings,” *Surface and Coatings Technology*, vol. 204, no. 15, pp. 2493–2498, Apr. 2010, doi: 10.1016/j.surfcoat.2010.01.032.

[54] G. Jiaqiang, L. Lei, W. Yating, S. Bin, and H. Wenbin, “Electroless Ni–P–SiC composite coatings with superfine particles,” *Surface and Coatings Technology*, vol. 200, no. 20–21, pp. 5836–5842, May 2006, doi: 10.1016/j.surfcoat.2005.08.134.

[55] J. N. Balaraju and K. S. Rajam, “Electroless deposition and characterization of high phosphorus13; Ni-P-Si3N4 composite coatings,” *International Journal of Electrochemical Science*, vol. 2, pp. 747–761, Oct. 2007.

[56] Y. S. Huang, X. T. Zeng, I. Annergren, and F. M. Liu, “Development of electroless NiP–PTFE–SiC composite coating,” *Surface and Coatings Technology*, vol. 167, no. 2–3, pp. 207–211, Apr. 2003, doi: 10.1016/S0257-8972(02)00899-X.

[57] W. Metzger and Th. Florian, “The Deposition of Dispersion Hardened Coatings by Means of Electroless Nickel,” *Transactions of the IMF*, vol. 54, no. 1, pp. 174–177, Jan. 1976, doi: 10.1080/00202967.1976.11870394.

[58] K. PARKER, “HARDNESS AND WEAR RESISTANCE TESTS OF ELECTROLESS NICKEL DEPOSITS,” *PLATING*, vol. 61, pp. 834–841, 1974.

[59] I. Apachitei, F. D. Tichelaar, J. Duszczyk, and L. Katgerman, “The effect of heat treatment on the structure and abrasive wear resistance of autocatalytic NiP and NiP–SiC coatings,” *Surface and Coatings Technology*, vol. 149, no. 2–3, pp. 263–278, Jan. 2002, doi: 10.1016/S0257-8972(01)01492-X.

[60] Y. LI, “Investigation of electroless Ni-P-SiC composite coatings,” *Plat. surf. finish*, vol. 84, no. 11, pp. 77–81, 1997.

[61] G. Straffelini, D. Colombo, and A. Molinari, “Surface durability of electroless Ni–P composite deposits,” *Wear*, vol. 236, no. 1–2, pp. 179–188, Dec. 1999, doi: 10.1016/S0043-1648(99)00273-2.

[62] L. Y. Wang *et al.*, “Friction and wear behavior of electroless Ni-based CNT composite coatings,” *Wear*, vol. 254, no. 12, pp. 1289–1293, Nov. 2003, doi: 10.1016/S0043-1648(03)00171-6.

[63] W. X. Chen *et al.*, “Wear and Friction of Ni-P Electroless Composite Coating Including Inorganic Fullerene-WS2 Nanoparticles,” *Adv. Eng. Mater.*, vol. 4, no. 9, pp. 686–690, Sep. 2002, doi: 10.1002/1527-2648(20020916)4:9<686::AID-ADEM686>3.0.CO;2-I.

[64] N. Feldstein, T. Lancsek, D. Lindsay, and L. Salerno, “Electroless Composite Plating,” *Metal Finishing*, pp. 35–51, Aug. 1983.

[65] M. Islam, M. R. Azhar, N. Fredj, and T. D. Burleigh, “Electrochemical impedance spectroscopy and indentation studies of pure and composite electroless Ni–P coatings,” *Surface and Coatings Technology*, vol. 236, pp. 262–268, Dec. 2013, doi: 10.1016/j.surfcoat.2013.09.057.

[66] L. Masry *et al.*, “Development Of Novel Corrosion Resistant Electroless Ni-P Composite Coatings For Pipeline Steel,” *INTERNATIONAL JOURNAL OF ENGINEERING SCIENCES & RESEARCH TECHNOLOGY*, vol. 7, pp. 122–134, Mar. 2018, doi: 10.5281/ZENODO.1189054.

[67] J. Balaraju, T. Sankara Narayanan, and S. Seshadri, “Evaluation of the corrosion resistance of electroless Ni-P and Ni-P composite coatings by electrochemical impedance spectroscopy,” *J Solid State Electrochem*, vol. 5, no. 5, pp. 334–338, Jul. 2001, doi: 10.1007/s100080000159.

[68] A. A. Zuleta *et al.*, “Preparation and characterization of electroless Ni–P–Fe3O4 composite coatings and evaluation of its high temperature oxidation behaviour,” *Surface and Coatings Technology*, vol. 203, no. 23, pp. 3569–3578, Aug. 2009, doi: 10.1016/j.surfcoat.2009.05.025.

[69] S. Ranganatha, T. V. Venkatesha, and K. Vathsala, “Development of electroless Ni–Zn–P/nano-TiO2 composite coatings and their properties,” *Applied Surface Science*, vol. 256, no. 24, pp. 7377–7383, Oct. 2010, doi: 10.1016/j.apsusc.2010.05.076.

[70] H. M. Jin, S. H. Jiang, and L. N. Zhang, “Microstructure and corrosion behavior of electroless deposited Ni–P/CeO2 coating,” *Chinese Chemical Letters*, vol. 19, no. 11, pp. 1367–1370, Nov. 2008, doi: 10.1016/j.cclet.2008.06.040.

[71] F. Hubbell, “CHEMICALLY DEPOSITED COMPOSITES - A NEW GENERATION OF ELECTROLESS COATINGS.,” *Plating and Surface Finishing*, vol. 65, pp. 58–62, Dec. 1978.

[72] M. Mohammadi and M. Ghorbani, “Wear and corrosion properties of electroless nickel composite coatings with PTFE and/or MoS2 particles,” *J Coat Technol Res*, vol. 8, no. 4, pp. 527–533, Jul. 2011, doi: 10.1007/s11998-011-9329-y.

[73] M. A. Shoeib, S. M. Mokhtar, and M. A. Abd El-Ghaffar, “Mechanical and corrosion protection properties of electroless nickel-polymer composite coatings,” *Metal Finishing*, vol. 96, no. 11, pp. 58–59, Nov. 1998, doi: 10.1016/S0026-0576(98)80873-8.

[74] W. Xu, R. Liu, P. C. Patnaik, M. X. Yao, and X. J. Wu, “Mechanical and tribological properties of newly developed Tribaloy alloys,” *Materials Science and Engineering: A*, vol. 452–453, pp. 427–436, Apr. 2007, doi: 10.1016/j.msea.2006.10.088.

[75] AMETEK Specialty Metal Products, “Tribaloy T-400 T-800 Powders,” *Metal Powders & Clad Plate Manufacturer*. https://www.powderclad.com/products/specialty-powders/www.powderclad.com/products/specialty-powders/t400-t800-tribaloy-powders (accessed Dec. 09, 2021).

[76] Durejko, Łazińska, Dworecka-Wójcik, Lipiński, Varin, and Czujko, “The Tribaloy T-800 Coatings Deposited by Laser Engineered Net Shaping (LENSTM),” *Materials*, vol. 12, no. 9, p. 1366, Apr. 2019, doi: 10.3390/ma12091366.

[77] Deloro, “Metallurgical Expertise.” https://www.deloro.com/solutions/metallurgical-expertise/ (accessed Dec. 09, 2021).

[78] International Trade Winds, “TRIBALOY T-800.” https://www.itwmetals.com.br/en/c/cobalt-alloys/tribaloy-t-800.html (accessed Dec. 09, 2021).

[79] M. X. Yao, J. B. C. Wu, S. Yick, Y. Xie, and R. Liu, “High temperature wear and corrosion resistance of a Laves phase strengthened Co–Mo–Cr–Si alloy,” *Materials Science and Engineering: A*, vol. 435–436, pp. 78–83, Nov. 2006, doi: 10.1016/j.msea.2006.07.054.

[80] D. RAGHU, “Recent developments in wear-and corrosion-resistant alloys for the oil industry,” *Materials performance*, vol. 36, no. 11, pp. 27–36, 1997.

[81] H. Sandhu and M. Kumar, “High-Temperature Hardness and Wear Resistance of Cobalt-Based Tribaloy Alloys,” *IJESC*, vol. 7, no. 3, 2017.

[82] C. B. Cameron and D. P. Ferriss, “Tribaloy Intermetallic Materials: New Wear- and Corrosion-Resistant Alloys,” *Anti-Corrosion Meth & Material*, vol. 22, no. 4, pp. 5–8, Apr. 1975, doi: 10.1108/eb010165.

[83] R. Liu, J. Yao, Q. Zhang, M. X. Yao, and R. Collier, “Effects of Silicon Content on the Microstructure and Mechanical Properties of Cobalt-Based Tribaloy Alloys,” *Journal of Engineering Materials and Technology*, vol. 138, no. 4, p. 041017, Oct. 2016, doi: 10.1115/1.4034075.

[84] A. Halstead and R. D. Rawlings, “Structure and hardness of Co–Mo–Cr–Si wear resistant alloys (Tribaloys),” *Metal Science*, vol. 18, no. 10, pp. 491–500, Oct. 1984, doi: 10.1179/030634584790253146.

[85] S. E. Mason and R. D. Rawlings, “Structure and hardness of Ni–Mo–Cr–Si wear and corrosion resistant alloys,” *Materials Science and Technology*, vol. 5, no. 2, pp. 180–185, Feb. 1989, doi: 10.1179/mst.1989.5.2.180.

[86] E. Díaz, J. M. Amado, J. Montero, M. J. Tobar, and A. Yáñez, “Comparative Study of Co-based Alloys in Repairing Low Cr-Mo steel Components by Laser Cladding,” *Physics Procedia*, vol. 39, pp. 368–375, 2012, doi: 10.1016/j.phpro.2012.10.050.

[87] C. Navas, M. Cadenas, J. M. Cuetos, and J. de Damborenea, “Microstructure and sliding wear behaviour of Tribaloy T-800 coatings deposited by laser cladding,” *Wear*, vol. 260, no. 7–8, pp. 838–846, Apr. 2006, doi: 10.1016/j.wear.2005.04.020.

[88] M. J. Tobar, J. M. Amado, C. Álvarez, A. García, A. Varela, and A. Yáñez, “Characteristics of Tribaloy T-800 and T-900 coatings on steel substrates by laser cladding,” *Surface and Coatings Technology*, vol. 202, no. 11, pp. 2297–2301, Feb. 2008, doi: 10.1016/j.surfcoat.2007.11.025.

[89] P. D. Wood, H. E. Evans, and C. B. Ponton, “Investigation into the wear behaviour of Tribaloy 400C during rotation as an unlubricated bearing at 600°C,” *Wear*, vol. 269, no. 11–12, pp. 763–769, Oct. 2010, doi: 10.1016/j.wear.2010.08.003.

[90] J. R. Davis, *Nickel, Cobalt, and Their Alloys*. ASM International, 2000.

[91] G. Bolelli, V. Cannillo, L. Lusvarghi, M. Montorsi, F. P. Mantini, and M. Barletta, “Microstructural and tribological comparison of HVOF-sprayed and post-treated M–Mo–Cr–Si (M=Co, Ni) alloy coatings,” *Wear*, vol. 263, no. 7–12, pp. 1397–1416, Sep. 2007, doi: 10.1016/j.wear.2006.12.002.

[92] T. Sahraoui, H. I. Feraoun, N. Fenineche, G. Montavon, H. Aourag, and C. Coddet, "HVOF-sprayed Tribaloy©-400: microstructure and first principle calculations," *Materials Letters*, vol. 58, no. 19, pp. 2433–2436, Jul. 2004, doi: 10.1016/j.matlet.2004.02.025.

[93] G. Bolelli and L. Lusvarghi, "Tribological properties of HVOF as-sprayed and heat treated Co–Mo–Cr–Si coatings," *Tribol Lett*, vol. 25, no. 1, pp. 43–54, Dec. 2006, doi: 10.1007/s11249-006-9136-2.

[94] G. J. Bruck, "Fundamentals And Industrial Applications Of High Power Laser Beam Cladding," presented at the SPIE International Symposium on Optical Engineering and Industrial Sensing for Advance Manufacturing Technologies, G. Sepold, Ed., Dearborn, MI, United States, Oct. 1988, p. 14. doi: 10.1117/12.947699.

[95] A. Frenk and W. Kurz, "High speed laser cladding: solidification conditions and microstructure of a cobalt-based alloy," *Materials Science and Engineering: A*, vol. 173, no. 1–2, pp. 339–342, Dec. 1993, doi: 10.1016/0921-5093(93)90240-F.

[96] S. Atamert and H. K. D. H. Bhadeshia, "Comparison of the microstructures and abrasive wear properties of stellite hardfacing alloys deposited by arc welding and laser cladding," *MTA*, vol. 20, no. 6, pp. 1037–1054, Jun. 1989, doi: 10.1007/BF02650140.

[97] J. Przybylowicz and J. Kusinski, "Laser cladding and erosive wear of Co–Mo–Cr–Si coatings," *Surface and Coatings Technology*, vol. 125, no. 1–3, pp. 13–18, Mar. 2000, doi: 10.1016/S0257-8972(99)00563-0.

[98] A. Tiziani, L. Giordano, P. Matteazzi, and B. Badan, "Laser stellite coatings on austenitic stainless steels," *Materials Science and Engineering*, vol. 88, pp. 171–175, Apr. 1987, doi: 10.1016/0025-5416(87)90082-6.

[99] S. T. Nyadongo, E. O. Olakanmi, and S. L. Pityana, "Experimental and numerical analyses of geometrical and microstructural features of Tribaloy T-800 composite coating deposited via laser cladding-assisted with pre-heat (LCAP) process," *Journal of Manufacturing Processes*, vol. 69, pp. 84–111, Sep. 2021, doi: 10.1016/j.jmapro.2021.07.043.

[100] P. Farahmand, "Experimental and numerical investigation on cladding of corrosion-erosion resistant materials by a high power direct diode laser," Southern Methodist University, Dallas, TX, 2015.

[101] A. R. K. Rana, "Synthesis & Characterization of Graphene Enhanced Electroless Ni-P Composite Coatings," Dalhousie University, Halifax, NS, 2020.

[102] H. Hertz, "On the contact of elastic solids," *Z. Reine Angew. Mathematik*, vol. 92, pp. 156–171, 1881.

[103] C. Wang, “Indentation and Fracture Behaviour of Electroless Ni-P-based Composite Coatings,” Dalhousie University, Halifax, NS, 2017.

[104] A. C. FISCHER-CRIPPS, “Predicting Hertzian fracture,” *Journal of Materials Science*, vol. 32, no. 5, pp. 1277–1285, Mar. 1997, doi: 10.1023/A:1018500522014.

[105] C. Kocer and R. E. Collins, “Angle of Hertzian Cone Cracks,” *Journal of the American Ceramic Society*, vol. 81, no. 7, pp. 1736–1742, Jan. 2005, doi: 10.1111/j.1151-2916.1998.tb02542.x.

[106] R. F. Cook and G. M. Pharr, “Direct Observation and Analysis of Indentation Cracking in Glasses and Ceramics,” *J American Ceramic Society*, vol. 73, no. 4, pp. 787–817, Apr. 1990, doi: 10.1111/j.1151-2916.1990.tb05119.x.

[107] A. Almotairi, A. Warkentin, and Z. Farhat, “Mechanical damage of hard chromium coatings on 416 stainless steel,” *Engineering Failure Analysis*, vol. 66, pp. 130–140, Aug. 2016, doi: 10.1016/j.engfailanal.2016.04.011.

[108] Z. Li and Z. Farhat, “Hertzian Indentation Behavior of Electroless Ni-P-Ti Composite Coatings,” *Metall Mater Trans A*, vol. 51, no. 7, pp. 3674–3691, Jul. 2020, doi: 10.1007/s11661-020-05795-0.

[109] K. T. Faber, T. Iwagoshi, and A. Ghosh, “Toughening by Stress-Induced Microcracking in Two-Phase Ceramics,” *J American Ceramic Society*, vol. 71, no. 9, p. C-399-C–401, Sep. 1988, doi: 10.1111/j.1151-2916.1988.tb06419.x.

[110] J. P. Singh, D. P. H. Hasselman, W. M. Su, J. A. Rubin, and R. Palicka, “Observations on the nature of micro-cracking in brittle composites,” *J Mater Sci*, vol. 16, no. 1, pp. 141–150, Jan. 1981, doi: 10.1007/BF00552068.

[111] J. D. Kuntz, G.-D. Zhan, and A. K. Mukherjee, “Nanocrystalline-Matrix Ceramic Composites for Improved Fracture Toughness,” *MRS Bull.*, vol. 29, no. 1, pp. 22–27, Jan. 2004, doi: 10.1557/mrs2004.12.

[112] X. Sun and J. A. Yeomans, “Ductile Phase Toughened Brittle Materials,” *Journal of materials science & technology*, vol. 12, no. 2, pp. 124–134, 1996.

[113] G. Bao and F. Zok, “On the strength of ductile particle reinforced brittle matrix composites,” *Acta Metallurgica et Materialia*, vol. 41, no. 12, pp. 3515–3524, Dec. 1993, doi: 10.1016/0956-7151(93)90231-G.

[114] R. O. Ritchie, “Mechanisms of fatigue crack propagation in metals, ceramics and composites: Role of crack tip shielding,” *Materials Science and Engineering: A*, vol. 103, no. 1, pp. 15–28, Aug. 1988, doi: 10.1016/0025-5416(88)90547-2.

[115] J. A. Yeomans, “Ductile particle ceramic matrix composites—Scientific curiosities or engineering materials?,” *Journal of the European Ceramic Society*, vol. 28, no. 7, pp. 1543–1550, Jan. 2008, doi: 10.1016/j.jeurceramsoc.2007.12.009.

[116] Y.-L. Shen and N. Chawla, “On the correlation between hardness and tensile strength in particle reinforced metal matrix composites,” *Materials Science and Engineering: A*, vol. 297, no. 1–2, pp. 44–47, Jan. 2001, doi: 10.1016/S0921-5093(00)01256-9.

[117] B. Bhushan, *Principles and Applications of Tribology*, Second edition. in Tribology series. Chichester, West Sussex, UK: Wiley, 2013.

[118] G. W. Stachowiak and A. W. Batchelor, *Engineering tribology*, Fourth edition. Amsterdam Heidelberg: Elsevier Butterworth-Heinemann, 2014.

[119] M. W. Hyttel, D. D. Olsson, G. Reisel, and J. Bøttiger, “Comparison of a newly developed compression-twist abrasive wear test with the ASTM G65 test method,” *Wear*, vol. 307, no. 1–2, pp. 134–141, Sep. 2013, doi: 10.1016/j.wear.2013.08.023.

[120] I. Hutchings and P. Shipway, *TRIBOLOGY: Friction and wear of engineering materials*, Second Editions. Cambridge, MA: Elsevier, 2017.

[121] S. Sundararajan and B. Bhushan, “Development of a continuous microscratch technique in an atomic force microscope and its application to study scratch resistance of ultrathin hard amorphous carbon coatings,” *J. Mater. Res.*, vol. 16, no. 2, pp. 437–445, Feb. 2001, doi: 10.1557/JMR.2001.0066.

[122] A. R. K. Rana and Z. Farhat, “Preparation and tribological characterization of graphene incorporated electroless Ni-P composite coatings,” *Surface and Coatings Technology*, vol. 369, pp. 334–346, Jul. 2019, doi: 10.1016/j.surfcoat.2019.04.043.

[123] J. A. Hawk, R. D. Wilson, J. H. Tylczak, and Ö. N. Doğan, “Laboratory abrasive wear tests: investigation of test methods and alloy correlation,” *Wear*, vol. 225–229, pp. 1031–1042, Apr. 1999, doi: 10.1016/S0043-1648(99)00042-3.

[124] ASTM International, “Standard Test Method for Measuring Abrasion Using the Dry Sand/Rubber Wheel Apparatus,” ASTM International, West Conshohocken, PA, G65-16, 2017.

[125] I. S. Raju and T. K. O’Brien, “Fracture mechanics concepts, stress fields, strain energy release rates, delamination initiation and growth criteria,” in *Delamination Behaviour of Composites*, Elsevier, 2008, pp. 3–27. doi: 10.1533/9781845694821.1.3.

[126] B.-Q. Yang, K. Zhang, G.-N. Chen, G.-X. Luo, and J.-H. Xiao, “Measurement of fracture toughness and interfacial shear strength of hard and brittle Cr coating on ductile steel substrate,” *Surface Engineering*, vol. 24, no. 5, pp. 332–336, Sep. 2008, doi: 10.1179/174329408X282587.

[127] M. A. Islam, “Erosion, Corrosion and Erosion-Corrosion of Oil and Gas Pipeline Steels,” Dalhousie University, Halifax, NS, 2015.

[128] A. C. Fischer-Cripps, *Nanoindentation*. in Mechanical Engineering Series. New York, NY: Springer New York, 2004. doi: 10.1007/978-1-4757-5943-3.

[129] ASTM International, "Test Method for Ranking Resistance of Materials to Sliding Wear Using Block-on-Ring Wear Test," ASTM International, West Conshohocken, PA, G77-17, 2017. doi: 10.1520/G0077-05R10.

[130] O. Güler, M. Kocaman, S. B. Akçay, H. Çuvalcı, and T. Varol, "Structure and tribological properties of composites based on a Novolac matrix with Ni P electrolytic coating," *Surface and Coatings Technology*, vol. 451, p. 129025, Dec. 2022, doi: 10.1016/j.surfcoat.2022.129025.

[131] M. K. Kokare, N. A. Jadhav, Y. Kumar, K. M. Jadhav, and S. M. Rathod, "Effect of Nd3+ doping on structural and magnetic properties of Ni0.5Co0.5Fe2O4 nanocrystalline ferrites synthesized by sol-gel auto combustion method," *Journal of Alloys and Compounds*, vol. 748, pp. 1053–1061, Jun. 2018, doi: 10.1016/j.jallcom.2018.03.168.

[132] R. Jensen, Z. Farhat, Md. A. Islam, and G. Jarjoura, "Effect of Coating Thickness on Wear Behaviour of Monolithic Ni-P and Ni-P-NiTi Composite Coatings," *Solids*, vol. 3, no. 4, pp. 620–642, Nov. 2022, doi: 10.3390/solids3040039.

[133] C. Wang, Z. Farhat, G. Jarjoura, M. K. Hassan, and A. M. Abdullah, "Indentation and bending behavior of electroless Ni-P-Ti composite coatings on pipeline steel," *Surface and Coatings Technology*, vol. 334, pp. 243–252, Jan. 2018, doi: 10.1016/j.surfcoat.2017.10.074.

[134] M. MacLean, Z. Farhat, G. Jarjoura, E. Fayyad, A. Abdullah, and M. Hassan, "Fabrication and investigation of the scratch and indentation behaviour of new generation Ni-P-nano-NiTi composite coating for oil and gas pipelines," *Wear*, vol. 426–427, pp. 265–276, Apr. 2019, doi: 10.1016/j.wear.2019.01.058.

[135] M. MacLean, Z. Farhat, G. Jarjoura, E. Fayyad, A. Abdullah, and M. Hassan, "Erosion and Toughening Mechanisms of Electroless Ni-P-Nano-NiTi Composite Coatings on API X100 Steel under Single Particle Impact," *JSEMAT*, vol. 09, no. 04, pp. 88–106, 2019, doi: 10.4236/jsemat.2019.94007.

[136] Z. Li, Z. Farhat, and Md. A. Islam, "Investigation of Single-Particle Erosion Behavior of Electroless Ni-P-Ti Composite Coatings," *J. of Materi Eng and Perform*, vol. 29, no. 3, pp. 1671–1685, Mar. 2020, doi: 10.1007/s11665-020-04722-z.

[137] Z. Li, Z. Farhat, G. Jarjoura, E. Fayyad, A. Abdullah, and M. Hassan, "Synthesis and Characterization of Scratch-Resistant Ni-P-Ti-Based Composite Coating," *Tribology Transactions*, vol. 62, no. 5, pp. 880–896, Sep. 2019, doi: 10.1080/10402004.2019.1634227.

[138] Z. Kamdi, P. H. Shipway, K. T. Voisey, and A. J. Sturgeon, “Abrasive wear behaviour of conventional and large-particle tungsten carbide-based cermet coatings as a function of abrasive size and type,” *Wear*, vol. 271, no. 9–10, pp. 1264–1272, Jul. 2011, doi: 10.1016/j.wear.2010.12.060.

[139] M. Kašparová, F. Zahálka, and Š. Houdková, “WC-Co and Cr3C2-NiCr Coatings in Low- and High-Stress Abrasive Conditions,” *J Therm Spray Tech*, vol. 20, no. 3, pp. 412–424, Mar. 2011, doi: 10.1007/s11666-010-9523-y.

[140] T. Liyanage, G. Fisher, and A. P. Gerlich, “Microstructures and abrasive wear performance of PTAW deposited Ni–WC overlays using different Ni-alloy chemistries,” *Wear*, vol. 274–275, pp. 345–354, Jan. 2012, doi: 10.1016/j.wear.2011.10.001.

[141] J. Hu, D. Y. Li, and R. Llewellyn, “Synergistic effects of microstructure and abrasion condition on abrasive wear of composites—A modeling study,” *Wear*, vol. 263, no. 1–6, pp. 218–227, Sep. 2007, doi: 10.1016/j.wear.2007.01.069.

[142] R. A. Al-Samarai, Haftirman, K. R. Ahmad, and Y. Al-Douri, “Evaluate the Effects of Various Surface Roughness on the Tribological Characteristics under Dry and Lubricated Conditions for Al-Si Alloy,” *JSEMAT*, vol. 02, no. 03, pp. 167–173, 2012, doi: 10.4236/jsemat.2012.23027.

[143] T. Hisakado, “The influence of surface roughness on abrasive wear,” *Wear*, vol. 41, no. 1, pp. 179–190, Jan. 1977, doi: 10.1016/0043-1648(77)90200-9.

[144] M. Hadinezhad, M. Elyasi, M. Rajabi, and M. Abbasi, “Study of the Effects of Slip Distance and Surface Roughness on Wear Rate,” *mst*, vol. 3, no. 4, pp. 146–154, Dec. 2015, doi: 10.13189/mst.2015.030412.

[145] R. C. Panziera, W. H. Flores, M. A. D. Tier, and A. C. C. De Oliveira, “Comparison of abrasive wear by rice husk of an HVOF WC–Co–Cr-based coating and an electric arc sprayed coating based on Fe–Cr–B–Si,” *J Braz. Soc. Mech. Sci. Eng.*, vol. 41, no. 8, p. 331, Aug. 2019, doi: 10.1007/s40430-019-1832-6.

[146] E. Rabinowicz, L. A. Dunn, and P. G. Russell, “A study of abrasive wear under three-body conditions,” *Wear*, vol. 4, no. 5, pp. 345–355, Sep. 1961, doi: 10.1016/0043-1648(61)90002-3.

[147] A. Surzhenkov, M. Viljus, T. Simson, R. Tarbe, M. Saarna, and F. Casesnoves, “Wear resistance and mechanisms of composite hardfacings at abrasive impact erosion wear,” *J. Phys.: Conf. Ser.*, vol. 843, p. 012060, May 2017, doi: 10.1088/1742-6596/843/1/012060.

[148] M. Moazami-Goudarzi and F. Akhlaghi, “Wear behavior of Al 5252 alloy reinforced with micrometric and nanometric SiC particles,” *Tribology International*, vol. 102, pp. 28–37, Oct. 2016, doi: 10.1016/j.triboint.2016.05.013.

[149] A. P. Sannino and H. J. Rack, “Dry sliding wear of discontinuously reinforced aluminum composites: review and discussion,” *Wear*, vol. 189, no. 1–2, pp. 1–19, Oct. 1995, doi: 10.1016/0043-1648(95)06657-8.

[150] Y.-C. Kang and S. L.-I. Chan, “Tensile properties of nanometric Al2O3 particulate-reinforced aluminum matrix composites,” *Materials Chemistry and Physics*, vol. 85, no. 2–3, pp. 438–443, Jun. 2004, doi: 10.1016/j.matchemphys.2004.02.002.

[151] S. T. Erdoğan, A. M. Forster, P. E. Stutzman, and E. J. Garboczi, “Particle-based characterization of Ottawa sand: Shape, size, mineralogy, and elastic moduli,” *Cement and Concrete Composites*, vol. 83, pp. 36–44, Oct. 2017, doi: 10.1016/j.cemconcomp.2017.07.003.

[152] N. P. Daphalapurkar, F. Wang, B. Fu, H. Lu, and R. Komanduri, “Determination of Mechanical Properties of Sand Grains by Nanoindentation,” *Exp Mech*, vol. 51, no. 5, pp. 719–728, Jun. 2011, doi: 10.1007/s11340-010-9373-z.

Appendix A – As-Deposited Coating Characterization

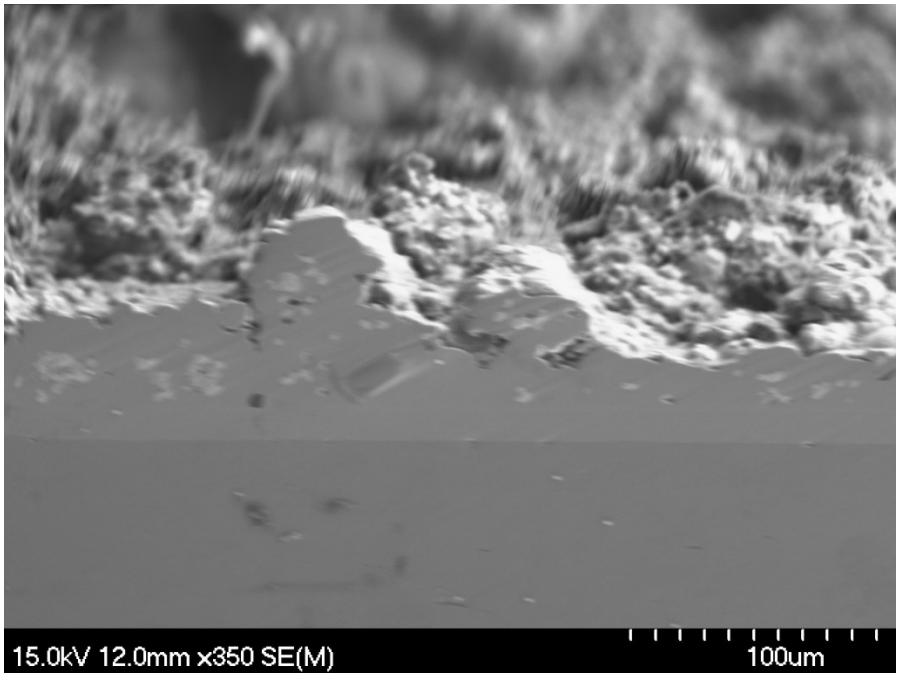

Figure A – 1: Additional SEM image of the as-deposited Ni-P-Tribaloy cross-section.

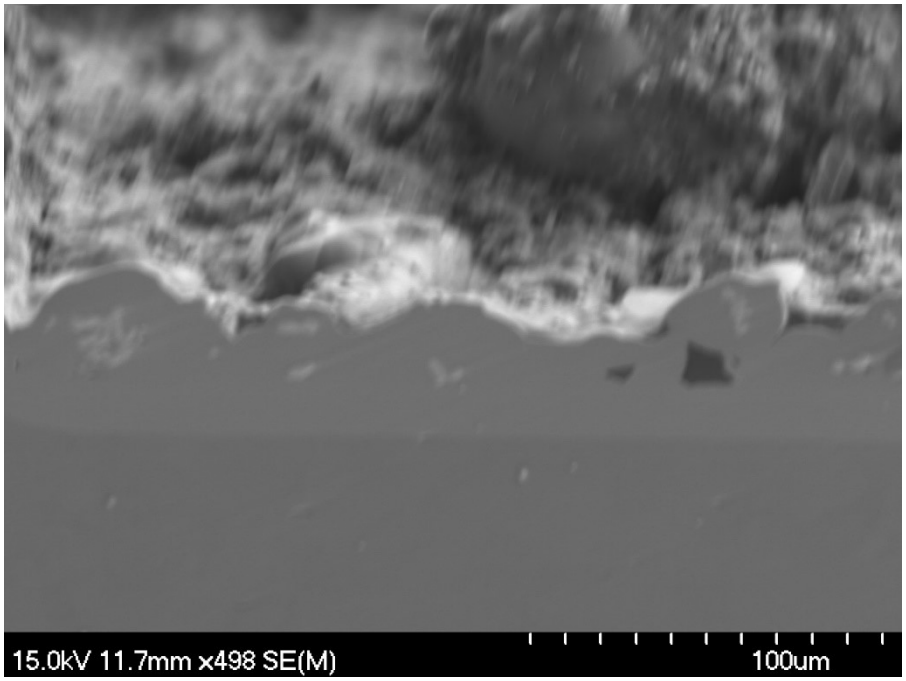

Figure A – 2: Additional SEM image of the as-deposited Ni-P-Tribaloy cross-section.

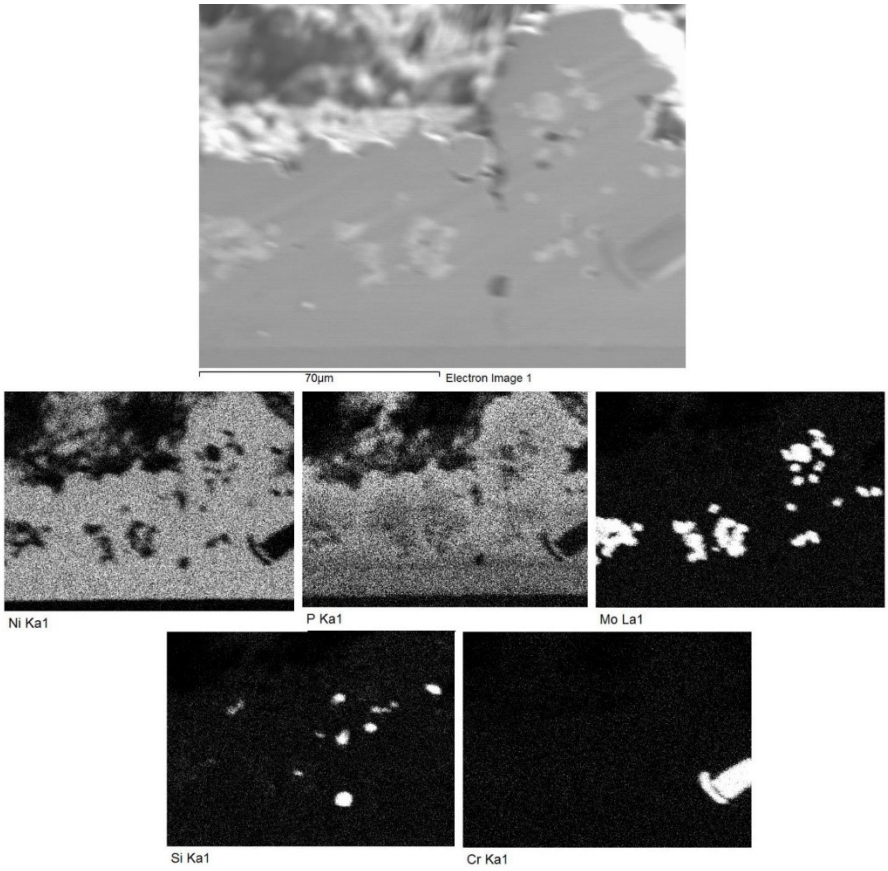

Figure A – 3: EDS mapping of as-deposited Ni-P-Tribaloy coating cross-section.

Appendix B – Micro-Hardness Load–Depth Curves

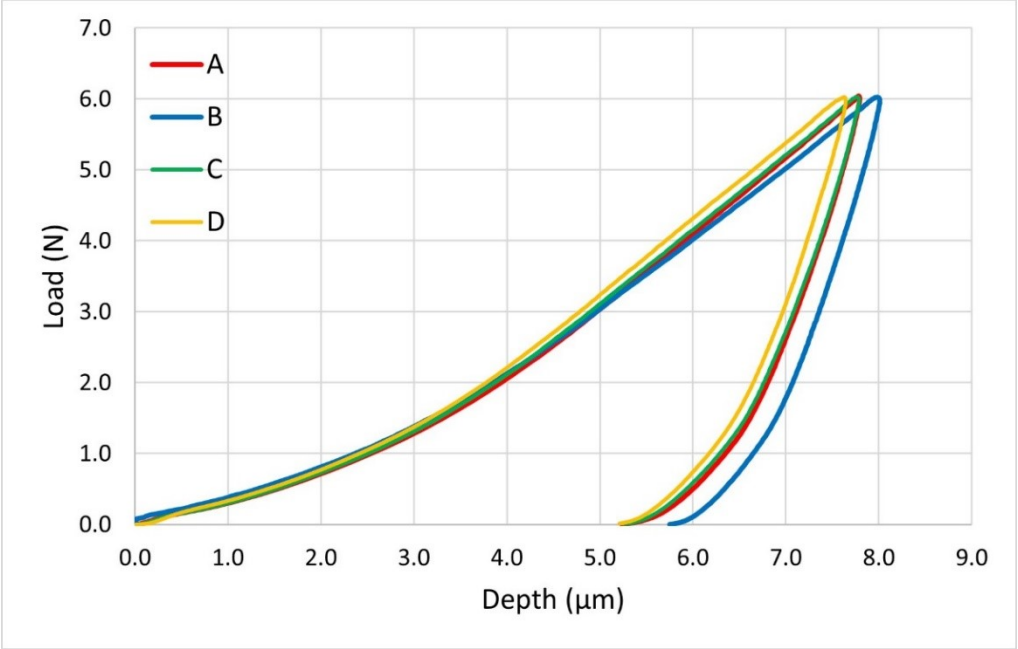

Figure B – 1: All load–depth curves for Ni-P.

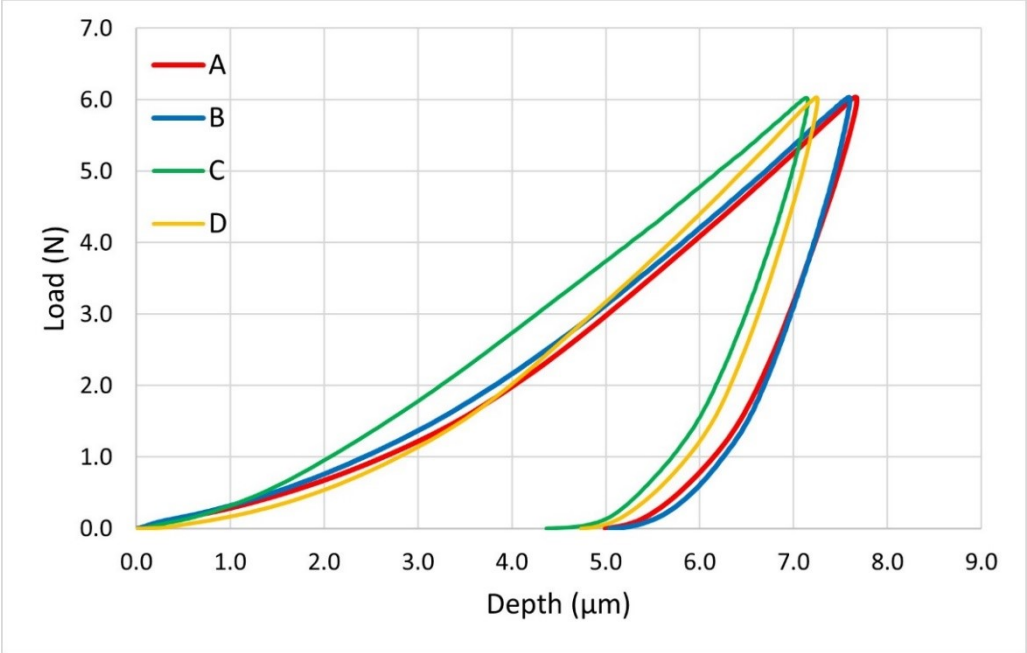

Figure B – 2: All load–depth curves for Ni-P-Tribaloy.

Appendix C – Indentation Images

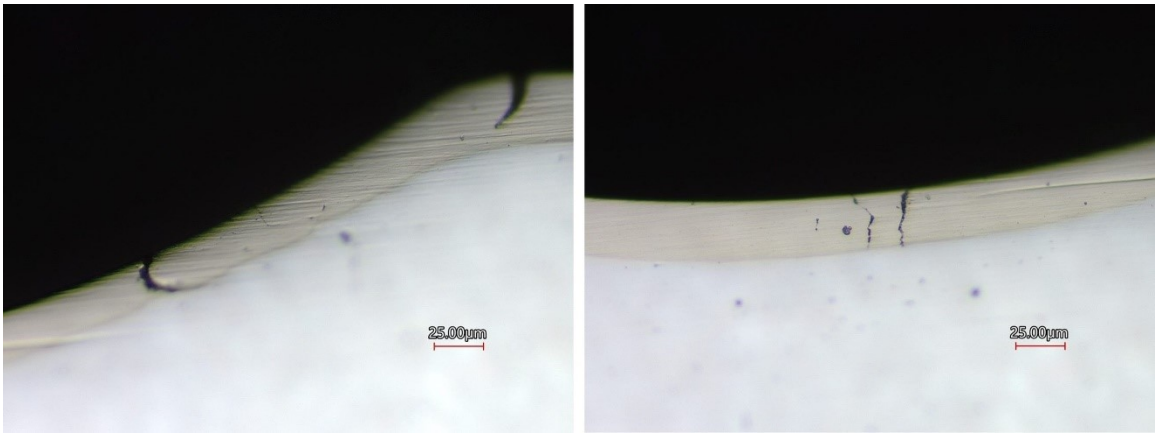

Figure C – 1: Additional images of indent cross-section around Ni-P.

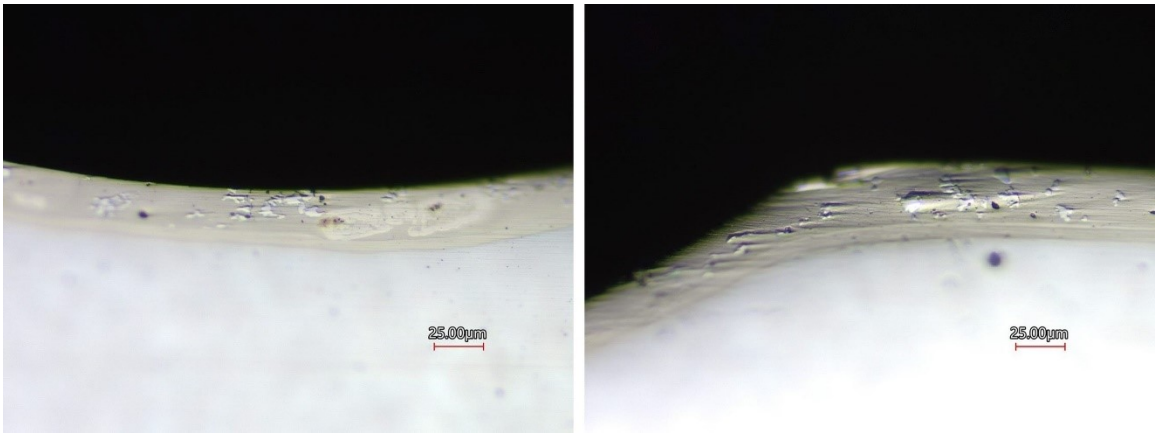

Figure C – 2: Additional images of indent cross-section around Ni-P-Tribaloy.

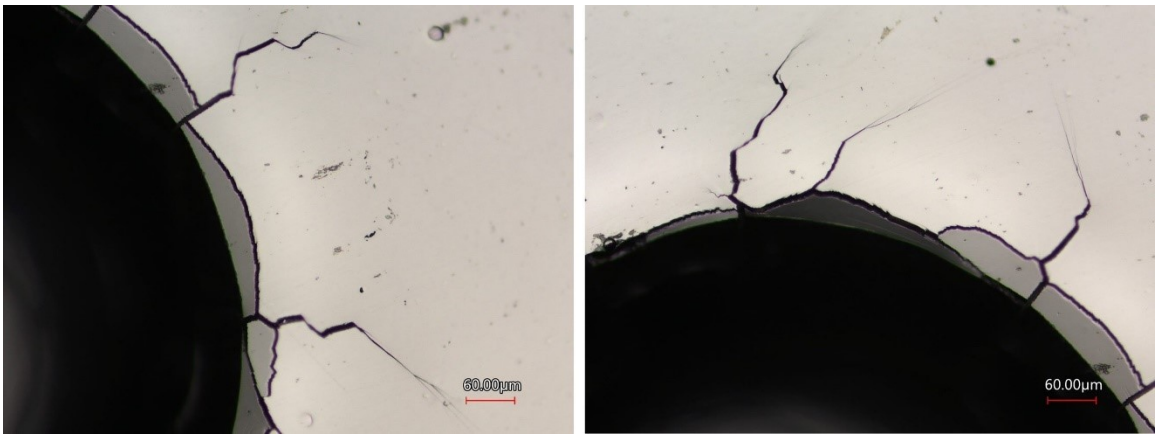

Figure C – 3: Additional close-up images of indent around Ni-P.

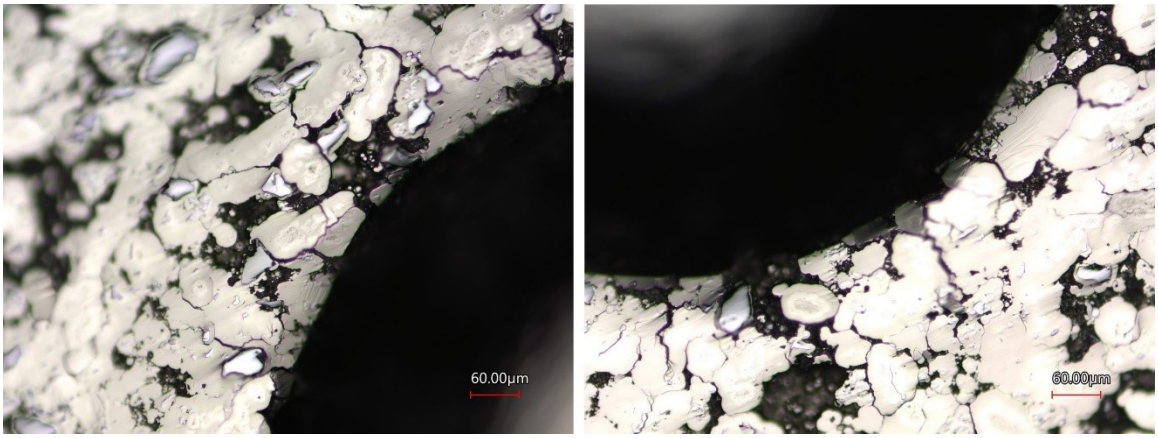

Figure C – 4: Additional close-up images of indent around Ni-P-Tribaloy.

Appendix D – Scratch Full Length Tracks

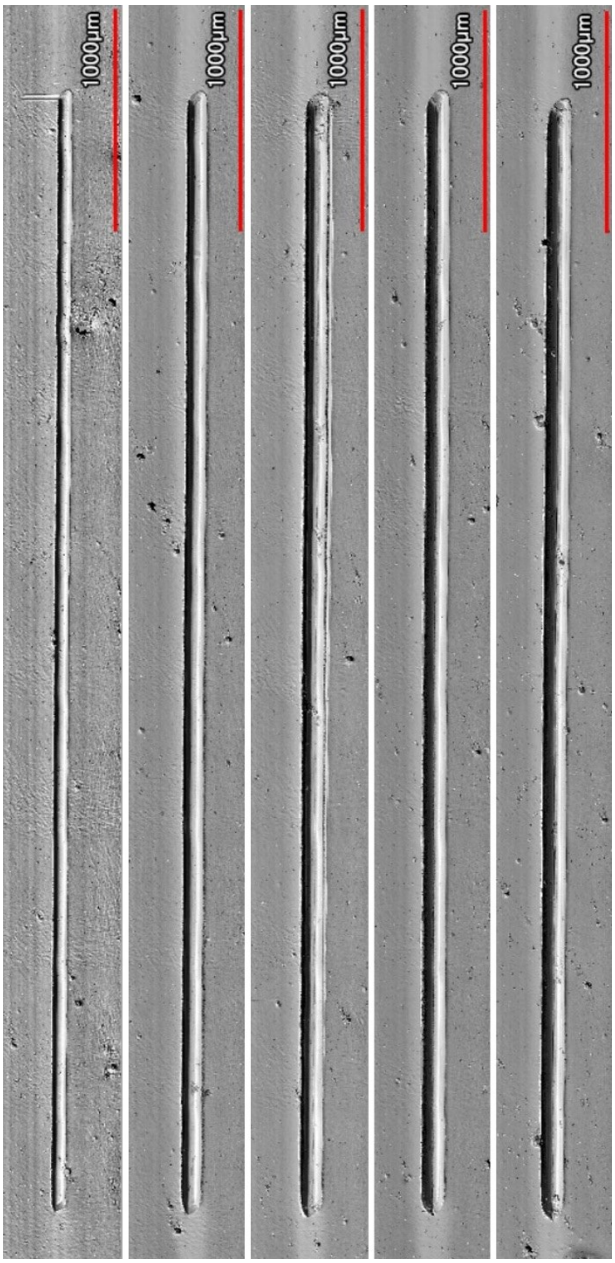

Figure D – 1: Confocal microscopy image of all scratches for Ni-P.

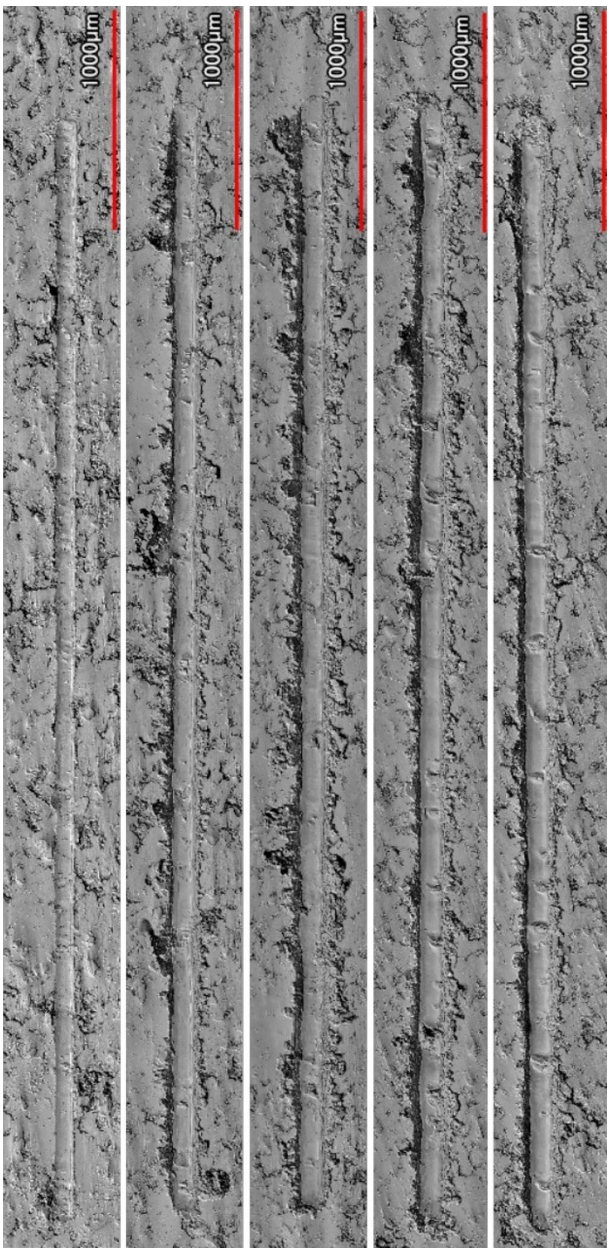

Figure D – 2: Confocal microscopy image of all scratches for Ni-P-Tribaloy.

Appendix E – Abrasion Scars

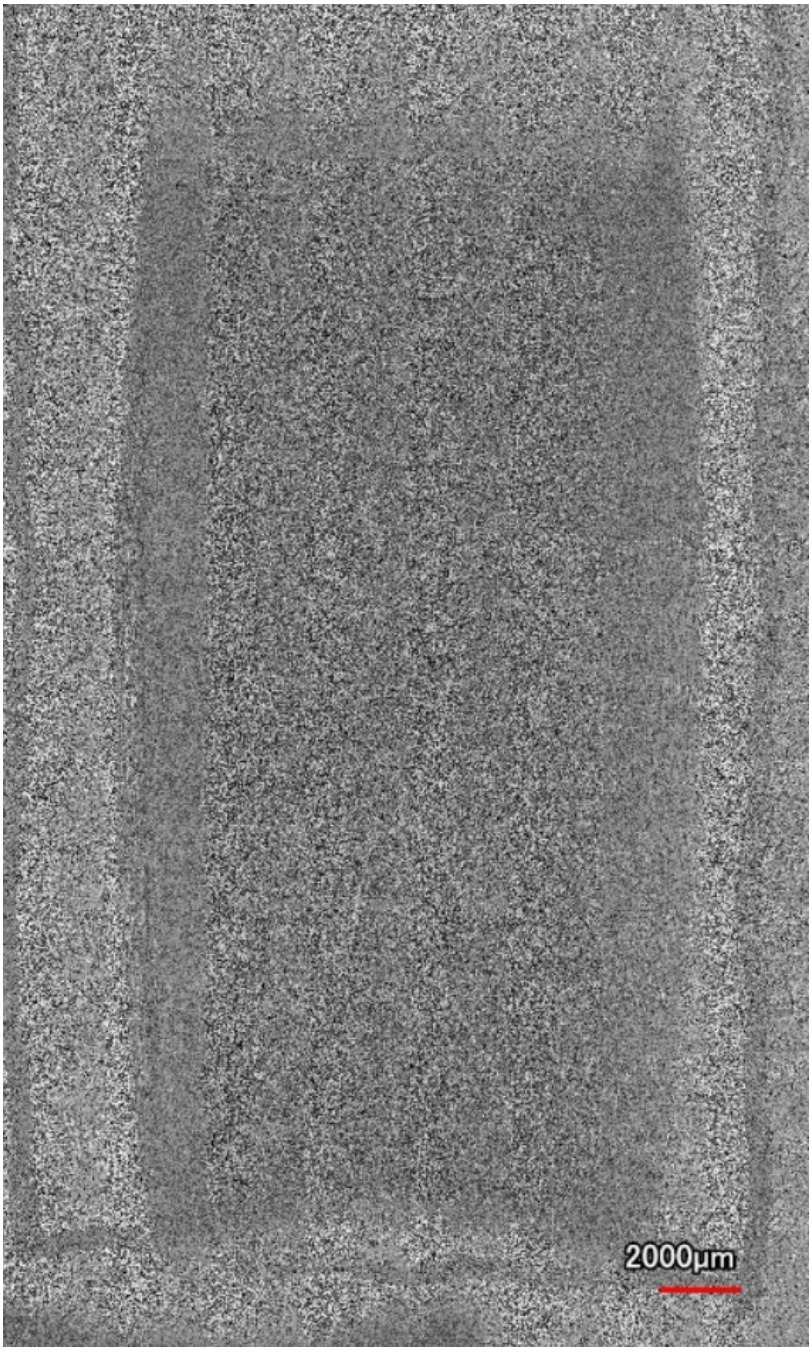

Figure E – 1: Confocal microscopy image of abrasion wear scar on Ni-P.

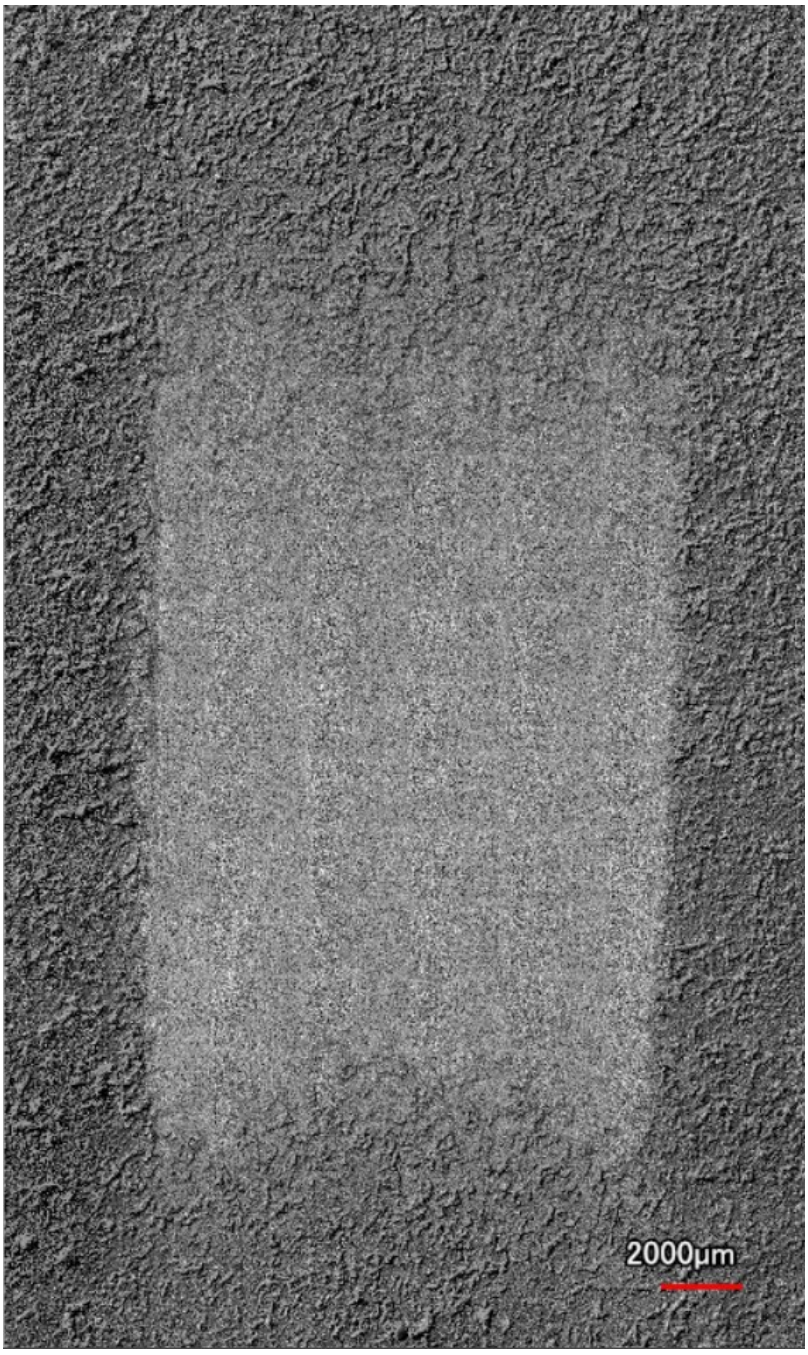

Figure E – 2: Confocal microscopy image of abrasion wear scar on Ni-P-Tribaloy.